

University of Nebraska - Lincoln

DigitalCommons@University of Nebraska - Lincoln

Mechanical (and Materials) Engineering --
Dissertations, Theses, and Student Research

Mechanical & Materials Engineering,
Department of

Summer 8-16-2013

THE MECHANICS OF INTRACRANIAL LOADING DURING BLAST AND BLUNT IMPACTS – EXPERIMENTAL AND NUMERICAL STUDIES

Veera Selvan Kuppuswamy

University of Nebraska-Lincoln, veera_1431@yahoo.co.in

Follow this and additional works at: <https://digitalcommons.unl.edu/mechengdiss>



Part of the [Applied Mechanics Commons](#)

Kuppuswamy, Veera Selvan, "THE MECHANICS OF INTRACRANIAL LOADING DURING BLAST AND BLUNT IMPACTS – EXPERIMENTAL AND NUMERICAL STUDIES" (2013). *Mechanical (and Materials) Engineering -- Dissertations, Theses, and Student Research*. 51.
<https://digitalcommons.unl.edu/mechengdiss/51>

This Article is brought to you for free and open access by the Mechanical & Materials Engineering, Department of at DigitalCommons@University of Nebraska - Lincoln. It has been accepted for inclusion in Mechanical (and Materials) Engineering -- Dissertations, Theses, and Student Research by an authorized administrator of DigitalCommons@University of Nebraska - Lincoln.

**THE MECHANICS OF INTRACRANIAL LOADING DURING
BLAST AND BLUNT IMPACTS – EXPERIMENTAL AND
NUMERICAL STUDIES**

By

Veera Selvan Kuppuswamy

A THESIS

Presented to the Faculty of
The Graduate College at the University of Nebraska
In Partial Fulfillment of Requirements
For the Degree of Master of Science

Major: Mechanical Engineering and Applied Mechanics

Under the Supervision of Professor Namas Chandra

Lincoln, Nebraska

August, 2013

THE MECHANICS OF INTRACRANIAL LOADING DURING BLAST AND BLUNT IMPACTS – EXPERIMENTAL AND NUMERICAL STUDIES

Veera Selvan Kuppuswamy, M.S.

University of Nebraska, 2013

Advisor: Namas Chandra

Head injuries in an explosion occur as a result of a sudden pressure changes (e.g. shock-blast) in the atmosphere (primary injury), high velocity impacts of debris (secondary injury) and people being thrown against the solid objects (tertiary injury) in the field. In this thesis, experimental and numerical approaches are used to delineate the intracranial loading mechanics of both primary (blast) and tertiary injuries (blunt).

The blast induced head injuries are simulated using a fluid-filled cylinder. This simplified model represents the head-brain complex and the model is subjected to a blast with the Friedlander waveform type of loading. We measured the temporal variations in surface pressure and strain in the cylinder and corresponding fluid pressure. Based on these data, the loading pathways from the external blast to the pressure field in the fluid are identified. The results indicate that the net loading at a given point in the fluid comprises direct transmissive loads and deflection-induced indirect loads. The study also shows that the fluid pressure (analogue of intracranial pressure) increases linearly with increase in reflected blast overpressures (ROP) for a given shell thickness. When the ROP is kept constant, fluid pressure increases linearly with the decrease in shell thickness.

For understanding the blunt induced head injuries, the compliant (acrylic gel complex) and rigid (aluminum body) head surrogates with an identical mass are impacted on target surfaces of different stiffnesses. The study indicates that the acceleration field in the gel-filled head surrogate varies from coup to counter-coup region, whereas the field is uniform in the rigid surrogate. The variation in the acceleration field is influenced by the shell deformation that in turn depends on the stiffness of the target surface. Impact studies on the helmet padding currently being used by the US Army are also carried out at different loading conditions. Our results indicate that for a fixed thickness of a foam pad, an increase in the stiffness of the pad will result in the increased absorption of the impact energy.

DEDICATION

This thesis is dedicated to the people involved in resolving the traumatic brain injury

ACKNOWLEDGMENTS

I would like to thank Professor Namas Chandra for his immense efforts and guidance on my research and thesis. His attitude and approach to research is truly inspiring, which made me to focus better on the research. The quality of the research would not have been better without his involvement and comments. His words of wisdom always motivated me and I am greatly indebted to him for this continued help and encouragement on the research and on my personal life as well.

I would like to thank Professor Ruqiang Feng for helping me to understand the blast structure interactions. The blast part of the study would not have progressed without his involvement and comments. I really appreciate his timely response, guidance and encouragement on the studies. I would like to thank Professor Joseph A. Turner for his continued support and encouragement on different aspects of my study.

I am greatly thankful to Dr. Chandra, Dr. Feng and Dr. Turner for serving on my thesis committee. I would like to thank Dr. Shailesh Ganpule for his assistance on the simulations and draft preparation and his hard work inspired me a lot. I thank Nick Kleinschmit for conducting the blast experiments and I appreciate Aaron Alai, Kurtis Palu, Brandon Perry, Steve Gloor and members of the machine shop for assisting me with the blunt experimental part of the study. I thank Dr. Maciej Skotak for his effort and support on the thesis and Dr. Fang Wang for her moral support. Special thanks to Aravind Sundaramurty who helped me now and then during the entire course of my study.

Finally yet importantly, I would like to thank the Army Research Office for funding the research and supporting my graduate study as well.

TABLE OF CONTENTS

DEDICATION	iv
ACKNOWLEDGMENTS	v
TABLE OF CONTENTS.....	vi
LIST OF FIGURES	xi
LIST OF TABLES	xvi
CHAPTER 1: INTRODUCTION.....	1
1.1 RESEARCH OBJECTIVES	5
1.2 RESEARCH SCOPE	6
1.3 ORGANIZATION OF THESIS.....	7
CHAPTER 2: LITERATURE REVIEW	9
2.1 INVITRO MODELS.....	10
2.2 ANIMAL MODELS.....	13
2.2.1 Blast case	13
2.2.2 Blunt case.....	15
2.3 CADAVER MODELS	17
2.3.1 Blast case	18
2.3.2 Blunt case.....	19
2.3.3 FE study	20
2.4 MECHANICAL HEAD MODELS	21
2.4.1 Blast case	23
2.4.2 Blunt case.....	24

2.5 SUMMARY	25
 CHAPTER 3: BLAST WAVE LOADING PATHWAYS IN THE SKULL BRAIN	
COMPLEX	27
3.1 INTRODUCTION	27
3.2 METHODS	28
3.2.1 Theoretical Considerations	28
3.2.2 Experiments	33
3.2.3 Computational Model	37
3.2.3.1 FE discretization	37
3.2.3.2 Material Models	39
3.2.3.3 Loading and boundary condition	40
3.2.3.4 Solution scheme	41
3.3 RESULTS	43
3.3.1 Experimental Results	43
3.3.2 Numerical Model Validation	46
3.3.3 Parametric studies on cylindrical head model	50
3.4. DISCUSSIONS	51
3.4.1 Arrival time analysis	52
3.4.2 Pressure Magnitude.....	53
3.4.2.1 Blast Load	53
3.4.2.2 Impedance mismatch	55
3.4.2.3 Shell Thickness	56
3.4.3 Correlation between fluid pressure and shell strain	57

3.4.4 Coup-Countercoup effect.....	58
3.4.5 Effect of cylinder radius.....	59
3.5 CONCLUSIONS.....	62
NOMENCLATURE.....	63
CHAPTER 4: RELATIONSHIP BETWEEN BLASTWAVE INTENSITY, SKULL THICKNESS AND INTRACRANIAL PRESSURE	65
4.1 INTRODUCTION.....	65
4.2 EXPERIMENT AND NUMERICAL MODEL	67
4.3 RESULTS AND DISCUSSION.....	69
4.3.1 Reflected overpressure (ROP)	69
4.3.2 Intracranial Pressure (ICP).....	72
4.3.3 Shell strain (ϵ_s)	74
4.4 RELATIONSHIP METHODOLOGY	76
4.4.1 Relationship	77
4.4.2 ICP equation.....	78
4.4.3 Valid range of ICP equation	79
4.4.4 Limitation of ICP equation	80
4.5 ROLE OF SKULL DEFLECTION ON ICP	80
4.6 CONCLUSIONS	84
CHAPTER 5: THE BEHAVIOR OF HOMOGENEOUS VS. FLUID FILLED SOLID HEADFORMS UNDER BLUNT IMPACT LOADING CONDITIONS	86
5.1 INTRODUCTION.....	86
5.2 METHODS.....	88

5.2.1 Experiment.....	88
5.2.2 Numerical model.....	91
5.3 RESULTS AND DISCUSSION.....	93
5.3.1 Target surface.....	93
5.3.2 Numerical model validation.....	96
5.3.3 Gel acceleration	97
5.3.4 Limitations of the current study.....	100
5.4 CONCLUSIONS	101
CHAPTER 6: DESIGN OF FOAM PADS FOR MITIGATING THE IMPACT	
INDUCED HEAD INJURY	103
6.1 INTRODUCTION.....	103
6.2 METHODS.....	104
6.2.1 Theoretical model	104
6.2.2 Experimental model.....	108
6.3 RESULTS	110
6.3.1 Low impact velocity	110
6.3.2 Medium impact velocity	112
6.3.3 High impact velocity.....	113
6.4 DISCUSSION	114
6.4.1 Hard and soft foam.....	115
6.4.2 Series and parallel foam.....	116
6.5 CONCLUSIONS	118
CHAPTER 7: CONCLUDING REMARKS	119

7.1 SUMMARY AND CONCLUSIONS.....	119
7.2 RECOMMENDED FUTURE STUDIES.....	121
REFERENCES.....	123

LIST OF FIGURES

Figure 1.1 Primary blast wave (Friedlander wave form)	3
Figure 2.1 a) Schematic representation of the stretch injury device. b) The workflow chart of the in vitro TBI model. (Skotak 2012).....	12
Figure 2.2: a) Strain gauge on rat skull. b) Instrumented rat in the shock tube. (Bolander 2011)	14
Figure 2.3: (a) Frontal blunt impact. (b) Occipital blunt impact. (Ono 1980).....	15
Figure 2.4: Cadaver prepared for occipital blunt impact setup .(Hardy 2007)	20
Figure 2.5 : Development of FE head model from MRI scans of the actual human head. (Ganpule 2011)	21
Figure 2.6: a) Spherical head surrogate b) The surrogate in shock tube. (Varas 2011)...	24
Figure 3.1 Blast wave interaction with heterogeneous body: (a) and (e) are the schematic diagrams of the loading; (b) and (f) are direct loadings; (c), (d), (e), (h) are indirect loadings.	29
Figure 3.2 (a) A 229 mm X 229 mm steel square-12 m long shock tube used in the experiments; (b) Fluid-filled cylinder inside the test section; (c) Cylindrical system with top and bottom sliders; (d) Cylinder (without fluid for clarity) showing the surface mount pressure	35
Figure 3.3 (a) Schematics of the experimental cylindrical set-up; (b) Sectional view A-A showing all the sensor locations (c) Sensor type/location terminology: First letter-F=front, M=middle, B=back; Second number-1=outside, 2=inside; Third letter-P=air surface pressure.....	36

Figure 3.4 (a) FE discretization; (b) Loading and boundary conditions employed in the simulation.....	38
Figure 3.5 Experimental measurements at various locations (a) schematic view of measurement locations; (b) external blast overpressures; (c) cylindrical shell strain; (d) pressure pulse in the fluid.....	45
Figure 3.6 Comparison of experimental and numerical blast pressures at three locations: (a) schematic; (b) front; (c) middle; (d) back.....	47
Figure 3.7 Comparison of experimental and numerical shell strains at three locations: (a) shape change of the cylinder from circle to ellipse obtained from simulation (b) front; (c) middle; and (d) back.	48
Figure 3.8 Comparison of experimental and numerical simulation results at three locations inside the fluid: (a) schematics; (b) front; (c) middle - pressure oscillations corresponding to the round trip wave motion; and (d) back.	49
Figure 3.9 Numerical simulations of pressure pulse: Top row- 2mm polycarbonate/steel; Bottom row-7mm polycarbonate/steel; Pressure rise in fig (b) corresponds to deflection-dominated indirect loads, absent in other cases.....	51
Figure 3.10 Numerical simulation of external flow field at different time points: (a) to (c) show the reflected wave fronts moving upstream; (d) to (f) show the evolution of low pressure region.	54
Figure 3.11 Comparison of external deformation of the cylinder (strain at M1) and fluid pressure in M2 in 2 mm polycarbonate-oil system: (a) Schematic; (b) Concurrent pressure rise in fluid and strain indicating indirect load.	57

Figure 3.12 Wave propagation in 2mm shell and fluid at different time points: (a) polycarbonate (b) steel-with the external shock front shown in dotted line.	59
Figure 3.13 Comparison of fluid pressures and external deformation of the cylinder (strain at M1) (a) 25 mm radius cylinder (b) 75 mm radius cylinder.	61
Figure 4.1 (a) Shock tube used in the experiments; (b) Fluid-filled cylinder inside the test section; (c) Cylinder with top and bottom sliders; (d) 2 mm and 3.5 mm cylinders used in the experiment	68
Figure 4.2 (a) Experimental cylinder set up without fluid showing the surface mount pressure/strain gages on the cylinder and pressure probe flushed with steel tube tip (b) Schematics of the experimental cylindrical set-up (c) Sectional view A-A showing all the sensor locations.....	68
Figure 4.3 Experimentally measured reflected overpressure at three locations: (a) Schematic (b) front (c) middle (d) back.....	70
Figure 4.4 Comparison of experimental and numerical simulations of reflected overpressure at three locations: (a) Schematic (b) front (c) middle (d) back.	71
Figure 4.5 Comparison of experimental and numerical simulation of ICP: Top row-2 mm polycarbonate cylinder; Bottom row-3.5 mm polycarbonate cylinder.	73
Figure 4.6 Comparison of experimental and numerical simulation of shell strain: Top row-2 mm polycarbonate cylinder; Bottom row-3.5 mm polycarbonate cylinder. ..	75
Figure 4.7 (a) Relation between skull thickness and ICP (b) Relation between reflected overpressure and its slopes.....	78
Figure 4.8 (a) Schematic (b) ICP comparison between 2mm and 7mm skull thicknesses (c) ICP correlation with skull strain for 2mm thick shell.	81

Figure 4.9 (a) Relation between skull thickness and skull strain (b) Relation between reflected overpressure and its decay constants	82
Figure 5.1 Top row – compliant surrogate experimental set up; Bottom row – rigid surrogate experimental setup: (a) In built drop tower setup ; (b) Strain gauge on inner bottom surface of the acrylic sphere; (c) Acrylic gel complex rigged with sensors; (d) Schematic of acrylic gel model; (e) Cadex monorail drop tower setup; (f) rigid aluminum surrogate setup; (g) Mounting of accelerometer and load cell; (h) schematic of rigid surrogate.....	90
Figure 5.2 Target surface model.	91
Figure 5.3 Target surface model – 1 m/s impact velocity (a) Compliant surrogate (b) Rigid surrogate.....	95
Figure 5.4 Comparison of experimental and numerical results of compliant surrogate impacting the wooden target surface	97
Figure 5.5 Target surface model – 1 m/s impact velocity (a) Measurement locations (b) Compliant surrogate (c) Rigid surrogate.....	98
Figure 5.6 Gel acceleration near the impact location (B) at 1 m/s impact velocity (a) Wooden surface (b) Hard foam surface (c) Soft foam surface	99
Figure 6.1 (a) Force deflection curve of a typical foam pad; (b) force deflection curve of hard and soft foam; (c) schematic of the head helmet model for foam selection ...	105
Figure 6.2 Schematic of the spring model (a) Individual; (b) Series; (c) Parallel	106
Figure 6.3 Foam pad configurations; top row – actual foam used in experiment: bottom row – schematic model of foam (a) Individual model (b) Series model (b) parallel model.....	107

Figure 6.4 Schematic of the experimental loading setup; a) Individual foam model; b) Series foam model; c) Parallel foam model	108
Figure 6.5 (a) Cadex monorail drop tower setup; (b) rigid aluminum surrogate setup; (c) Accelerometer mounted at the center of ball arm and load cell unit assembled to the bottom of anvil.....	109
Figure 6.6 Experimental measurements at an impact velocity of 1 m/s for all the foam configurations; a) acceleration; (b) impact force	111
Figure 6.7 Experimental measurements at an impact velocity of 3 m/s for all the foam configurations; a) acceleration; (b) impact force	113
Figure 6.8 Experimental measurements at an impact velocity of 5 m/s for all the foam configurations; a) acceleration; (b) impact force	114

LIST OF TABLES

Table 3.1 Finite element discretization	39
Table 3.2 Material properties	40
Table 3.3 Experimentally measured arrival times for 2mm polycarbonate cylinder	44
Table 4.1 bTBI study conducted on different test subjects	66
Table 4.2 Pressure generated in the fluid for the given blast wave overpressure and shell thickness	77
Table 4.3 Characteristics of the ICP equation	79
Table 5.1 Target surface model at 1 m/s impact velocity	94
Table 5.2 Load cell measurements in target surface model	94
Table 6.1 Peak values of the study parameters	112

CHAPTER 1: INTRODUCTION

Lately Improvised Explosive Devices (IEDs) have become a common weapon among the insurgents. Head injuries due to these IED explosions occur as a result of a sudden pressure changes in the atmosphere (primary injury), impacts of debris traveling at high velocity (secondary injury) and people being thrown against the solid objects (tertiary injury) in the field [1, 2]. The IEDs are primarily responsible for most of the casualties occurring in the war zone of recent military conflicts. For instance, in Operation Enduring Freedom in Afghanistan (OEF) and Operation Iraqi Freedom (OIF), injuries caused by explosive blast exposure account for over 60% of overall combat casualties [3].

Among various injuries on the battlefield, traumatic brain injury (TBI) has become a common injury among the soldiers. A recent RAND (Research AND Development) report estimates that 320,000 service members or 20% of the deployed force (of total deployed 1.6 million) are potentially suffering from TBI. In addition, researchers found that about 19 % of returning service members report that they might have had TBI during deployment, with 7 % reporting both a brain injury and major depression [4]. The Center for Disease Control and Prevention estimates that approximately 1.4 million US individuals sustain TBIs per year [5].

The TBI has a wide range of symptoms. Some effects are obvious immediately after the injury, whereas some may appear days, weeks or even years later. Loss of consciousness, nausea, dizziness, mental depression, blurred vision, and headache are some of the acute TBI symptoms. The costs of treating TBI victims of Iraq and

Afghanistan are huge. The RAND study estimated that through 2007, the cost of deployment-related TBI were between \$554 million and \$854 million. Final costs are unknown given the uncertainty over the length of the conflict as well as uncertainty over the natural history of TBI [6]. Hence, it is critical to understand the mechanics of TBI to formulate the mitigation strategies and to reduce the cost involved in treating it.

The TBI primarily results from the interaction of blast wave and human head (primary injury) and head-object impacts (tertiary injury). In case of the blast wave induced TBI, direct transmission of the blast wave, flexure of the skull due to blast load and vascular transmission of pressure wave from the thorax to the brain are identified as a few potential mechanisms [7-10]. For the blunt impact induced injuries numerous studies have been carried out and linear and rotational acceleration of the head and the relative motion between skull and brain are identified as the key mechanics of injury [11-14].

Blast induced TBI (bTBI) is caused by the primary planar blast wave. The blast waveform in the field is quite complex due to interactions with ground and obstacles. However, for studying the bTBI a Friedlander waveform, the simplest form of a shock wave is often employed [15-18]. A schematic of the Friedlander waveform is shown in Fig 1.1. The three main parameters of the Friedlander blast wave are peak overpressure, positive duration and the impulse. The peak overpressure reduces and positive duration of the blast wave increases as the blast wave propagates away from the explosion epicenter. Though negative phase can possibly cause cavitation, it is not considered in this work.

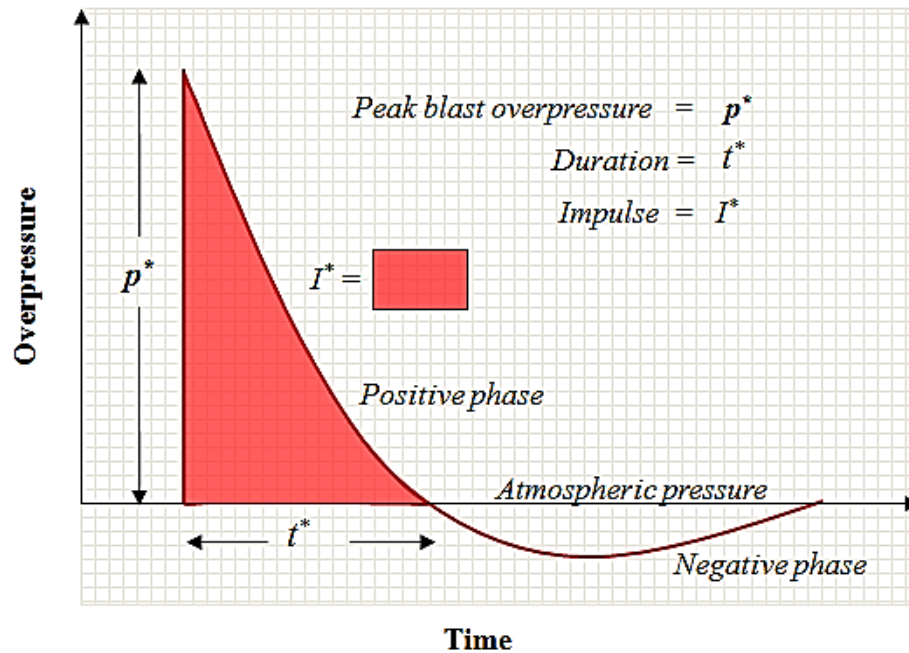


Figure 1.1 Primary blast wave (Friedlander wave form)

Shock tubes are usually employed to generate the Friedlander waveform shock waves in the laboratory. A shock tube generally has a driver, transition and driven sections. The driver section contains pressurized gas (e.g. helium, nitrogen), which is separated from the transition by Mylar membranes, while the remaining sections contain air at atmospheric pressure and temperature. Upon membrane rupture, the shock wave is generated which expands through the transition and develops into the planar Friedlander waveform shock wave in the driven section. Thus, the test subject like animal model or cadaver head placed in the shock tube is subjected to the primary blast wave, which facilitates the study of the mechanics of TBI. In spite of many studies have been carried out for bTBI and a few mechanisms are identified, the true mechanics of the injury is yet to be discovered.

In case of blunt impact TBI, numerous studies have been carried out in understanding the underlying mechanisms. Studies were carried out on the whole body cadavers, cadaver heads, surrogate headforms and dummies at different loading conditions. A few specific parameters like linear and rotational acceleration, relative motion between brain and skull and coup and counter coup effect have been identified as key factors in determining the severity of blunt injury. For many years, the linear acceleration at the center of gravity of the head has been used to assess the injury probability in the blunt impact models.

The test procedure for the head protection system (helmet) is performed in accordance with the Federal Motor Vehicles Safety Standard (FMVSS) 218 [19]. In this testing procedure, the helmeted headform rigged with a single-axis accelerometer is dropped on a hemispherical or flat anvil. The peak headform acceleration limit of 400 G is set as the pass-fail criterion for helmets. The 400 G threshold is considered as the limit for serious brain injury. Army combat helmets do not have a well-defined basis of the testing criteria. The acceleration criterion in motor vehicle standard is a rational choice to prevent serious head injury, based on knowledge base developed in the motor vehicle industry for many years. This criterion could not be directly used in military environments because of the inherent differences between these two, most importantly the unavailability of immediate medical assistance in the war zone. Further in automobiles, passengers do not wear helmets, whereas soldiers do in the field. Hence, the peak acceleration limit was reduced to 300 G. The advanced combat helmet (ACH) meets this testing criterion at 10.1 feet per second (fps) impact velocity. However due to the demands of the modern battlefield the US Army has raised the impact velocity to

14.14 fps and 17.3 fps [20, 21]. Interestingly, currently used helmets do not meet these updated testing criteria.

The in-depth understanding of the loading mechanics of a blunt impact is required to establish the testing criteria and for the development of safer helmets. Currently a homogenous rigid headforms are used for assessing the blunt induced injury. However, the human head is heterogenous and deformable. This raises two critical questions: 1) can a homogeneous rigid headform represent the heterogeneous skull-brain complex? 2) If not, which is the critical point of measurement and what needs to be measured in the compliant headform? Hence, a thorough study of the compliant and rigid headform is required to answer the above questions and to establish the appropriate testing criteria of helmets.

1.1 RESEARCH OBJECTIVES

The main objective of this research is to understand the intracranial loading mechanics of blast and blunt impact events. The loading pathway from the external field to the affected point in the intracranial content is the core objective of the study. The polycarbonate cylinder filled with mineral oil, and the acrylic spherical shell filled with ballistic gel are chosen as head surrogate models for this study.

The loading pathways are studied by analyzing each component of the surrogate, from the external load to the internal affected region. For the blast loading case, we performed the analysis of pressure transmission as the shock wave progresses through the surrogate. In the experiment, the pressure sensors measure the progression of the external blast loading; the loading process is studied in detail using complementary

numerical simulations. Similarly, the pressure and strain sensors measure the response of the test subject for the applied external load. The numerical modeling of the blast loading and response of the test subject are carried out to identify the most plausible loading pathways.

For blunt impact induced TBI model, the loading pathways in compliant and rigid head surrogates are compared. To deduce the effect of compliance of the surrogate on the acceleration, the acrylic-gel surrogate is rigged with a uniaxial accelerometer at the center and a strain gauge at the bottom of the shell's interior. Assuming negligible deformation, the rigid surrogate is fitted only with a uniaxial accelerometer. Then, the comparison study between compliant and rigid surrogates are made. The effects of target surface materials on the acceleration are also studied. The resulting relationship provides insight in the understanding of the mechanics of loading. The effect of the target surface like foam pads on the loading of intracranial content will aid in the development of the head protection systems. This objective is critical for the development of safer helmets.

1.2 RESEARCH SCOPE

A complex phenomenon is normally analyzed based on the findings obtained from simple case studies. The mechanics of blast and blunt induced TBI is highly complex to study with the actual human head. Currently, blast induced TBI is studied using different animal models (mice, rats, pigs) and these findings are then scaled to the actual human head. On the other hand, blunt impact is well studied with the whole body cadaver, cadaver heads, headforms and dummies. The existing head injury criteria for blunt impact are typically driven from the skull fracture. A true brain injury criterion is

yet to be established. Hence, the right blunt injury mechanics have to be figured out and the brain injury criteria have to be established with the right impact loading conditions.

To understand the intracranial mechanics in blast or blunt impact models, the mechanics of the loading of the individual component of the head (skull and brain, for instance) have to be clearly studied. With the mechanical head surrogate approach, influence of different components of the head in the mechanics of loading could be studied in detail. Since the mechanical head surrogates could be modified for studying the specific mechanism of the TBI, the primary injury causing mechanism can be easily identified with this surrogate. Based on the findings, experimentation on the animal and human head models can be designed for TBI. The significance of each injury parameter and its characteristics at various loading conditions can be figured out from the experimentation, from which in turn the mitigation strategies can be formulated. Thus, the mechanical head surrogate study forms the baseline model for TBI. From this baseline model, different hypothesis on TBI can be verified that can be extended to the animal and human models.

1.3 ORGANIZATION OF THESIS

The thesis consists of seven chapters. Test subjects previously used for studying TBI are categorized and discussed separately in Chapter 2. Advantages and limitations of each model are listed in the same chapter. Chapter 3 deals with the blast-loading on the head surrogate. Blast loading propagation process across the human head and key parameters involved are discussed in detail. The relationship between blast wave intensity, skull thickness and intracranial pressure is discussed in the Chapter 4. Chapter 5 deals with the characterization of a compliant surrogate; the comparison study between

compliant and rigid surrogate is presented in this chapter. The effects of the target surface and skull deformation on the acceleration of the head are also analyzed. In Chapter 6, energy-absorbing characteristic of the helmet padding for the mitigation of the head injuries are presented. Finally, in Chapter 7, conclusions are made based on the performed studies. Variations of these results with respect to size, shape and material models of the test subjects are also discussed in this chapter. Future recommendations to improve the understanding of TBI are also included.

CHAPTER 2: LITERATURE REVIEW

This chapter deals with the past studies conducted for understanding the intracranial loading mechanics due to blast and blunt impacts. The key findings in those studies along with the limitation of the studies are also presented. Since numerous studies have been carried out for blunt impact loadings and the related head loading mechanisms, the focus is given more on the blast loading mechanics. Various studies on different test subjects have been carried out to unravel the actual mechanics of blast induced TBI. Commonly used test subjects are *in vitro* cell culture, *in vivo* animal models, mechanical head models, cadaver head models, and numerical models. These subjects are selected based on the mode of injury and the severity of TBI studied. For instance, *in vitro* model represents the cellular level injury model followed by an animal model that represents the tissue level injury model. Finite element methods are extensively used in figuring out the details loading process that are not possible in the experiments.

Though the study parameters and study methodology vary with test subjects, the primary goal of all the studies is to establish the mechanics of loading. In animal models, for instance histology, pathology and immunohistochemistry are carried out to identify the mechanics of TBI [22]. In few other animal studies, intracranial pressure, skull flexure and lung pressure are studied to determine the mechanics of TBI [17, 23]. In *in vitro* study subjects, due to the limitations in measuring techniques and testing methodologies, only certain parameters like pressure and strain are monitored in the studies [24, 25].

Generating a proper loading condition is a critical experimental requirement; this is especially true for blast TBI. The loading conditions are chosen based on the size and type of test subjects. For instance, *in vitro* models may not be loaded with the loading conditions used for mechanical head surrogates. Hence, choosing the right combination of loading conditions and test subjects will help in the understanding of the correct response of the test subjects. Each test subject is unique and has different advantages and limitations as discussed below.

2.1 INVITRO MODELS

An *in vitro* neuronal injury model is typically done at the cellular level. For instance, the cell can either be injured due to stretching, compression or torsional loading. The cells employed in the study are cultured in the right medium, supplemented with serum for their growth. These cells are then placed in the test medium and are subjected to appropriate loading conditions. After the loading, the cells are usually stained and tested for the injury. Though the loading mechanics of blast and blunt are supposedly different, the mode of brain injury depends on the spatiotemporal variation of stress field (intracranial pressure, shear stress and shear strain) in the brain, which is common for both blast and blunt. Hence, the *in vitro* models are commonly employed to study the mode of injuries for both blast and blunt studies.

The first *in vitro* stretch model was developed by Ellis et al. to evaluate the injury of astrocytes [26]. Astrocytes cells were grown on silastic membrane and the membrane was stretched using a positive pressure pulse. The severity of cell injury was related to the intensity of deformation of the membrane. Ellis and co-workers came up with an arbitrary injury scale based on strain levels applied to cells: 31% – mild, 38% – moderate

and 51% – severe. This membrane stretch injury model was then widely used in the research of cell cultures composed of cortical, hippocampal and cerebellar neurons and glia [27, 28].

To evaluate the cellular level tolerance to strain, optical nerve of a guinea pig was employed [29]. The optical nerve was stretched to different lengths by a sling. Changes in the visual potential were then measured to check the functional impairment of the optic nerve. Visual evoked potential is the electrical signal transmitted through the optic nerve. Intensity of degradation of this potential indicates the level of neuronal damage on stretching.

To study the effect of rate of loading, a distinct membrane stretch model was developed which is shown in Fig 2.1 [24]. In this model, the stretch rate of the membrane corresponds to the loading rate. This is a modified version of the cultured axonal injury (CAI) device and used strain rate between 15 to 68 s⁻¹. SH-SY5Y cells cultured on the membrane were used in this study. It was found that the effect of strain rate was insignificant for the strain fixed at 50%. Stretch induced dose-response curve was also developed which showed a very sharp increase in numbers of injured cells in a range of strain of 30-55%.

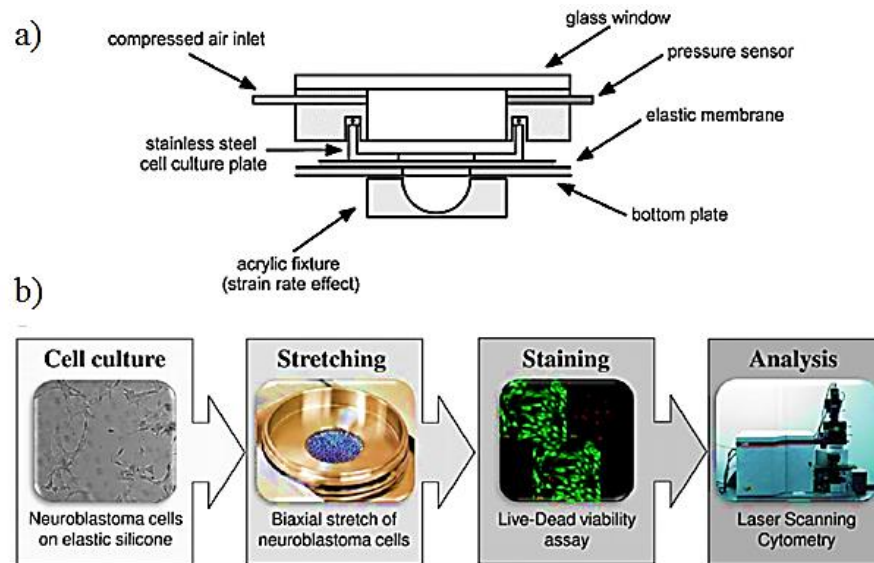


Figure 2.1 a) Schematic representation of the stretch injury device. b) The workflow chart of the in vitro TBI model. (Skotak 2012)

There are many *in vitro* models available to study the effect of TBI, mostly in a stretching regime. Some other models are available for studying the effect of pressures. For example, the model developed by Kodama et al. can be used to study the effects of pressure on cell permeabilization [30]. Human promyelocytic leukemia cells were cultured in a cell culture incubator. The fluorescein isothiocyanate-dextran uptake was used to evaluate the extent of injury, after the cells were subjected to pressure wave in the shock tube. It was concluded that the impulse of the pressure wave rather than the peak pressure changed the permeability of the plasma membrane of the cells.

Results from the *in vitro* cell models (cellular level) give the basic understanding behind the cell injury and its severity. This forms the base for analyzing the animal level models involving pathology studies for TBI. Hence, the cell injury found in the animal models can be compared to the injury established in the *in vitro* model to discover the basic mechanics of injury during the loading. The main disadvantage of *in vitro* model is

its delicacy. An *in vitro* model may not be subjected to actual blast and blunt loading conditions. Similarly, injury parameters like acceleration, pressure, strain and its rate measurements are limited and it has always been questioned whether the applied loads are properly transmitted to the cells.

2.2 ANIMAL MODELS

2.2.1 Blast case

During World War II, most of the deaths in an explosion occurred because of lung injuries. Gas filled organs such as the lungs, larynx and the gastrointestinal tract were more susceptible to blast. Research was focused to establish a lung injury threshold to the blast waves which led to the use of animal models in the injury studies [31, 32]. These studies were carried out by subjecting various animal models to blast waves with different overpressures and positive duration. The lethal dose for 50% of the animals (LD₅₀) was then calculated based on the mortality with respect to blast overpressures and positive durations. Most of the animal models used for the study were mammals. Animal models used in the study comprised of 264 dogs, 115 goats, 200 mice, 110 hamsters, 150 rats, 120 guinea pigs, 48 cats, and 40 rabbits [31].

The blast induced TBI is a extremely challenging problem. There is always a delay between the TBI event and the symptoms arising out of the event. Some behavioral changes are often observed as a consequence of the TBI event. Hence, animal models are widely used to understand the different aspects of the TBI. The animals exposed to the blast wave in a shock tube were then monitored for the symptoms and behavioral changes [33]. In another study, detailed pathology was carried out in the blast exposed animal models to develop the treatment techniques for TBI [22].

There are different hypotheses for the cause of TBI. In one theory, chemical changes in the brain and body following a blast exposure lead to in TBI. This theory was studied in rabbits and rats. A significant increase in free radicals with the decrease in antioxidant levels has been observed in the rabbits and rats following blast exposure [34]. Since free radicals are observed in victims subjected to blast exposure, it is hypothesized that the release of radicals following blast exposure may cause chemical imbalance resulting in apoptosis of the neuronal cells [35].

In another hypothesis, flexing of the skull due to blast load increases the intracranial pressures in the brain [8]. This hypothesis was tested using rat models [23]. Strain gauges are attached at three locations on the rat's skull as shown in Fig 2.2 and are exposed to blast waves. From the measured strain values it was found that skull did flex due to impinged blast load. The oscillations in the intracranial pressure profile dictated the frequency of oscillation of the skull.

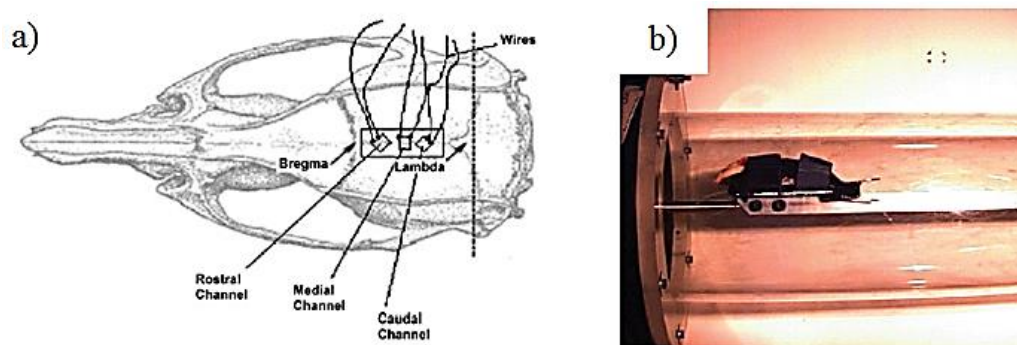


Figure 2.2: a) Strain gauge on rat skull. b) Instrumented rat in the shock tube. (Bolander 2011)

In another hypothesis, the blast wave impinging on the thorax/chest travels through the vascular system to the head that result in TBI [10]. To test the hypothesis, rats were initially taught an active avoidance task for 6 days. Their performance on this

task was studied before they were subjected to the blast waves. The head of the rat was protected from the blast exposure using steel plate during the blast experiment to test the hypothesis. The effects of blast wave impinging on the thorax/chest wall of the rat were studied by assessing the behavior of the rats. The behavior of the rat was reduced for the first 3 hours following the blast exposure. Some chemical changes were also observed in the brain that was supposedly due to the vascular transmission theory.

2.2.2 Blunt case

Primates are frequently used in studies of blunt impact induced TBI. Impact tolerance of human was studied in early 1980 using monkeys [36]. The head was impacted as shown in Fig 2.3 and causes for concussion were established. Translational and rotational acceleration, contact area of the impact and direction of impact were investigated in this study. The threshold for the development of concussion symptoms was also established in this work. These results were then extrapolated to humans using dimensional analysis.

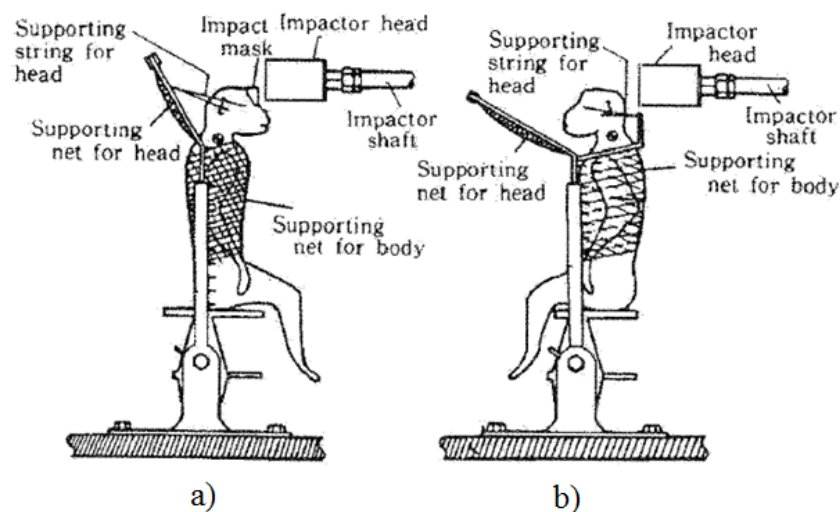


Figure 2.3: (a) Frontal blunt impact. (b) Occipital blunt impact. (Ono 1980)

In another study, axonal injury was studied using a sheep model [37]. The head was impacted on the lateral aspect of the skull. Impact forces, duration of impact and head kinematics were measured. A nine-axis accelerometer array was used to study the head kinematics. The axonal injury was determined using amyloid precursor protein. Axonal injury was consistently observed in all sheep models. Injured regions were identified as sub cortical and deep white matter and periventricular white matter. Severity of injury was then correlated with the peak magnitude of the impact force and linear and angular velocity of the head.

Intracranial pressure (ICP) was analyzed in a study conducted on rabbits [38]. The head was impacted with iron bars and intracranial pressure was monitored with pressure microsensors. Two groups, one with mild and the other with severe injury level were studied. ICPs in severe injury group were high. Coup-countre coup effect was observed in the head. Gross morphological changes observed in this study included different levels of scalp hematoma, skull fractures, subdural hematoma and subarachnoid hemorrhage.

Apart from real animal models, finite element (FE) animal models are also used to study TBI. These finite element models are built from the Magnetic resonance imaging (MRI) sequential images and are meshed and validated against the experiments [16]. Due to the difficulty in building the FE animal models, only a few models are currently available for the study. These FE models complement the experimental study of the animal models. In addition, key features that could not be studied in the actual experiments can be studied with these finite element models. One such study is done in

the blast-loading pathway on rat models. In this, blast wave propagation from the external blast field to the internal brain was captured with the help of the FE rat model [16].

For blunt impact, many two and three dimensional finite element models were developed. Ferret, pig, sheep, rat and monkey FE models were used to understand blunt injury. However, the anatomical structures of the model were not detailed in most of these studies. Different kinds of experiments were carried out and parameters like, pressure, von mises stress and strain were studied in different regions of the brain model.

Hence, actual animal models are primarily used to test the certain hypothesis and other behavioral change studies following the loadings. However, there are many disadvantages and limitations in using animal models. Instrumenting the head of small animal models (rat, mice) is difficult and repeatability of the experiment is questionable. Conversely, though pig has a significantly larger head, the instrumentation is difficult due to the thick skull. Also the skull properties change with the age of the animal models involved in the study [23]. In addition, comparison of results between animal models is difficult because of change in head shape and skull thickness. For instance, pigs have skull thickness of 10 mm whereas rats have a thickness of around 2 mm [39]. These changes may reflect on the hypothesis considered for the study. Hence animal test subjects must be chosen carefully for the study of TBI.

2.3 CADAVER MODELS

Experimentation on cadavers also called post mortem human subjects (PMHS) become popular in the automobile accident field of studies. Since cadaver disintegrates quickly, they are embalmed to protect it and thus the properties of embalmed PMHS may

vary from the actual human. Hence, the experimentation period on the PMHS should be kept as short as possible.

2.3.1 Blast case

For conducting blast induced TBI, the head is usually parted and are exposed to blast in the shock tube. The main problem in conducting the experiment with parted head is retaining the shape of the brain. Parting the head results in the brain collapse and hence it is difficult to conduct the experiment with the brain. One strategy to overcome this problem is to replace the brain with appropriate stimulant material (e.g. ballistic gel). This complete process of removing and replacing the actual brain with the brain simulant followed by instrumentation and then experimentation should be done in a short period due to the tissue decay factor.

Some of the cadaver head experiments were conducted in our research group at the University of Nebraska, Lincoln. Cadaver head was preserved before the experiment and brain was replaced with ballistic gel. The head/brain is instrumented with pressure sensors and strain gauges are attached to the skull. Three strain gauges and four pressure sensors were used in the head; frontal, occipital and lateral portion of the skull were considered for strain measurements; frontal, occipital, midbrain and lateral portion of the brain were considered for pressure measurements. They are then subjected to blast waves generated in 28" shock tube.

In another study conducted by Wayne state university, the brain was used to study bTBI [40]. In those experiments, the head was parted from the body between the third and fourth vertebrae. Carotid arteries and jugular veins were preserved carefully after parting. Then these arteries and veins were fitted with disconnect fittings to assist

perfusion of the head. The intracranial pressure is measured with the optic sensors that were implanted in the brain through the skull and skull flexure were measured using strain gauges fitted on the skull. The instrumented head was then exposed to blast wave.

2.3.2 Blunt case

In the blunt impact TBI both full body PMHSs and heads alone were used to get insight into the mechanics of injury. Many head injury criteria involving acceleration and pressure were determined from these studies [41, 42]. A series of blunt experiments were performed on a unembalmed human cadaver to measure the linear acceleration during blunt impact. Following impact pathological evaluation of the brain tissue was also carried out. It was found that the acceleration in excess of 300 G results in vascular hemorrhage.

In another study, intracranial pressure, strain and relative motion of the brain were studied [43]. Pressure transducers, nine accelerometers and high speed X-ray were employed to study the parameters as shown in Fig 2.4. A pneumatic piston produced blunt impact to the head, and resulting relative motion between skull and brain was quantified. Peak coup and counter coup pressure increased with increase in linear acceleration of the head. Peak strain also increased with increase in linear acceleration. The study also showed that protection offered by helmets, resulted in reduced linear acceleration and thus the injury.

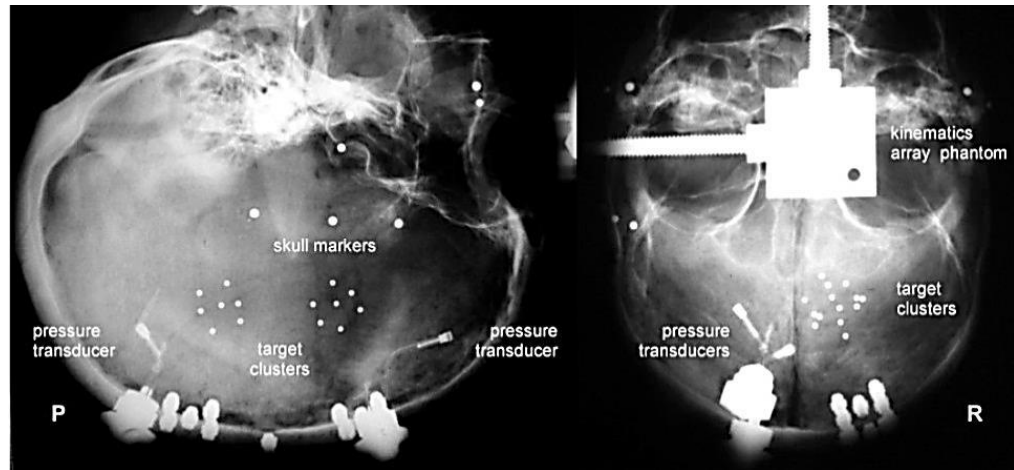


Figure 2.4: Cadaver prepared for occipital blunt impact setup .(Hardy 2007)

2.3.3 FE study

The entire process of the head preparation, preservation of the integrity of the brain tissue using perfusion system and instrumentation of the head with the sensors is a laborious. Variabilities resulting from the sample preparation and experimental factors lead to huge experimental variations. These variations influence the results and hence deciphering each part in the results would be very difficult. Hence, often the finite element head models are used for studying bTBI in humans. There are many finite element head models available for understanding bTBI. As mentioned earlier, finite element model of the human head is generated from the MRI as shown in Fig 2.5 [44]. Though the variabilities in the FE models are smaller, the material property of the each component involved in the model is unknown. However, the FE model will provide a clearer understanding of the fundamentals of bTBI.

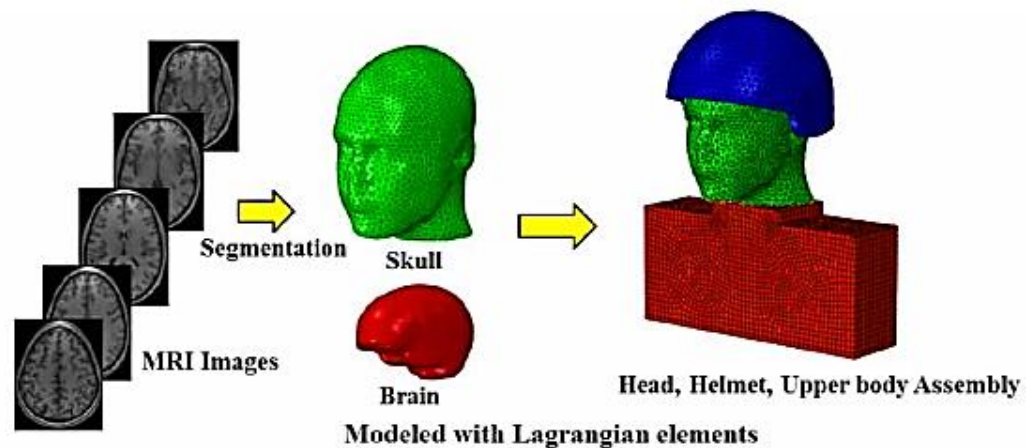


Figure 2.5 : Development of FE head model from MRI scans of the actual human head. (Ganpule 2011)

Many key findings are established using FE head models which are consistent with some of the cadaver head experiments [45]. It was found that the blast wave flow field around the head is not uniform and it varies with change in size and shape of the head. Pressure fields in the brain are related to the intensity of external blast pressure wave and the structural wave of the skull. Intracranial pressure correlates with the surface pressures on the head.

The FE models are also used for to determine the role of personal protective equipment (helmet) on bTBI [44]. FE model, headform and actual cadaver head are the appropriate models to check the role of PPE and improve the design to mitigate bTBI. To check the performance of helmets, test subjects are fitted with helmets and are subjected to blast waves.

2.4 MECHANICAL HEAD MODELS

Test subjects that are robust and consistent in performing TBI studies are mechanical models. Mechanical head models are sometimes called as headforms. The

major limitation of the mechanical model is their lack of biofidelic characteristics. Hence, they are less popular when compared to other test subjects. Mechanical test subjects are simple to build, could be instrumented easily, and could be varied in different sizes and shapes.

Though real test subjects like animal models and cadaver head models supposedly provide true results for TBI, the variations in measured parameters involved in the models are huge. Hence, the actual experimental results are speculative and many numbers of experiments are needed to draw a proper conclusion. Controlling the variables in those models is difficult. Instrumenting *in vitro*, animal and cadaver head subjects is another big issue.

Mechanical head models are available in various forms and sizes. In mechanical models, each parameter in the study like materials involved, positioning of the subject with respect to loading, size and shape of the model, location of sensors and other variables are clearly known. Hence, results drawn from the mechanical models are concrete and thus understanding the basics behind the loading mechanics can be made clearer and stronger.

These mechanical models are not biofidelic. Hence, the response and conclusions made from the mechanical models cannot be directly applied to the humans or animal models. Nevertheless, efforts have been made to enhance the biofidelic nature of the mechanical models. Mechanics of stress wave propagation in the skull and its effect on the brain, pressure propagation in the brain, deformation of the head and other basic phenomena occurring during the loading can be studied thoroughly using mechanical subjects. The conclusions drawn from the mechanical models are useful for animal and

human model studies. Distinct experiments can be designed on the animal and cadaver models based on the conclusions from the mechanical models. Hence, the study on mechanical subjects reduces the variabilities in the animal and cadaver experiments and proper conclusion can be made.

Computational modeling is another plus in using mechanical subjects. Since the material models are commonly available for the mechanical head surrogates, actual loading pathways can be computed accurately. With the help of the combined computational models and the actual experiments, detailed study of the mechanics of TBI can be made. For instance, skull flexure that might be responsible for bTBI was discovered using computational modeling of numerical model [8]. Following this study, the experimental evidence was furnished to confirm the theoretical work of Moss and co-workers [23]. Hence, computational modeling can be useful to identify various mechanisms of the shock wave-head interaction mechanics.

2.4.1 Blast case

With a mechanical subject, the biomechanical response of the head under blast loading was studied [46]. An egg shaped surrogate that mimic the head of small size animal models like those that of a rat was used. The egg shaped surrogate has external skull made of polyethylene filled with silicone gel. The surrogate was subjected to the incident blast wave pressure of around 80 kPa. A single optic pressure sensor was used to measure the pressure inside the gel. Computational modeling was carried out with the arbitrary Lagrangian-Eulerian (ALE)/Lagrangian coupling algorithm available in LS-DYNA.

In another study, spherical gelatin filled skull-brain surrogate was used to study the bTBI [47]. The spherical skull surrogate was made of 7 mm thick polyurethane and filled with ballistic gel (Fig 2.6). The surrogate was fitted with internal pressure sensors and external strain gauges and was subjected to 40kPa incident blast pressure.



Figure 2.6: a) Spherical head surrogate b) The surrogate in shock tube. (Varas 2011)

In this study, the effect of skull opening was evaluated and it was demonstrated that pressure in the gelatin was maximized when the opening was facing the incident blast wave. Computational modeling was also carried out with computational fluid dynamics (CFD). The model was validated with the experiment and then the parametric studies were carried out.

Alley and co-workers performed a series of experiments with mechanical subjects for the characterization of the blast wave interaction [48]. Two types of skull and brain simulants were used. An explosive driven shock tube was used to generate blast waves. The results obtained speculated that pressure amplification occurred at the interface inside the head at the material interfaces. In addition, significant relative displacement was observed between the materials in the head.

2.4.2 Blunt case

Headforms are another type of mechanical test subjects. They are solid body made mostly of magnesium. Headforms are extensively used in the research area focused on various aspects of blunt impact. Different headforms like Hybrid III and NOSCAE are typically used to evaluate the head injury during blunt loading. Performances of helmets are typically tested with these headforms. The helmeted headform is dropped from different height as per the testing standard and acceleration of the headform is measured to assess the pass-fail criteria. In blast loading study, headforms are used to study the external blast loading mechanics on the head and aid the design of PPE for soldiers. In one of the study with the headform, the effect of the passing shock wave on the flow field around the bare and helmeted-headform was studied. Different types of helmets, i.e. suspension and padded helmets were analyzed for their performance under blast loading conditions. Many findings, for example the underwash effects, have been identified in this study. The extent of the underwash effect depends on the size of the void helmet-head space. Computational modeling of these headforms in various configurations helped establish the probable flow fields of the shock wave around the head [44].

2.5 SUMMARY

Though many studies have been carried out to understand the mechanics of TBI, there are no comprehensive and concrete conclusions. Basic mechanisms of TBI still remain unresolved. Hence, a simple comprehensive study is required to clearly identify the basic intracranial mechanics of the TBI. From the above discussion, it has been clear that though many study models are available. The mechanical study model is more robust and simple to deal with. Though the biofidelic nature of the mechanical model is certainly questionable, the response of the model to the specific loading is still

meaningful. Thus, well-planned experiments on mechanical surrogates will produce concrete results when compared to animal and cadaver studies for understanding the basic mechanics of TBI. Moreover, the computational model of the surrogate is more reliable when compared to the models of animal and cadaver. With the validated model, parametric study can be done which makes the study more comprehensive in nature. Since mechanical surrogates provide consistency and repeatability, they are chosen as the test objects, as described later.

CHAPTER 3: BLAST WAVE LOADING PATHWAYS IN THE SKULL BRAIN COMPLEX

3.1 INTRODUCTION

This chapter deals with the fundamental loading mechanics of the blast wave. General interaction dynamics of the blast wave and the corresponding consequences on the test subjects are studied in detail and are related to the potential injury causing mechanisms. Several theories have been proposed as potential mechanisms of the blast induced traumatic brain injury (bTBI). These theories include vascular transmission [7, 10, 49, 50]; direct transmission of the blast wave through cranium [3, 9, 51, 52]; flexure of skull [8, 23, 53]. The 15-point Glasgow Coma Scale defines the severity of injury as mild (13-15), moderate (9-12), severe (3-8), and vegetative states (<3) [54]. In mild to moderate cases of bTBI, there is no skull fracture; other pathophysiological markers in the brain are well below the detectable levels based on current neuro-imaging or serum biomarkers. This chapter addresses the biomechanical loading in these cases, where stresses in the brain results from blast wave-head interactions.

An egg shaped skull/brain surrogate model was developed for the study of head response at different orientations during blast loading [46]; spherical surrogate was developed for the study of effects of the skull opening for bTBI [47]. In this study, head (skull-brain complex) is idealized as a fluid filled circular cylinder with a longitudinal axis normal to the blast wave propagation. Brain is idealized as fluid contained in the cylinder, the latter being idealized as skull. The top and bottom of the cylinder is allowed to move freely to avoid bending along the axis during blast wave interaction and thus represents a two-dimensional analogue of the skull-brain complex.

The overall goal of this study is to understand the time-dependent spatial variation of the pressure field in the fluid when a fluid-filled cylinder is subjected to an external blast load. A theoretical framework for the blast loading of the skull - brain is developed in terms of a cylinder filled with fluid. Description about the experimental test configurations and the shock tube employed for generating idealized primary blast loading conditions are given along with the development of numerical methods.

3.2 METHODS

Primary blast induced neurotrauma (BINT) is a closed head injury; when the head interacts with the external flow field of the blast wave, the skull (the cylinder) deflects but does not fracture, whereas the brain (the fluid) is injured when the state of stress, strain and/or energy exceed some critical values. Shape (impulse) of the pressure profile [9, 16], oscillatory pressure pulses [30] and focal magnitude of pressure [55] at the neuronal level has all been identified as possible causes of the injury. Hence effect of blast wave on time-dependent pressure variation in the fluid at any given region needs to be understood in terms of the loading pathways and thus forms the main purpose of the study.

3.2.1 Theoretical Considerations

In this sub-section, a theoretical model of a blast wave interacting with a fluid-filled cylinder is developed. The blast wave flow field is described in terms of velocity and pressure as it traverses around the cylinder. The effect of this external pressure field on the stress wave and deflection experienced by the cylinder is then illustrated. These effects are then related to the fluid pressure field. It is postulated that the loading at any

given point in the fluid can be divided into two separable parts as direct and indirect loading components.

Consider a fluid-filled cylinder subjected to a blast wave, as shown in Fig. 3.1. The terminologies used in the study are shown at the end of this chapter. The pressure-time relationship of an idealized Friedlander incident wave can be written as

$$p(t) = p^* \left(1 - \frac{t}{t^*}\right) e^{-\frac{bt}{t^*}} \quad (3.1)$$

where $p(t)$ is the blast wave pressure at any time t at a given point, p^* is the peak overpressure, t^* is the positive duration of a blast wave and b is the decay constant.

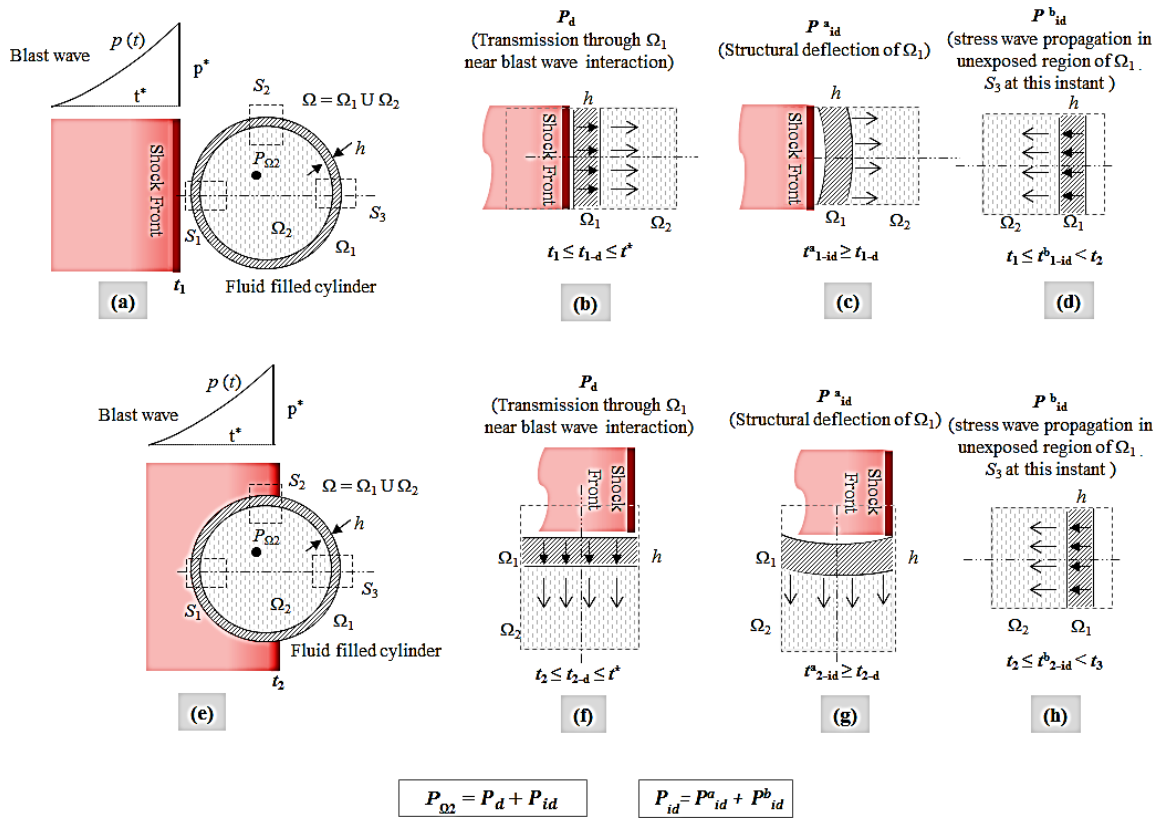


Figure 3.1 Blast wave interaction with heterogeneous body: (a) and (e) are the schematic diagrams of the loading; (b) and (f) are direct loadings; (c), (d), (e), (h) are indirect loadings.

In actual explosions, the waveforms are more complex due to reflections from ground, structures, debris and enclosures. However, for the sake of standardization, basic studies and comparisons to idealized Friedlander waveform given in Eq. 3.1 is oftentimes preferred. A generic blast wave comprises a shock front travelling with a Mach number >1 (supersonic), followed by an exponentially decaying blast wind [56]. Without loss of generality, this shock front-blast wind will be referred as the blast wave in this work. In a typical blast wave of interest, the peak overpressure p^* will be in the range of 3-4 atmospheres (0.2 to 0.3 MPa peak overpressure), with a very sharp rise time in the range of 1 or 2 μs (microsecond) and a total duration of 5 to 7 ms (millisecond). Based on these parameters, the air shock travels at a velocity of about 500 m/s and the total width of the blast wave is about 2.5 m. Compare this to total impact duration of 10-30 ms for the blunt impact with a much slower rise time [57]. As the blast encounters the fluid-filled cylinder, the mechanical pressure loading pdA occurs based on the total projected surface area of the cylinder. The loading vanishes as the external pressure reduces and lasts only for a few milliseconds concurrent with the blast wave.

Given this blast loading condition on a fluid-filled cylinder, we are interested in the state of stress at any given material point in the fluid. When we refer to the state of stress in the fluid, we primarily refer to the hydrostatic compressive stress (pressure) and use these terms interchangeably. Let $P_{\Omega_2}(t)$ indicate the state of pressure at any arbitrary point in the fluid, and it varies with time. Thus, we seek to evaluate the spatio-temporal variations of P_{Ω_2} given the entire history of blast wave going past the cylinder. Solid body of the cylinder is designated as Ω_1 and the fluid is designated as Ω_2 with the system

$\Omega=\Omega_1\cup\Omega_2$. For the purpose of categorizing the loading pathway, total loading at a given point in the fluid is partitioned into direct and indirect components, such that

$$P_{\Omega 2}=P_d+P_{id} \quad (3.2)$$

where P_d is the direct loading (direct transmission of stress waves in the region of blast wave interaction) and P_{id} is the indirect loading (esp. deflection of the shell) as shown in Fig. 3.1. Figures 3.1(a) to 3.1(d) illustrate the initial stages of blast loading on the cylindrical system. Blast wave transmission to the fluid is shown in Fig. 3.1(b). Blast wave transmission at section S_1 depends on the intensity of blast load at the section and the acoustic impedance mismatch between the cylinder-fluid interface [58, 59]. External blast load $F(t)$ at any time t is given by

$$F(t)=\int p_R(t)dA \quad (3.3)$$

where $p_R(t)$ is the reflected overpressure of blast wave acting on area dA of section S_1 . $p_R(t)$ is generally higher than the incident pressure $p(t)$; this is an important aspect of the problem and will be discussed in detail later. This blast load induces intensive compressive stress waves in the body Ω_1 . A fraction of this compressive wave is transmitted to the fluid Ω_2 . Intensity of stress transmitted (σ_t) to the fluid can be assumed by the following one dimensional expression

$$\sigma_t=\sigma_i\left(\frac{2Z_{\Omega 2}}{Z_{\Omega 1}+Z_{\Omega 2}}\right) \quad (3.4)$$

where $Z_{\Omega 1}=\rho_{\Omega 1}c_{\Omega 1}$ and $Z_{\Omega 2}=\rho_{\Omega 2}c_{\Omega 2}$ are the impedance of body Ω_1 and fluid Ω_2 respectively, σ_i is the intensity of incident wave on the interface and ρ and c are the density and acoustic velocity of the medium. Thus the magnitude of direct loading as

seen in Fig. 3.1(b) depends on the blast load and the material properties; it continuously varies as the blast wave is unloaded as given by Eq. 3.1. It should be noted that the equation (3.4) is based on one dimensional theory, and is not strictly valid for cylindrical solutions. This equation is employed to explain the loading pathway at the section level (say S_1). This equation should be viewed and used with limitations for a three dimensional problems.

Apart from direct transmission as shown in Fig. 3.1(b) the cylindrical structure gets loaded, which in turn causes not only local deflection as seen in Fig. 3.1(c) but also global deflection as the generated stress waves propagate in both directions. This local deflection due to the stress wave propagation interacts with the fluid which is the indirect component of the loading; the magnitude of the indirect load depends on the geometric and material properties of the cylinder. For instance the local displacement of a circular ring subjected to an applied concentrated load F is given by

$$\delta \propto \frac{FR^3}{EI} \quad (3.5)$$

where R is the mean radius of the cylinder, and E is the young's modulus and I is the area moment of inertia of the ring [60]. It can thus be seen that deflection decreases as the flexural rigidity is increased or the radius is decreased when all other factors are kept constant. Typical longitudinal stress wave speeds in the solid material are higher than the air shock velocity. For example, stress wave travels at 2270, 5960, and 2900 m/s in polycarbonate, steel, and skull respectively which are much higher than the typical air shock velocity of 500 m/s. Hence, stress wave travels faster in the cylinder, loads the fluid much before the arrival of the shock front as is seen in Fig. 3.1(d). This stress wave

propagation pattern causes a tensile state of stress leading to possible cavitation, depending on the magnitude of the stress vis-à-vis the vapor pressure of the fluid. Thus a typical material point $P_{\Omega 2}$ is stressed from both direct and indirect loadings.

Figures 3.1(e) to 3.1(h) depict the blast-structure-fluid interaction at a point of time when the shock front passes the mid-point of the cylinder in region S_2 . In this case, the direct loading occurs in region S_2 while the stress wave propagates from S_2 to both the sides of the cylinders. As the stress waves travel from these instantaneous loading regions, they superimpose on stress waves arriving due to previous loadings, see for example Fig. 3.1(b) to 3.1(d). Thus a very complex set of loading pattern emerges affecting the pressure at $P_{\Omega 2}$. Hence, total load at point $P_{\Omega 2}$ in the fluid is a combination of direct and indirect loads emerging at various sections of the body. Though peak values of pressures usually occur when the direct and indirect loads are both actively loading a point, this is not always the case. Though the direct load disappears when the tail of the blast wave is past the entire cylinder, indirect load due to already distorted cylinder persists until all the elastic energy is dissipated in the fluid as well as the cylinder.

3.2.2 Experiments

The blast experiments reported in this study are part of Nick Kleinschmit's thesis. Portions of the experimental setup and the configurations presented in this study are also available in his thesis [61]. The surrogate head model used in the study is subjected to planar blast waves of Friedlander type in a specially designed shock tube. A 229 mm x 229 mm steel square compression driven shock tube has been designed and tested at University of Nebraska Lincoln's (UNL) shock wave generation facility [62, 63]. This

shock tube consists of three main sections – cylindrical driver section, square driven section and a transition section between the driver and driven. The driver section contains pressurized gas (e.g. Nitrogen or Helium) which is separated from the transition by several 0.25 mm thick Mylar membranes, while the remaining sections contain air at atmospheric pressure and temperature. The cross sectional transition from circular driver to square driven is achieved with the transition section. Upon membrane rupture a blast wave is generated which expands through the transition and develops into planar blast wave in the driven section. The test section (which is part of driven section) is strategically located to expose specimens to the blast wave profile of interest. A high speed video camera is placed near the test section to capture the blast-specimen interaction events. The shock tube is designed and built such that a fully developed planar blast wave is obtained in the test section located approximately 2502 mm from the driver end; the total length of the shock tube is 12319 mm. The test location can be varied depending on the desired peak overpressure, positive duration and impulse, which in turn depend on strength of the explosive and stand-off distance of the specimen from the explosive.

A cylindrical head model (diameter 50 mm, thickness 2 mm and length 178 mm) is developed with a polycarbonate cylinder filled with mineral oil. The material of the cylindrical shell and fluid are selected such that they closely mimic the human skull and the brain respectively in terms of density and acoustic wave speed. Mineral oil is chosen over water to reduce cavitation effects. The cylinder is mounted on sliders, as shown in Fig. 3.2 so that the cylinder can easily slide (translate); this is important to eliminate bending (end) effects that might occur if the cylinder were to be rigidly mounted. In

addition, this freedom to slide is more representative of free-field blast loading experienced by a dismounted soldier.

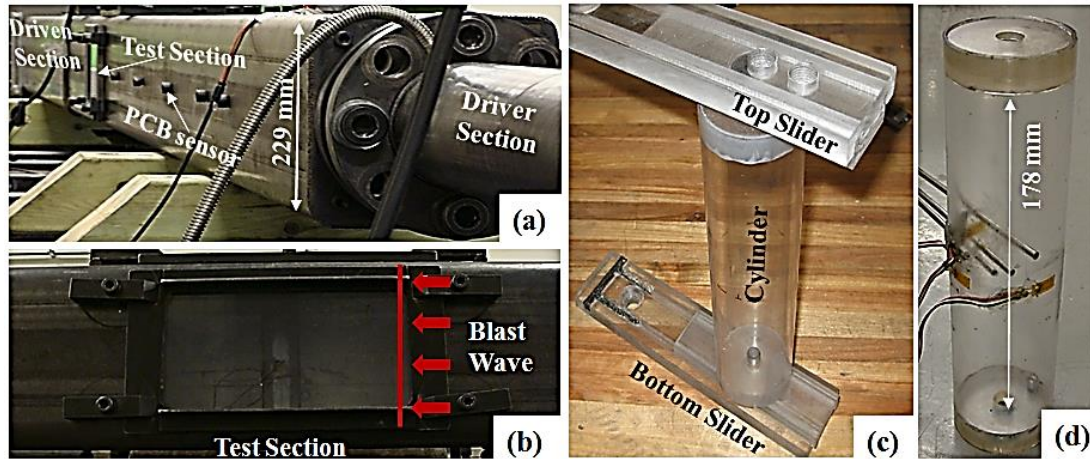


Figure 3.2 (a) A 229 mm X 229 mm steel square-12 m long shock tube used in the experiments; (b) Fluid-filled cylinder inside the test section; (c) Cylindrical system with top and bottom sliders; (d) Cylinder (without fluid for clarity) showing the surface mount pressure

Response of the cylindrical shell to the blast wave is measured with surface pressure and surface strain gauges; response of fluid is monitored with pressures sensors at different points within the fluid. The sensor configuration consist of surface mounted pressure sensors (Kulite model LE-080-250A) and circumferentially mounted Vishay strain gauges (model CEA-13-250UN-350) located at 0° (F1), 90° (M1), and 180° (B1) with respect to the oncoming shock wave. Strain gauges are glued circumferentially on cylinder surface using M-bond adhesive and they measure circumferential strain. The frequency response of the strain gauge is 1 MHz and hence can record sudden changes in strains. Surface pressure sensors are glued and taped using rubber cement and duct tape with the sensing surface exposed. Surface pressure sensors measure the reflected blast overpressures, record the arrival of blast waves and track their flow. Probe-style Kulite pressure sensors (model XCL-072-500A) that measure the fluid pressures are mounted at

the center (M2) of the tube as well as at offsets of 19 mm in front (F2) of and behind (B2) the center sensor, as shown in Fig. 3.3. These sensors are mounted inside the cylinder at an orientation perpendicular to the oncoming shock front. The three sensors are vertically aligned 7.5 mm apart with the front sensor above the center and the back sensor below it. Figure 3.3 shows the sensor configuration. Data acquisition time interval in the experiment is $1\mu\text{s}$ (microsecond), hence all sensors can capture the sudden rise due to shock loadings. The terminologies used for the sensors that are shown in Fig 3.3 (a) are as follows; F represents the front, M represents the middle, B represents the back; numerical value 1 represents outside measurement (outside shell) and 2 represents inside measurement (inside shell); P represents the pressure and S represents the strain.

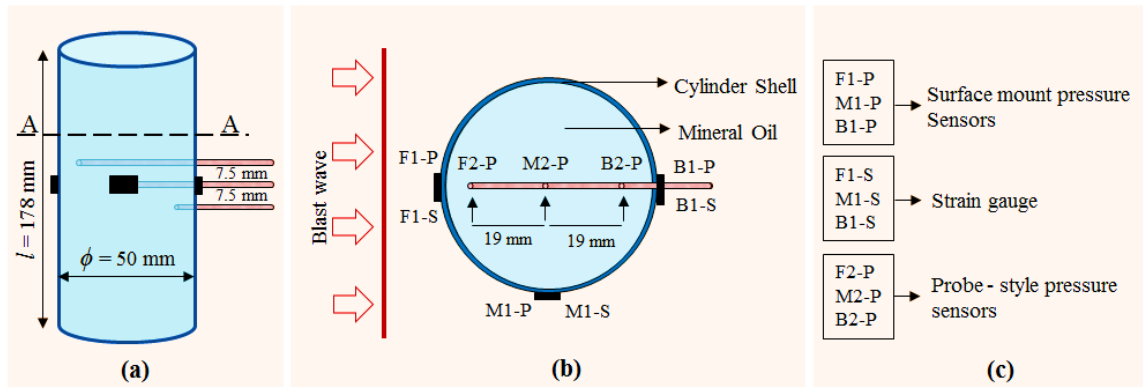


Figure 3.3 (a) Schematics of the experimental cylindrical set-up; (b) Sectional view A-A showing all the sensor locations (c) Sensor type/location terminology: First letter-F=front, M=middle, B=back; Second number-1=outside, 2=inside; Third letter-P=air surface pressure

The sensing elements can measure the absolute pressure from 0-1.72 MPa (0-250 psi) with a nominal calibration of 58.02 mV/MPa (0.400 mV/psi) using 10 volts excitation. All pressure sensors used in the experiments are calibrated under shock/dynamic loading conditions using a separate 101 mm (4") diameter shock tube. Accurate calibrations are achieved by generating precisely controlled blast wave

velocities and invoking the Rankine-Hugoniot jump conditions to relate the blast wave velocity to blast wave overpressures. Each set of experiments is repeated at least three times ($n=3$), and the numerical values are averaged. However, plots are used from a single experiment. More details about the experiments including the number of repetitions and their peak values, averages and standard deviations are all available in Nick Kleinschmit's thesis [61].

3.2.3 Computational Model

The primary purpose of the computational model is to understand the dynamics of blast loading at given shell and fluid points. Blast structure interaction is a short dynamic event and hence the explicit dynamic analysis is employed to simulate the event. Interaction between blast wave and structure is enabled by Coupled Eulerian-Lagrangian (CEL) technique. Simulated results are then compared against experimental results for the validation of the developed numerical model.

3.2.3.1 FE discretization

Finite Element (FE) modeling technique is used to simulate the propagation of a planar blast wave through the shock tube and its interaction with the cylinder. The cylinder and the fluid contained in it are modeled with Lagrangian elements. The air inside the shock tube is modeled with Eulerian elements. Schematic of the setup is shown in Fig. 3.4 (a). Eulerian framework allows modeling of highly dynamic events (e.g. shock) which will otherwise induce heavy mesh distortion. This approach has been used in the past by various researchers [16, 44, 45, 62, 64-66]. Lagrangian and Eulerian domains are meshed with 8 node brick element. Interaction between the cylindrical shell and the fluid is modeled through tied (no sliding, no separation) contact. No separation

behavior is necessary to simulate countercoup phenomena typically observed in head injuries. No separation allows tensile loads to be transferred across the interface.

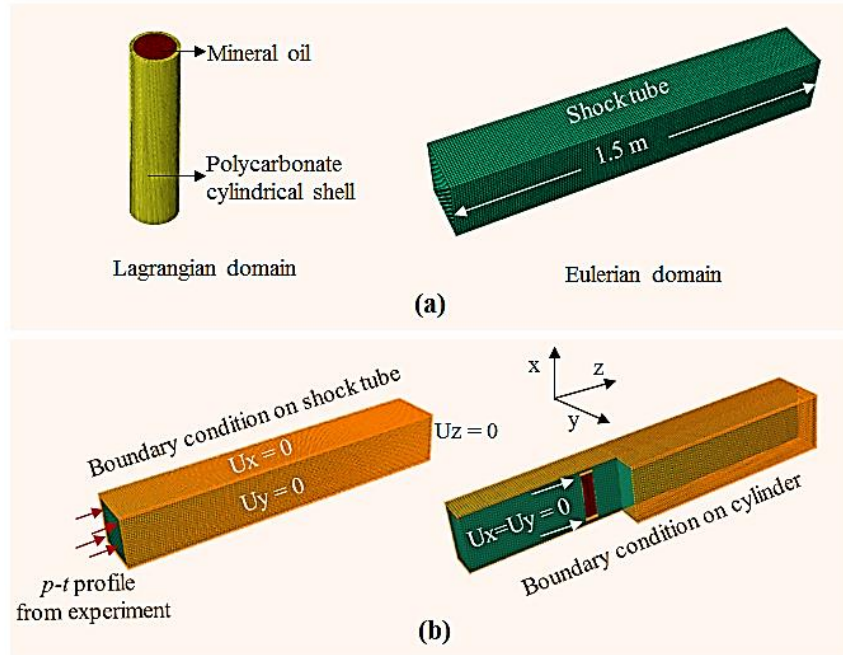


Figure 3.4 (a) FE discretization; (b) Loading and boundary conditions employed in the simulation

An enhanced immersed boundary method is used to provide the coupling between Eulerian and Lagrangian domains. Interaction between the propagating blast wave and cylindrical shell is defined through ‘general contact’ feature (card) in Abaqus[®]. In general contact, contact constraints are enforced through penalty method with finite sliding contact formulation. Various contact property models are available in general contact. In the present work, frictionless tangential sliding with hard contact is used as a contact property model. Hard contact defines pressure-overclosure relationship between contacting surfaces. Hard contact behavior implies that: 1) the surfaces transmit no contact pressure unless the nodes of the slave surface contact the master surface 2) no penetration is allowed at each constraint location and 3) there is no limit to the magnitude

of contact pressure that can be transmitted when the surfaces are in contact. Mesh convergence studies have been performed for both Eulerian and Lagrangian elements. The mesh convergence criterion is based on less than 5% change in the peak value of a given field variable (i.e. reflected overpressure, shell strain and fluid pressure). Mesh convergence is achieved at element sizes of 3 mm, 1 mm and 1 mm respectively for air, cylindrical shell and fluid inside the cylinder. Table 3.1 shows the number of nodes, number of elements, and element types for each component of the converged FE model.

Table 3.1 Finite element discretization

Model	Domain	No. of Nodes	No. of Elements	Type of Element
Air	Eulerian	1,357,360	1,316,250	Hexahedral
Polycarbonate cylinder	Lagrangian	95,823	66,740	Hexahedral
Mineral oil	Lagrangian	409,752	393,860	Hexahedral

3.2.3.2 Material Models

Air is modeled as an ideal gas equation of state (EOS) given by

$$P = (\gamma - 1) \frac{\rho}{\rho_0} e \quad (3.6)$$

where P is the pressure, γ is the specific heat ratio (1.4 for air), ρ_0 is the initial air mass density and ρ is the current mass density and e is the internal volumetric energy density. Mach number of the shock front obtained from our experiments is approximately 1.5; hence the ideal gas EOS assumption is acceptable as the ratio of specific heats does not change drastically at this Mach number. The cylindrical shell is modeled as linear, elastic, isotropic solid with the material properties of polycarbonate (base case) and steel

(parametric studies). The shell strains obtained from the experiments are less than 1%; hence linear, elastic modeling assumption is valid. The fluid contained in the cylinder is modeled with Mie-Gruneisen equation of state (EOS) that relates the final state of density (ρ) to corresponding pressure and is given by

$$P_H = \frac{\rho_0 C_0^2 \eta}{[1-s\eta]^2} \quad (3.7)$$

where, P_H is the hugoniot pressure, ρ_0 is the reference density, C_0 is the reference wave speed, $\eta = (1 - \frac{\rho_0}{\rho})$ is the nominal volumetric compressive strain, and $s = dU_s / dU_p$ is the linear Hugoniot slope coefficient. Material properties of polycarbonate and mineral oil are close to the material properties of the skull and brain respectively [67, 68]. Material properties are listed in Table 3.2.

Table 3.2 Material properties

Material	Density ₃ (kg/m ³)	Elastic/Bulk* Modulus (MPa)	Poisson Ratio	Speed of sound (m/s)	Temperature (K)	Gas Constant (J/kg-K)
-Skull	1710	5370	0.19	2900	---	---
Polycarbonate	1220	2380	0.37	2270	---	---
Brain	1040	2190*	---	1509	---	---
Mineral oil	825	1600*	---	1440	---	---
Water	1000	2400*	---	1482	---	---
Steel	7880	200000	0.3	5960	---	---
Air	1.2	---	---	347	300	287

3.2.3.3 Loading and boundary condition

Experimental pressure boundary condition (i.e. experimentally measured pressure-time ($p-t$) profile deep inside the shock tube) is used as an input for the FE

simulations. Displacement perpendicular to the faces of the shock tube is kept zero in order to avoid escaping/leaking of air through these faces as shown in Fig. 3.4(b). Hence there would be no lateral flow during shock wave propagation. Top and bottom faces of the cylindrical model are constrained in the vertical and transverse directions; the cylinder can move freely (frictionless) along the direction of blast wave propagation. It should be noted that probe holders that hold the sensors are not included in the modeling. Simulations with the probe holders are carried out in pilot studies and it is found that the probe holders do not have a significant effect on the wave propagation inside the fluid.

3.2.3.4 Solution scheme

The finite element model is solved using a nonlinear transient dynamic procedure with Coupled Eulerian-Lagrangian (CEL) method (Abaqus[®]). This approach is validated against known analytical solutions. In addition, further validation of FSI modeling using Abaqus[®] can be found in Mougeotte et al. [69]. In this approach, the governing partial differential equations for conservation of momentum, mass and energy along with material constitutive equations and equations defining the initial and the boundary conditions are solved simultaneously. In Abaqus[®] the Eulerian time incrementation algorithm is based on an operator split of the governing equations, resulting in a traditional Lagrangian phase followed by an Eulerian phase. During the Lagrangian phase of the time increment, nodes are assumed to be temporarily fixed within the material and the elements deform with the material. During Eulerian phase of the time increment, deformation is suspended, elements with significant deformation are automatically remeshed, and the corresponding material flow between neighboring elements is computed. As material flows through an Eulerian mesh, state variables are transferred

between elements by advection. In the current analysis, 8 node brick elements are employed which use isoparametric interpolation functions.

An enhanced immersed boundary method is used to provide the coupling between Eulerian and Lagrangian domains. Here, Lagrangian region resides fully or partially within Eulerian region and provides no-flow boundary conditions to the fluid in the direction normal to the local surface. Further, Eulerian region provides the pressure boundary conditions to the Lagrangian region. Thus a combination of fixed Eulerian mesh and solid-fluid interface modeling through enhanced immersed boundary method allows for concurrent simulations of the formation and propagation of primary shock wave in a fluid medium and accounts for the FSI effects and structural deformations once the shockwave encounters a solid.

In CEL, coupling between Eulerian and Lagrangian domains is two-way coupling. In our methodology, we are actually solving the whole model with the same Lagrangian equations. For the Eulerian part/domain in the model the results are simply mapped back to the original mesh. The Lagrangian (solid) body can be a deformable body and can deform based on the forces acting on it and the deformation of the Lagrangian solid influences the Eulerian part/domain.

For the current analysis, a typical simulation requires about 24 hours of CPU time on 8 dedicated Opteron parallel processors (processor speed 2.2 GHz, 2 GB memory per processor), for an integration time of 2.5 ms for a single run. In this work, automatic time stepping is used with explicit central-difference time integration. In automatic time stepping, time increment ($= \sqrt{L_{min}/C}$) is calculated at each increment for each element

based on element size and wave speed. This calculation resulted in the time step of $8.7\text{e-}8$ s for the simulations.

3.3 RESULTS

As outlined in the theoretical considerations, pressure-time variations at a given material point in the fluid are resultants of the instantaneous effects of direct and indirect loads arriving at that point. Both these loads emanating from different sources vary in magnitude and arrive at a given point from different directions. Thus the propagation process is quite complex. Only some selected features of the measured (or computed) pulse at a given point, e.g. arrival time and initial peak are typically traceable. The first section of results relates experimental measurements (Fig. 3.5) to numerical results (Fig. 3.6 through 3.8) for the purposes of model validation. It should be noted that for this set of the results, experiments and simulations are carried out on 2 mm thick polycarbonate shell filled with the mineral oil. The second section (Fig. 3.9 through 3.13) shows the parametric studies carried out to understand different loading pathways, which are addressed in detail in the discussion section. The measurements are discussed in terms of the reflected blast overpressure and strain fields in the cylindrical shell and pressure fields in the fluid.

3.3.1 Experimental Results

Table 3.3 shows the experimentally measured arrival times and corresponding calculated velocities at all sensor locations. Row 1 gives the arrival time and row 2 gives the distance travelled by the wave between sensors. The calculated velocities are shown in row 3. Wave velocities are calculated based on the distance between the sensors and differences in arrival time. Arc length of the shell is used to calculate wave velocity in the

shell whereas to calculate wave velocity in air and the fluid, direct distance (longitudinal) between the sensors is used. Blast wave velocities vary on the surface of the cylinder whereas the velocities in the shell and mineral oil are close to their longitudinal wave speeds.

Table 3.3 Experimentally measured arrival times for 2mm polycarbonate cylinder

	Blast Overpressure			Fluid pressure			Shell strain		
	F1-P	M1-P	B1-P	F2-P	M2-P	B2-P	F1-S	M1-S	B1-S
Arrival time t (μ s)	1000	1046	1138	1006	1020	1033	1004	1021	1037
Distance travelled by the waves S (mm)	0	25	50	0	19	38	0	39.25	78.5
Wave velocity dS/dt (m/s)	---	545	270	---	1357	1461	---	2308	2453
	(Blast wave - Air)			(Pressure wave - Mineral oil)			(Stress wave - Polycarbonate)		

Experimentally measured blast overpressures (F1-P, M1-P, B1-P) and longitudinal strains (F1-S, M1-S, B1-S) on the surface of the cylinder, and pressures (F2-P, M2-P, B2-P) in the fluid are shown in Fig. 3.5. Terminologies used in the designation of these locations are shown in Fig. 3.3 (c). Reflected blast overpressure at the frontal location (F1) shows a very sharp rise followed by a decaying pressure pattern (Fig. 3.5(b)). The peak overpressure at location F1 is amplified 2.5 times the incident pressure. Peak overpressures at side (M1) and rear (B1) are significantly lower ($\Lambda_{M1} = 0.63$ and $\Lambda_{B1} = 0.94$) than the reflected overpressure at the front (F1) ($\Lambda_{F1} = 2.5$); all three pressure pulses begin to equilibrate after about 4 ms. Small secondary peak observed in the pressure profile at $t=1.6$ ms is due to the side wall reflection from the blast tube. Using

numerical simulations, it is found that the secondary reflection has very minimal effects on the pressure pulses observed in the fluid.

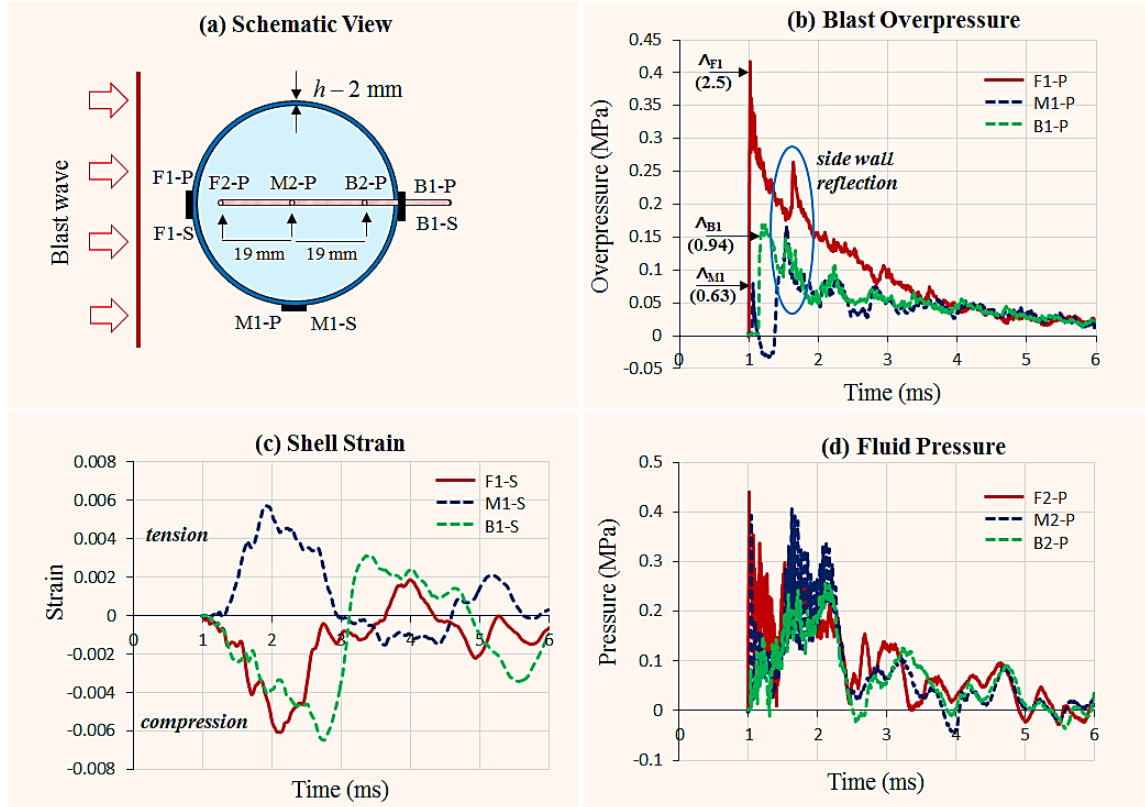


Figure 3.5 Experimental measurements at various locations (a) schematic view of measurement locations; (b) external blast overpressures; (c) cylindrical shell strain; (d) pressure pulse in the fluid.

Surface mounted strain gauges (F1-S, M1-S and B1-S) measure negative (compressive), positive (tensile) and negative (compressive) strains, respectively as shown in Fig. 3.5 (c). Strain measure indicates that the front section undergoes compression while the middle section is under tension, i.e., the circular cylinder becomes elliptical with major axis passing through M1 and perpendicular to the flow and minor axis passing through F1 and B1. The fluid pressure measured at F2 (Fig. 3.5 (d)) shows a sharp pressure rise followed by pressure decay (till $t=1.5 \text{ ms}$). This is attributed to transmission of pressure from the surface (F1-P) to the fluid. After $t=1.5 \text{ ms}$ the pressure

is again increased (secondary rise). This secondary rise is attributed to shell deformation. The pressure eventually dies down at $t=2.5$ ms. Fluid pressures at M2 and B2 show similar trend but the initial magnitude of peak pressure is reduced as we go from F2-M2-B2. In addition M2 shows significantly higher oscillations as compared to sensor F2 and B2.

3.3.2 Numerical Model Validation

For numerical model validation, firstly convergence study is performed. Once the convergence criteria are met, then the material model (e.g. density, elastic modulus) used in the simulation are varied within the available range for a better match with the experiments. As mentioned in the computation section, 5% change in the peak value of the variable is used as a convergence criterion. Once this is achieved, simulations for different combinations of the available density and elastic modulus of polycarbonate shell and the available density and acoustic wave velocity of mineral oil are carried out to obtain a right numerical model of the experiment. Analysis and parametric study are carried out on this final numerical model to draw the final conclusions. The material properties used in the final numerical model are listed in Table 3.2. Figure 3.6 shows the numerical results of blast overpressures at experimental locations, superimposed with the experimental data for comparison purposes. It should be noted that for ease of comparison, the shock wave arrival times of the simulations are shifted to match the experimental arrival times. Simulated blast overpressures are in good agreement with the experimental data. Simulation is able to capture the main features like shock front, peak pressure, negative phase and secondary rise.

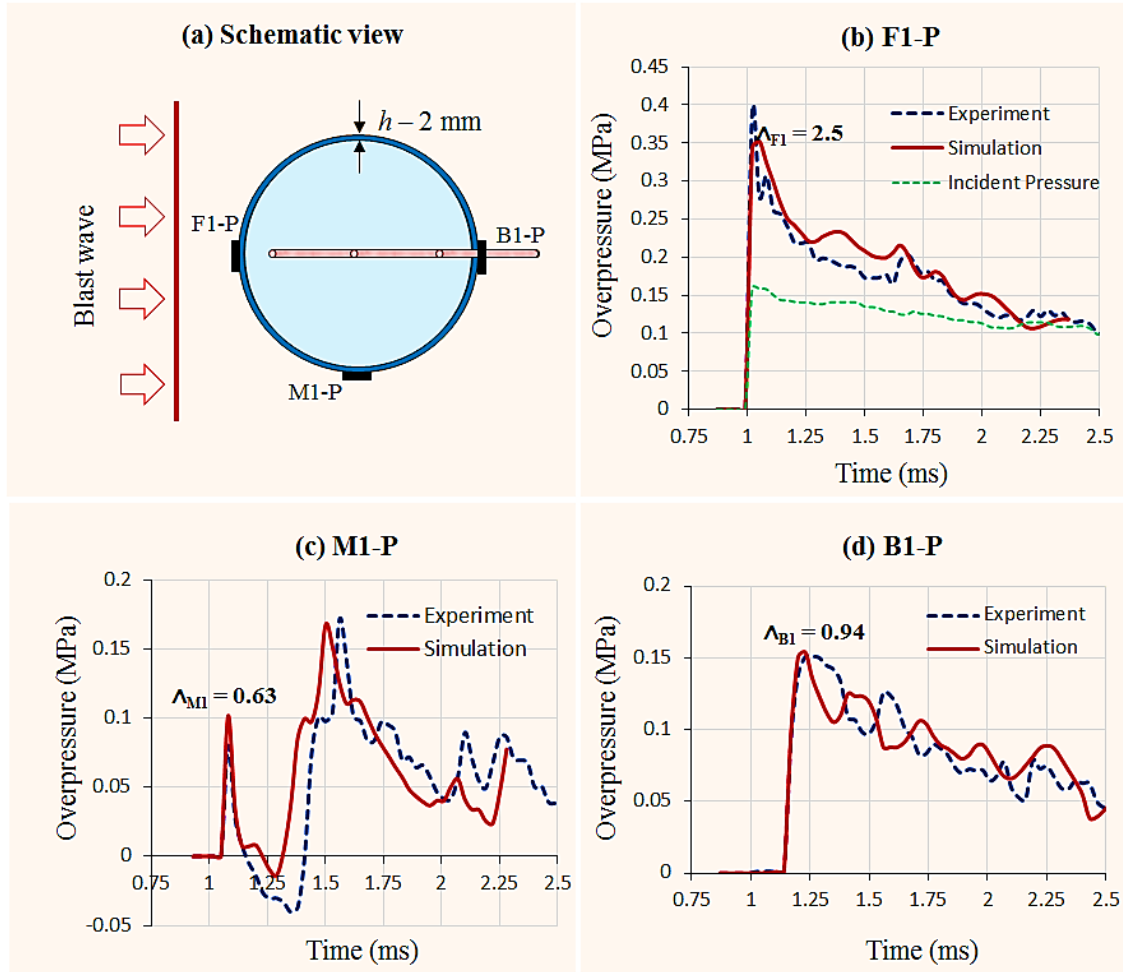


Figure 3.6 Comparison of experimental and numerical blast pressures at three locations: (a) schematic; (b) front; (c) middle; (d) back.

Comparison between experimental and numerical strains at location F1, M1 and B1 are shown in Fig. 3.7. The simulation results agree with the experimental data and predict the same pattern of compression, tension and compression at locations F1, M1 and B1 respectively. Shape change from circle to ellipse (Fig. 3.7(a)) is clearly captured in the simulation.

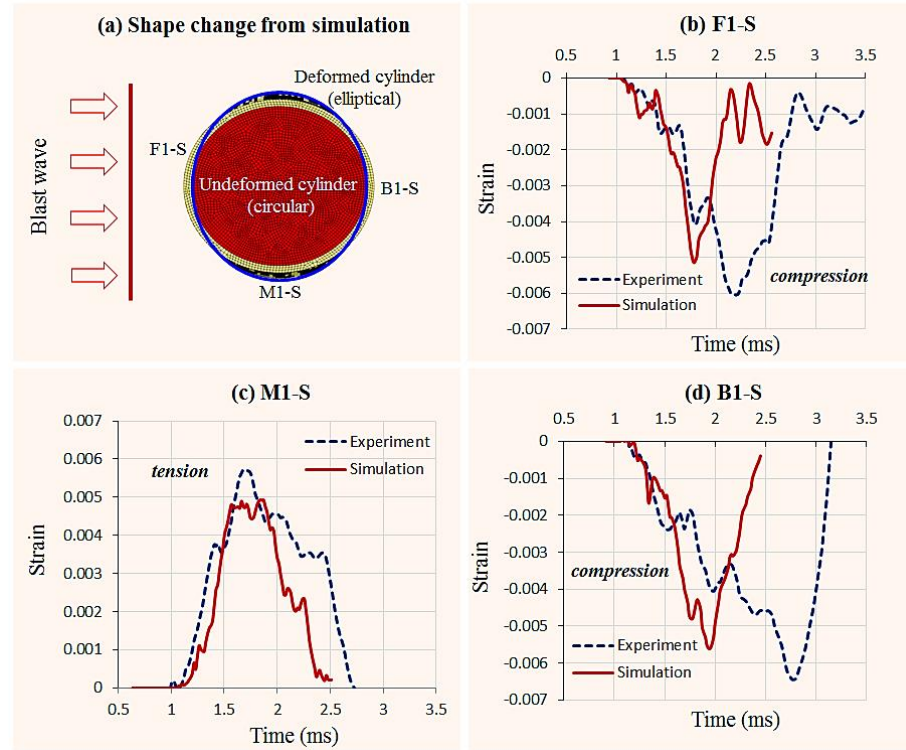


Figure 3.7 Comparison of experimental and numerical shell strains at three locations: (a) shape change of the cylinder from circle to ellipse obtained from simulation (b) front; (c) middle; and (d) back.

Comparison of fluid pressures between the experiment and numerical simulations at location F2, M2 and B2 are shown in Fig. 3.8. For ease of comparison, pressure profiles obtained from the simulation are filtered at 15 kHz. The simulated pressure profiles show a similar pattern as that of the experiments. At location F2, the sharp pressure rise from the simulation is consistent with the shock front rise time from the experiments. Response of pressure gauge at M2 (geometric center) shows the trend of a pressure pulse superimposed by a periodic oscillation. The period of oscillation corresponds to the round trip travel time of an acoustic stress wave across the interior of the cylinder (23 mm radial distance in 16 μ s). At location B2, simulation captures pressure rises due to direct (transmission) and indirect (deflection) loading that is consistent with the experimental results.

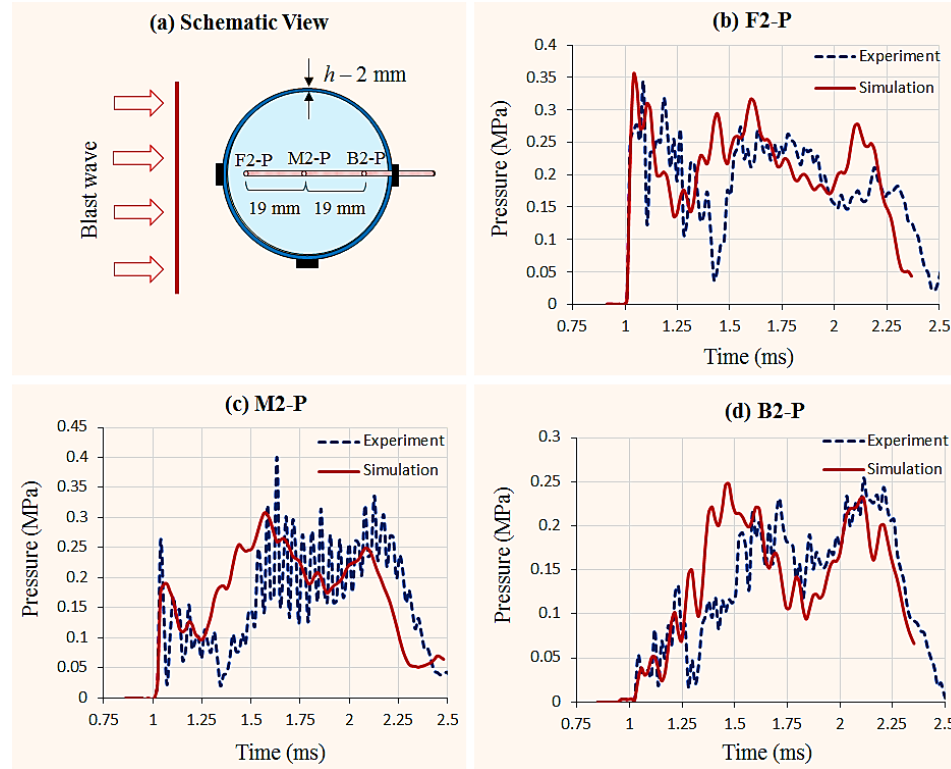


Figure 3.8 Comparison of experimental and numerical simulation results at three locations inside the fluid: (a) schematics; (b) front; (c) middle - pressure oscillations corresponding to the round trip wave motion; and (d) back.

Though simulation results match fairly well with the experimental results, some discrepancies in the experimental and simulation data are observed. In the simulations, shock wave travels faster than the experiments and the difference is of the order of 0.2 ms. This difference in velocity between experiment and simulation is attributed to the ideal gas equation of state modeling assumption, membrane rupture pattern and the friction along the inner wall of the shock tube [44-46, 62]. However, for ease of comparison between experimental data and simulation results, the shock wave arrival times of the simulations are shifted so that arrival times match with the experiments. It is not only the shock front, but the entire blast wave (including shock foot or tail) travels faster in the simulation. A similar trend is observed in our previous works [44, 45, 62].

Due to differences in shock wave velocities though the mismatch between experiments and simulation in the pulse decay region appears to be out of phase, it can be partially attributed to the velocity mismatch. The authors have performed Fast Fourier Transform (FFT) analysis of experimental and computational data. From the FFT analysis, it is seen that the dominant frequencies of the oscillations are similar in the experiments and simulations. Another factor that needs to be considered for the mismatches between the experiment and simulation is the measurement point. Since the pressure and strain measurement points in the simulation are not exact as in the experiments, some mismatches are anticipated. In the simulation, the measurement points are mostly confined with an element whereas in the experiment, the measurement point is the sensing region of the sensor. Hence, there are some differences in the location and region of measurement. For instance, in case of strain measurements, the length of the sensing region of the strain gauge in the experiment is around 6.5 mm whereas in simulation it is around 2 mm.

3.3.3 Parametric studies on cylindrical head model

The results of numerical simulations match the experimental data fairly well; in-depth analyses of the effect of different parameters are provided in this section. Since the pressure field in the fluid is affected by the structural (material/geometry) response of the cylinder, both material and thickness of the cylinder are independently varied for the study.

Effect of material and thickness of the cylinder on fluid pressures are shown in Fig. 3.9. Two thicknesses (2 and 7 mm) and two materials (polycarbonate and steel) are

used in the study. Peak pressures at F2 are reduced as the shell material is changed from polycarbonate to steel. In addition, sensor B2 shows negative pressure (initial pressure rise) in case of steel (Fig. 3.9(c) & (f)), whereas for polycarbonate positive pressure (initial pressure rise) is observed at B2 (Fig. 3.9(b) & (e)). Similarly as the shell thickness is increased from 2 mm to 7 mm the peak pressures are reduced for both polycarbonate (Fig. 3.9(b) & (e)) and steel (Fig. 3.9(c) & (f)). Apart from the magnitude, other patterns in the pressure profiles remain unchanged for 2 mm and 7 mm steel cases as seen in Fig. 3.9(c) & (f). But for polycarbonate case, patterns in the pressure profiles vary substantially between 2 mm and 7 mm as seen in Fig. 3.9(b) & (e).

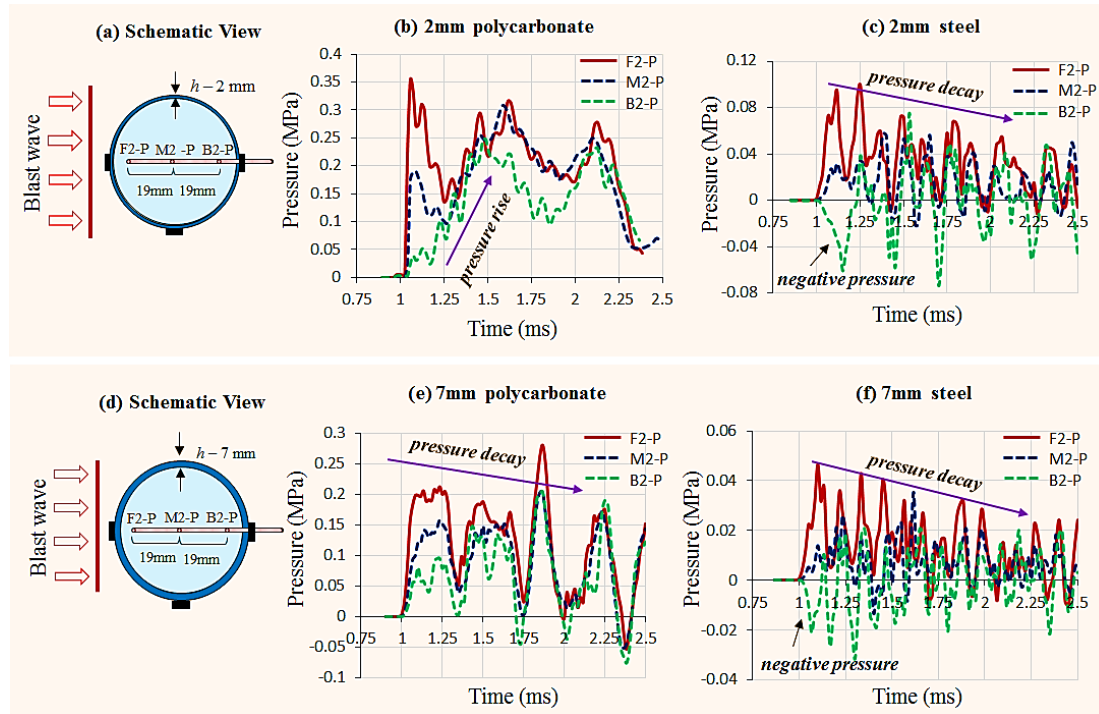


Figure 3.9 Numerical simulations of pressure pulse: Top row- 2mm polycarbonate/steel; Bottom row-7mm polycarbonate/steel; Pressure rise in fig (b) corresponds to deflection-dominated indirect loads, absent in other cases.

3.4. DISCUSSIONS

It can be seen from the previous sections that the pressure in the fluid is a complex function of external blast flow dynamics, geometry/material of the cylinder and acoustic velocity of the fluid. In order to fully understand the mechanics of the direct transmissive load and the structural deflection-induced indirect loads, it is important to pare down the sequence of different wave motions arriving at a point, by monitoring the time of arrival of different waves. The very first response of either the external surface pressure, strain, or the internal fluid pressure will indicate the arrival of different waves.

3.4.1 Arrival time analysis

Arrival time analysis of the experimentally measured values in the case of the 2 mm polycarbonate case is shown in Table 3.3. From the table, it can be seen that the flow velocity around the cylinder between F1 and M1 (anterior to lateral) is 550 m/s and flow velocity between M1 and B1 (lateral to posterior) is 270 m/s. Compare these velocities to the far-field shock velocity of 500 m/s. Hence, there is a speed-up from anterior to mid-point (lateral) and slow-down from the mid-point to the posterior location. This speed-up and slow-down process is due to the blast wave and cylinder interaction dynamics (Fig. 3.10). As the shock front impinges on the cylinder at its most upstream region (see Fig. 3.1, region S_1), a reflected shock propagating in the opposite direction starts to develop. At the same time, regular reflections occur that propagate radially and in the upstream direction. Thus, a compressive pattern of variable strength develops as a result of incident shock reflection over the surface and upstream motion of the blast wave. At an angle of about 45° from the leading-edge radius, Mach reflection takes place. In this region, the shock foot propagates faster than the shock front. At 90° , the shock foot has the same speed as the shock front. At angles greater than 90° , the shock foot starts to slow down

relative to the shock front resulting in generation of expansion waves. These expansion waves are formed after the shockwave passes the top point of the cylinder at 90° from the leading edge. At an angle of 180° from the leading edge, blast traversing from the sides of the cylinder meet (flow union) resulting in higher pressure as compared to the pressure at 90° . Similar observations are reported by Ofengeim et al.[70].

It is critical to understand the wave propagation in the cylindrical shell and the fluid. Based on the arrival time analysis of strain gauges at F1, M1 and B1, stress wave velocity in the cylindrical shell is 2400 ± 100 m/s (Table 3.3). This calculated wave velocity is close to the longitudinal wave speed of polycarbonate (2270 m/s). Similarly, calculated wave velocity (1450 ± 110 m/s) in the fluid from the arrival time analysis is close to the longitudinal wave speed of the fluid (1440 m/s).

The arrival of the pressure wave at the front sensor (F2) in the fluid is $6 \mu\text{s}$ after the arrival of the surface pressure wave at sensor F1 (Table 3.3). This indicates that pressure wave in the fluid is due to the direct transmission of the blast wave. Once the wave is initiated in the fluid, it travels at the longitudinal wave speed of the fluid and accounts for the initial sharp pressure rise at sensor M2 and B2.

3.4.2 Pressure Magnitude

3.4.2.1 Blast Load

It needs to be recognized that the blast wave is a moving load with the shock front (head of the blast wave) inducing much higher load compared to that of the tail. The magnitude of this moving load inflicted on the structure is primarily determined by the area involved in the blast-structure interaction region and the corresponding reflected

blast overpressure at that region as given in Eq. 3.3. Reflected blast overpressure can be expressed as an amplification ratio of the blast wave and is given by

$$\Lambda = \frac{p_R(t)}{p_i(t)} \quad (3.8)$$

where $p_R(t)$ and $p_i(t)$ are incident and reflected overpressures of a blast wave, respectively. The reflected overpressure range for an air shock is within $2 \leq \Lambda \leq 8$. Value of Λ depends on (a) the relative orientation of surface normal to the blast wave flow direction, (b) rigidity of surface (yielding or unyielding), (c) velocity of the shock wave (or its Mach number) and (d) geometry, material and stiffness of the object [71].

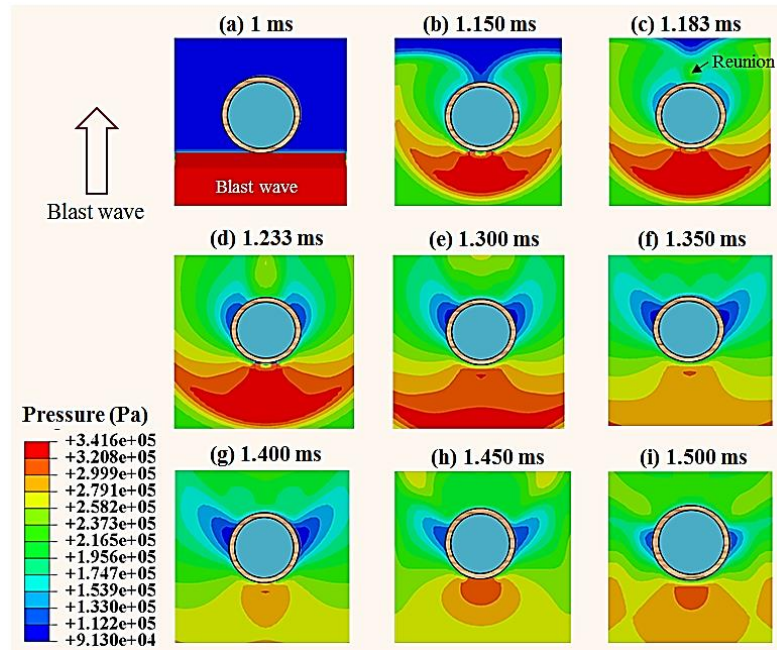


Figure 3.10 Numerical simulation of external flow field at different time points: (a) to (c) show the reflected wave fronts moving upstream; (d) to (f) show the evolution of low pressure region.

From the interaction pattern of blast wave with cylinder, it is clear that the blast wave impinges normal to the cylindrical surface in frontal interaction (F1) leading to high Λ_{F1} ($=2.5$) where both static and dynamic pressures are involved. When the blast wave

approaches the sides (M1) the entire front half is engulfed in blast loading with structural loading per unit area (local traction) changing due to two reasons: (i) Reflection ratio (Λ) changes as a function of the angle between the blast propagation direction and the local normal to the surface. At this point, the flow is almost parallel to the sides (M1) and has a minimum value of Λ since only static pressure is involved in the interaction, and (ii) very presence of the cylinder which changes flow dynamics as blast wave traverses from the front (F1) to sides (M1) (see Fig. 3.10). At the rear (B1), the blast wave traversing the both sides of the cylinder reunites (Fig. 3.10(c)) thus leading to higher amplification (Λ_{B1} (0.94)) compared to the middle (Λ_{M1} (0.63)). Thus direct load changes around the periphery as the reflection ratio Λ changes. It turns out that the magnitude of pressure generated in the fluid is highest at the front (F2) and is due the direct transmission of the blast overpressure from the surface (F1).

3.4.2.2 Impedance mismatch

The magnitude of the pressure transmitted to the fluid due to blast interaction depends on the reflected pressure and the impedance mismatch. Pressure transmitted to the fluid is assumed by the following expression

$$\sigma_t = \sigma_i \left(\frac{2Z_{\Omega m}}{Z_{\Omega p} + Z_{\Omega m}} \right) \quad (3.9)$$

where σ_i is the incident stress wave impinging on the interface between polycarbonate and mineral oil, σ_t is the stress wave transmitted to the mineral oil and $Z_{\Omega m}$ and $Z_{\Omega p}$ are the impedance of mineral oil and polycarbonate respectively. Steel has a much higher impedance (47 MPa-s/m) compared to polycarbonate (2.76 MPa-s/m) and mineral oil (1.2 MPa-s/m). Based on these impedances, the intensity of stress wave transmitted to the

fluid in the polycarbonate case ($\sigma_t = 0.61\sigma_i$) is higher than the steel case ($\sigma_t = 0.049\sigma_i$). Hence, higher the impedance mismatch, lesser is the transmission [46, 48, 58]. Thus the magnitude of pressure waves in the fluid for 2 mm steel case is less compared to 2 mm polycarbonate case. As the impedance mismatch determines the magnitude of transmitted waves, it can be concluded that direct load is inversely proportional to impedance mismatch.

3.4.2.3 Shell Thickness

Figure 3.9 clearly shows that the pressure transmission reduces with increase in thickness. Though 2 mm and 7 mm polycarbonate cases have the same impedance mismatch, peak pressure in the fluid for 7 mm thick shell is lesser than the 2 mm case. A similar trend is also observed in 2 mm and 7 mm steel cases. Thus, it is clear that the blast wave transmission reduces with increase in shell thickness.

When the cylinder is subjected to shock loading (see Fig. 3.1, region S_1), there is a direct transmission of stress followed by the indirect loading due to shell deflection. While the direct load is determined by the impedance mismatch condition (acoustic response), the deformation of the cylinder in the vicinity of the loading is determined by the structural response. The structural response is measured in terms of flexure rigidity (EI) where E is the modulus of elasticity and I is moment of inertia. EI not only controls the structural response but also determines the wave speed. For the same diameter of the cylinder, an increase in thickness leads to increase in the moment of inertia, and hence lower deflection. Stress in the fluid arising due to the shell deflection is indirect load; this indirect load is maximum for 2 mm polycarbonate and it reduces for 7 mm polycarbonate. For 2 mm and 7 mm steel cases it still reduces further (Fig. 3.9). Thus as

the structural rigidity of the cylinder is increased either through an increase in the modulus of elasticity or/and thickness of the shell, indirect load to the fluid decreases.

3.4.3 Correlation between fluid pressure and shell strain

In the previous sections it is shown that an initial pressure rise in the fluid is due to transmission of blast wave to the fluid and is governed by blast wave-cylinder interactions at the anterior portion (see Fig. 3.1, region S_1) of the cylinder. In this section, the relation between fluid pressure and surface strains is illustrated. Figure 3.11 compares the (circumferential) strain in the cylinder at side (M1) with the fluid pressure at the center of the cylinder (M2), for 2 mm polycarbonate case.

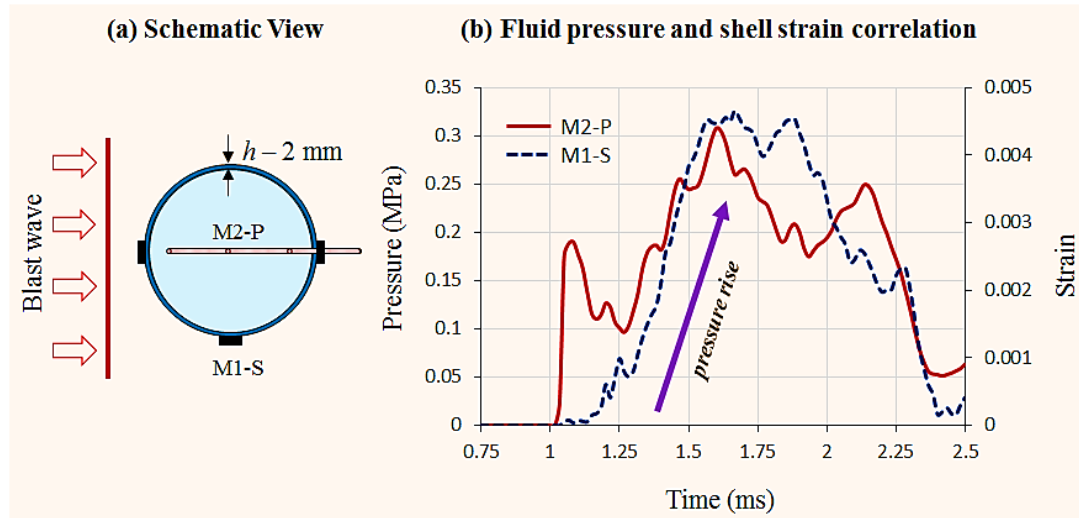


Figure 3.11 Comparison of external deformation of the cylinder (strain at M1) and fluid pressure in M2 in 2 mm polycarbonate-oil system: (a) Schematic; (b) Concurrent pressure rise in fluid and strain indicating indirect load.

From the figure, it can be seen that the rise and fall of the pressure in the fluid is strongly related to the strain variation in the cylinder. Further, the pressure pulse is a combination of internal wave reflections in fluid and shell deflection (indirect load). This then explains the pressure rise observed in Fig. 3.9 (b) for all the three fluid pressure data.

For 7 mm polycarbonate and for both the 2 and 7 mm steel cases shell deflections are limited and hence there is no significant pressure rise. Thus, pressure decays with time for these cases as shown in Fig. 3.9 (c), (e) and (f). Hence indirect load (deflection of the shell) has a significant effect on the fluid pressure.

3.4.4 Coup-Countercoup effect

Coup-countercoup effect is common in blunt impacts that are primarily due to the relative motion of the skull and the brain [72-74]. However Coup-countercoup effect in BINT [8, 46, 75-77] may or may not be due to this relative motion, since head acceleration is significantly less, at least during the time point of our investigation (first 2.5 ms) [8].

Negative pressures are observed at the rear end (B2) of the fluid in the steel case and are absent in the polycarbonate case (Fig. 3.9). Thus the present study clearly shows that the coup-countercoup effect in BINT is dictated by the wave propagation within the shell compared to that in the fluid as shown in Fig. 3.1(e), and not by global acceleration/deceleration effects. This is explained with the help of simulations.

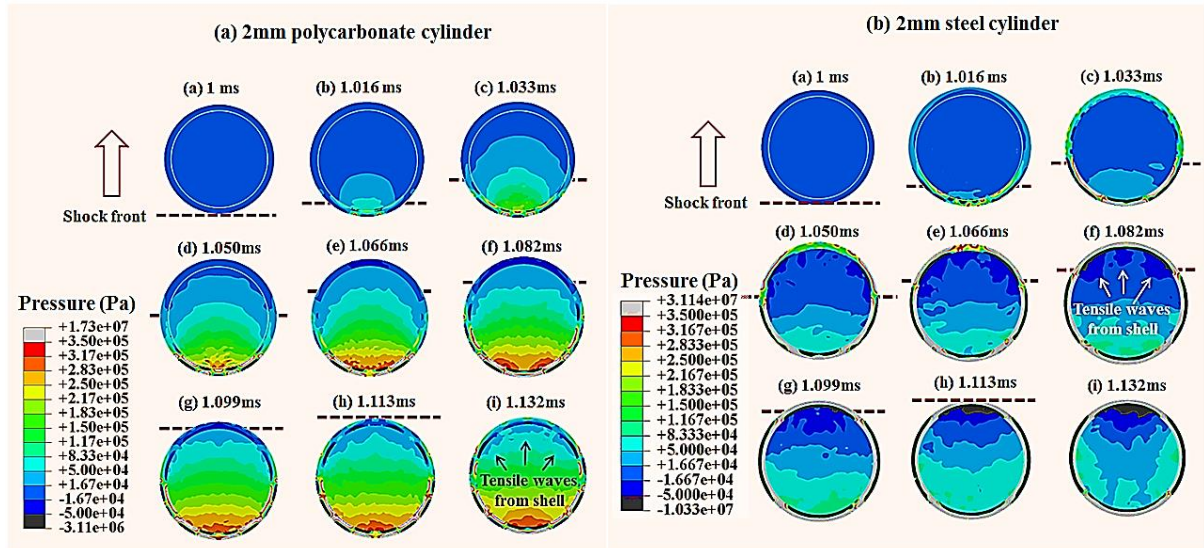


Figure 3.12 Wave propagation in 2mm shell and fluid at different time points: (a) polycarbonate (b) steel- with the external shock front shown in dotted line.

Figure 3.12 shows the pressure/stress waves in the fluid/shell for both 2 mm polycarbonate and steel cases at various time points of interest; here the latter shows the countercoup effect while the former does not. In steel case, compressive stress waves generated in the shell at the blast impinging region (F1) travel along the shell (F1-M1-B1) and transmits tensile (expansion) wave to the fluid near B2. Stress wave velocity in steel is approximately 4 times higher than that in the fluid, and hence produces countercoup effect. In polycarbonate case, the time taken by the stress waves to travel along the circumference (F1-M1-B1) of the shell is longer than the time taken by the pressure wave (F2) in the fluid to travel across the cylinder (F2-M2-B2); hence there is no countercoup effect. Thus, indirect load can induce negative pressures (tension) when the acoustic velocity in the solid is much higher than that in the fluid.

3.4.5 Effect of cylinder radius

The 25 mm radius polycarbonate cylinder used in the experiments corresponds to the head of small animal (e.g. rodents) specimens that are frequently tested in BINT studies [16, 23]. However, the applicability of this model to human head is not so obvious. For this reason, numerical analysis is conducted on a 75 mm radius polycarbonate cylinder (2 mm thick) subjected to similar blast loading conditions. Radius of 75 mm is reasonably similar to the average dimensions of a human head.

Figure 3.13 shows the comparison of fluid pressure and shell strain between 25 mm and 75 mm cylinder radius cases. The pressure patterns for 75 mm cylinder at all locations (F2, M2 and B2) are similar to 25 mm cylinder. Deflection of the shell is less in 75 mm cylinder due to increase in the flexural rigidity; thus the deflection induced load (indirect load) reduces. Oscillations similar to that of 25 mm case are observed at the fluid center (M2), but its frequency is different due to changes in wave propagation distance. Differences in oscillation frequencies are also seen between our experimental data on rat ($r \sim 15$ mm) and PMHS ($r \sim 75$ mm) (unpublished work; manuscript in preparation). The wave arrival times at F2, M2 and B2 for 75 mm cylinder yield the same acoustic velocity of fluid as that of 25 mm cylinder case.

Hence the results obtained for the 2 mm thick polycarbonate cylinder with 75 mm diameter can be applied to human head in terms of the loading path and pressure pulses in the fluid. However, as the geometry of the human skull is much more complex with thickness varying from 2 mm to 7mm, care should be exercised while applying these results.

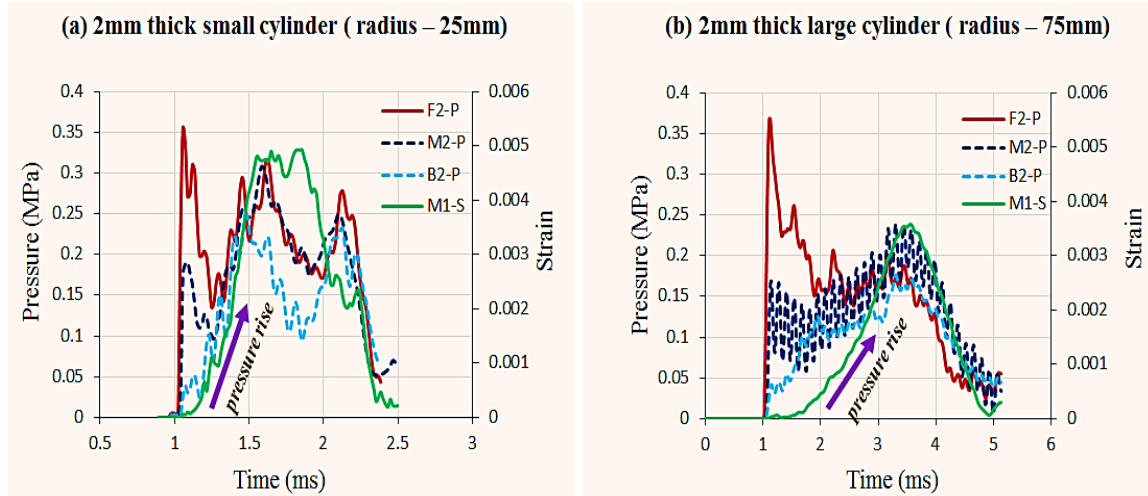


Figure 3.13 Comparison of fluid pressures and external deformation of the cylinder (strain at M1) (a) 25 mm radius cylinder (b) 75 mm radius cylinder.

Some of the limitations in this study are: (i) A fluid filled cylinder is used as a surrogate head; thus all the results should be viewed in qualitative terms as response of human head will vary due to variations in geometry and materials. (ii) While studying the response of the fluid filled cylinder to the blast wave, we are mainly focused on key parameters like peak pressure and the shape of the pressure pulse inside the fluid due to the blast wave. Thus many aspects of blast physics like Mach reflection, flow field around the cylinder are not studied in great detail. The problem of shock wave interaction with the structure can be very complex depending upon nature of the problem (e.g. viscous vs. inviscid fluids, boundary layer effects) and the goal of the research work. (iii) Only positive phase of the blast wave is considered in this work hence effects of negative phase on fluid pressure inside the cylindrical cavity are not studied. (iv) Mineral oil is used as brain simulant which is less susceptible to cavitation and hence cavitation effects are not studied in this work.

3.5 CONCLUSIONS

From the study presented in this chapter, we have figured out a few fundamental injury-causing mechanisms. Based on experimental measurements and validated computational modeling, the following conclusions can be made. They are:

- Blast flow field around the cylinder is governed by the geometry of the cylinder. The amplification factor Λ (ratio of reflected overpressure on the cylinder surface to that of far-field side-on incident pressure) is governed by orientation of the cylinder with respect to the direction of blast wave propagation, and the dynamics of fluid-structure interaction. Λ is maximum in the frontal section and reduces in the middle and the posterior sections. Hence the loading in the frontal section greatly determines the biomechanical loading of the shell and the fluid.
- The total load at a point in the fluid can be partitioned into direct and indirect loads. Direct load is the stress wave transmitted from the blast to the cylinder and then to the fluid and is governed by the acoustic impedance mismatch. Higher the mismatch, lower is the transmission. Indirect load is the loading arising from the deflection of the container that loads the fluid, and this is governed by material stiffness and thickness of the shell. Higher the stiffness or/and the thickness, lesser is the indirect load.
- The cylindrical shell changes its shape from a circular cross-section to elliptical and then restores back to a circle, in the case of deflection-dominated thin cylinders. For thick cylinders the shape change is minimal. The shape change induces a rising pressure response in the fluid that is absent for thick cylinders.

- Pressure history in the fluid is governed by the interaction of multiple waves emanating from different points.
- In the ranges of air blast (field-relevant) load, peak pressure at any given point in the fluid is governed by direct transmissive load. The duration of impulsive pressure load is governed by deflection-induced indirect loads.
- Based on the time difference in the stress wave propagation of the solid and the fluid, in some special cases, negative pressures can occur in the contrecoup region; this is indirect load and can possibly lead to cavitation in the fluid.

NOMENCLATURE

p^*	Blast wave peak overpressure
$p(t)$	Blast wave overpressure at time t
t^*	Positive duration of blast wave
Ω	Heterogeneous body ($\Omega_1 \cup \Omega_2$)
Ω_1	Homogenous shell medium
Ω_2	Homogenous fluid medium
h	Shell thickness of Ω_1
S_1	Section 1 in heterogeneous body
S_2	Section 2 in heterogeneous body
S_3	Section 3 in heterogeneous body
t_1	Time at which shock front interacts with S_1
t_2	Time at which shock front interacts with S_2
t_3	Time at which shock front interacts with S_3
P_{Ω_2}	Total load at any point in medium Ω_2
P_1	Load at any point in fluid Ω_2 from section 1
P_2	Load at any point in fluid Ω_2 from section 2
P_d	Direct load (transmission from shell near blast wave interaction)

P_{id}	Indirect load ($P_{id}^a + P_{id}^b$)
P_{id}^a	Indirect load due to structural deflection of shell
P_{id}^b	Indirect load due to stress wave propagation in unexposed region of Ω_1
t_{1-d}	Duration of direct load (P_d) from section 1
t_{1-id}^a	Duration of indirect load (P_{id}^a) from section 1
t_{1-id}^b	Duration of indirect load (P_{id}^b) from section 1
t_{2-d}	Duration of direct load (P_d) from section 2
t_{2-id}^a	Duration of indirect load (P_{id}^a) from section 2
t_{2-id}^b	Duration of indirect load (P_{id}^b) from section 2

CHAPTER 4: RELATIONSHIP BETWEEN BLASTWAVE INTENSITY, SKULL THICKNESS AND INTRACRANIAL PRESSURE

4.1 INTRODUCTION

In the previous chapter, we analyzed the shock structure interaction leading to TBI. One of the main conclusions from the study was that the intensity of pressure transmitted to the fluid reduces with increase in the thickness of the cylindrical shell. This finding is further explored in this chapter. The motivation behind this study is the use of different thickness study models in TBI studies. Each thickness study model will have distinct effects in the brain surrogate for a similar blast loading condition. Hence, it is important to study the effect of the thickness of the model. The test subjects commonly employed for bTBI study include post mortem human subjects (PMHS-human cadavers)/computational head models [77-79], animal models [23, 39, 80, 81]mechanical head surrogates [46, 48, 82] and in-vitro injury models of single cells to 3D cultures [24, 25]. The type and intensity of blast wave employed in each of these test subjects are quite different, since different intensities can introduce the same pathophysiological conditions depending on the skull thickness and geometry. For example, lower intensities of blast wave can cause the same level of injury in rats compared to that of pigs, the latter endowed with thicker skulls [39, 83]. In this work, it is hypothesized that the magnitude of intracranial pressure (ICP) dictates the probability of injury both in the acute and chronic stages [9, 30, 55]; hence, we seek to relate ICP to primary blast wave and skull geometry/thickness.

Skull thickness of human head (≈ 2 mm to 8 mm), animal models (≈ 0.2 mm to 10 mm) and mechanical head surrogate models (≈ 3 mm to 7 mm) are all quite different, and vary from 0.2 mm to 10 mm. Hence for a given BOP, the ICP generated in these models varies with respect to thickness of the skull.

Table 4.1 bTBI study conducted on different test subjects

Test Subjects	Skull thickness (mm)	Incident pressure (kPa)	Intracranial pressure (kPa)	Author and year
Mouse	0.2-0.7	68-105	--	Cernak 2011
Rat	0.29-0.71	69-117	100-187	Bolander 2011
Ferret	---	98-837	--	Rafaels 2010
Pig	9.74	110-740	80-390	Shridharani 2012
Polyethylene (skull) -silicone gel (brain)	3	77	55-60	Zhu 2011
Polyurethane (skull) - gelatin (brain)	7	35-40	20-25	Varas 2011
Poly(methylmethacrylate) (skull) - synthetic gelatin (brain)	---	100-744	2000-3500	Alley 2011
Idealized head model	---	490-1400	3000-5600	Zhang 2009
Computational head model (visible human project)	2-7	1300	3000-4000	Taylor 2009
Post mortem human subjects (PMHS)	2-7	70-103	124-220	Bir 2011

Table 4.1 lists some of the commonly used head models and their thicknesses with incident BOP conditions and the corresponding ICP generated in those conditions. These variations in skull thickness, BOP and ICP increase the variabilities in bTBI studies and also complicate the comparison of results between any two bTBI studies involving different kinds of test subjects and different ranges of BOP. Furthermore, the experimental data of ICP measured in the rat models by our group as well as other groups

vary with respect to ROP. The ICP also tends to vary with respect to the thickness of the skull. Hence it is apparent that both ROP and skull thickness influence the ICP. These findings motivate the study of the relationship between these three parameters. To establish the relationship between these three parameters a simple fluid filled cylindrical model, a surrogate for the rodent head is chosen for the study. The variabilities in the model are kept to a minimum.

The primary objective of this study is to establish a relationship between the BOP, skull thickness and ICP. For this purpose, we selected a fluid-filled cylinder of two different thicknesses and experimentally subjected them to a defined blast wave (Friedlander wave form). In this model, the cylinder represents a circular skull while the fluid is the surrogate for the brain; all of them along with the blast wave are on a single plane, aligned in the direction of shock wave propagation. A coupled Eulerian-Lagrangian finite element method is used to model the fluid and the structure, and simulates the experimental conditions. The experimental results are compared not only to validate the model, but also to understand the flow physics as well as the structural shock dynamics. Once validated, the numerical method is used to understand the effect of different BOPs (under 1000 kPa), skull thicknesses (1 mm to 8 mm) and skull deflections on ICP (fluid pressure).

4.2 EXPERIMENT AND NUMERICAL MODEL

Figure 4.1 shows the experimental configuration of the fluid-filled cylinder and the blast tube used in the study. The details about the shock tube are discussed in detail in the previous chapter. Hence, the experimental description is reduced for brevity. To study

thickness effects, cylinders of two different thicknesses (2 mm and 3.5 mm) made of polycarbonate filled with mineral oil are used.

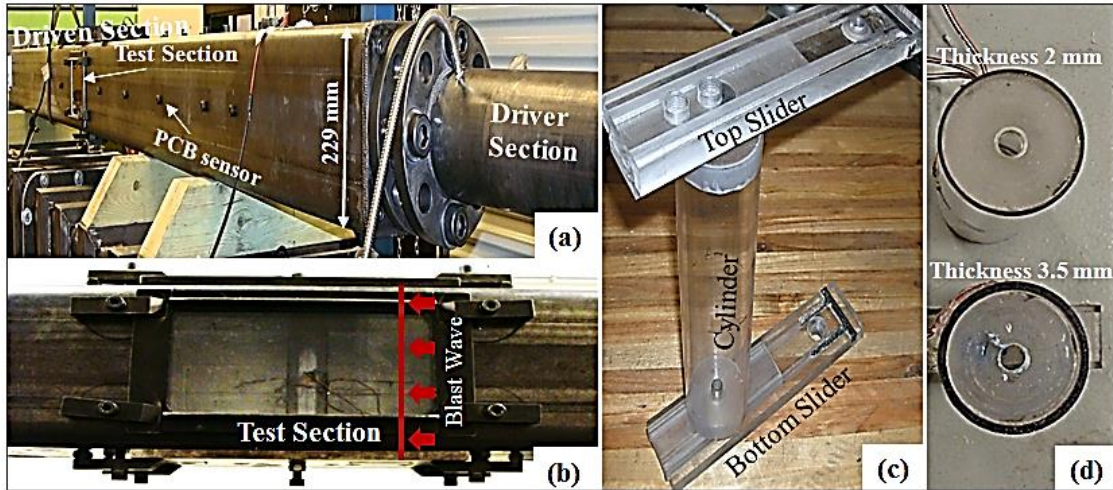


Figure 4.1 (a) Shock tube used in the experiments; (b) Fluid-filled cylinder inside the test section; (c) Cylinder with top and bottom sliders; (d) 2 mm and 3.5 mm cylinders used in the experiment

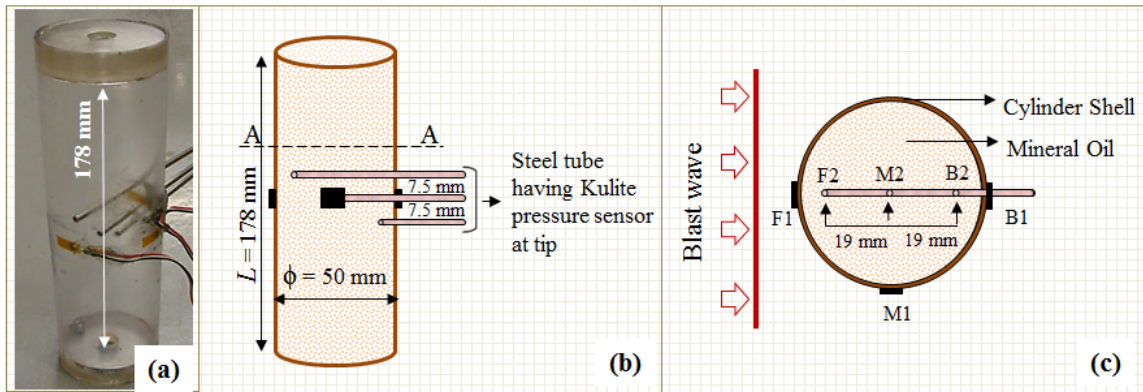


Figure 4.2 (a) Experimental cylinder set up without fluid showing the surface mount pressure/strain gages on the cylinder and pressure probe flushed with steel tube tip (b) Schematics of the experimental cylindrical set-up (c) Sectional view A-A showing all the sensor locations.

The sensors and its configuration used in this study are similar to the previous study. Please refer to Chapter 3 for the description. A schematic figure of the sensor configuration is shown in Fig 4.2 for reference. Detail description of the experiments,

sensors and the corresponding setup are also available in Nick Kleinschmit's thesis [61]. The planar blast wave interacting with the polycarbonate-mineral oil systems are numerically modeled using a coupled Eulerian-Lagrangian (CEL) finite element (FE) method. The details of the development are discussed in detail in the previous chapter and hence not provided in this chapter.

4.3 RESULTS AND DISCUSSION

4.3.1 Reflected overpressure (ROP)

The surface mounted pressure sensor on the cylindrical surface measures the local blast pressures as a function of time. When the air blast wave encounters a solid surface normal to its direction of flow, it gets reflected back leading to a high reflection ratio. The blast reflected overpressure at the frontal location (F1) shows a very sharp rise followed by a decaying pressure pattern (Fig. 4.3 (b)). The reflected overpressures at side (M1) and rear (B1) are significantly lower than the reflected overpressure at front (F1). Secondary peaks observed in the profiles at F1 as shown in Fig 4.3 (b) can be ascribed to the side wall reflections from the blast tube. Figure 4.3 (c) shows that there is a negative surface pressure of about -0.04 MPa; Figure 4.3 (d) shows an oscillating pressure pulse compared to the front sensor. Negative pressure observed at M1 is due to flow separation phenomenon. Since blast wave is travelling with high velocity, flow separation occurs symmetrically beyond the mid-point, due to the geometry of the cylinder.

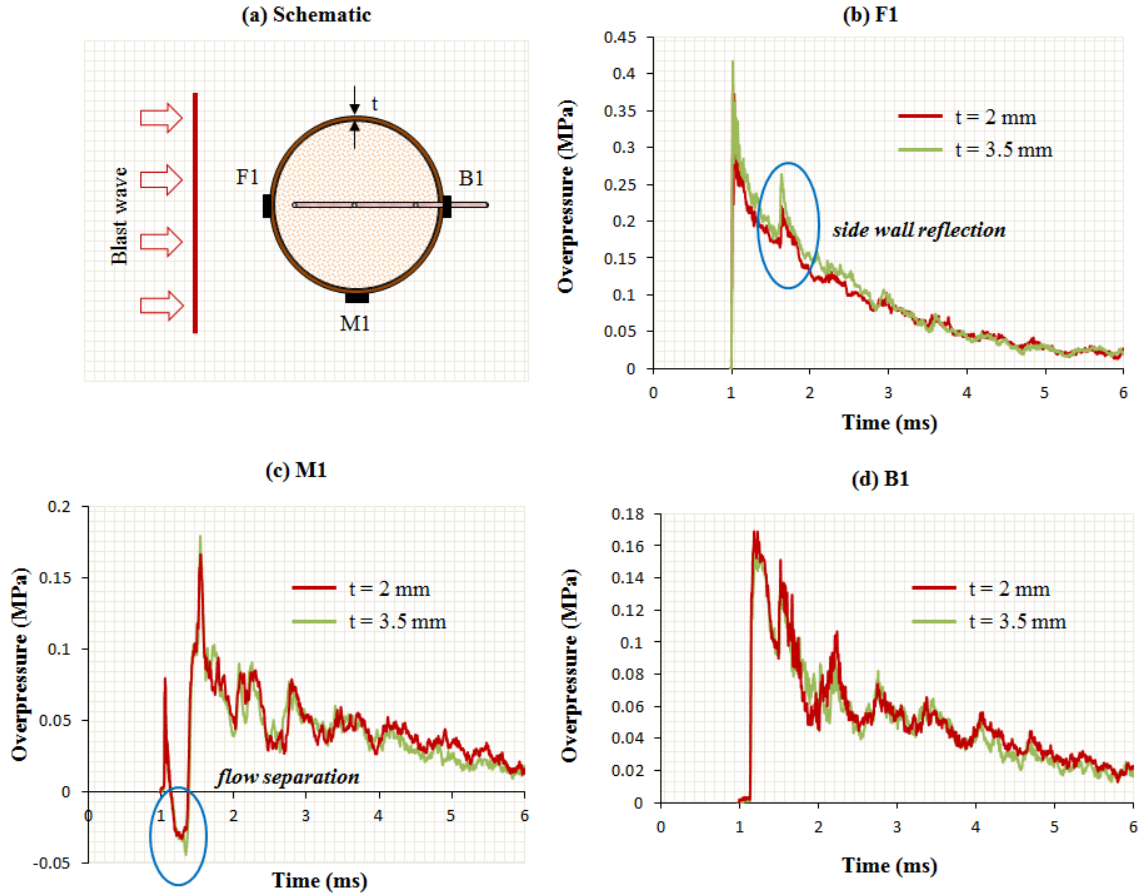


Figure 4.3 Experimentally measured reflected overpressure at three locations: (a) Schematic (b) front (c) middle (d) back

Figure 4.4 shows the experimentally measured surface pressure in the front, middle (side) and back of the 2 mm thick cylinder along with numerical simulation results. Figure 4.4 (b) shows the reflected overpressure in the front (experimental and numerical) along with the incident (side-on) pressure for the first 2.5 ms. Reflected peak overpressure $p_R = 0.4$ MPa for an incident BOP of $p_i = 0.16$ MPa yields a reflection ratio of $\Lambda_{F1} = 2.5$. While the shock front produces the higher amplification, this ratio reduces to incident value $\Lambda = 1$, in the blast at 2.5 ms.

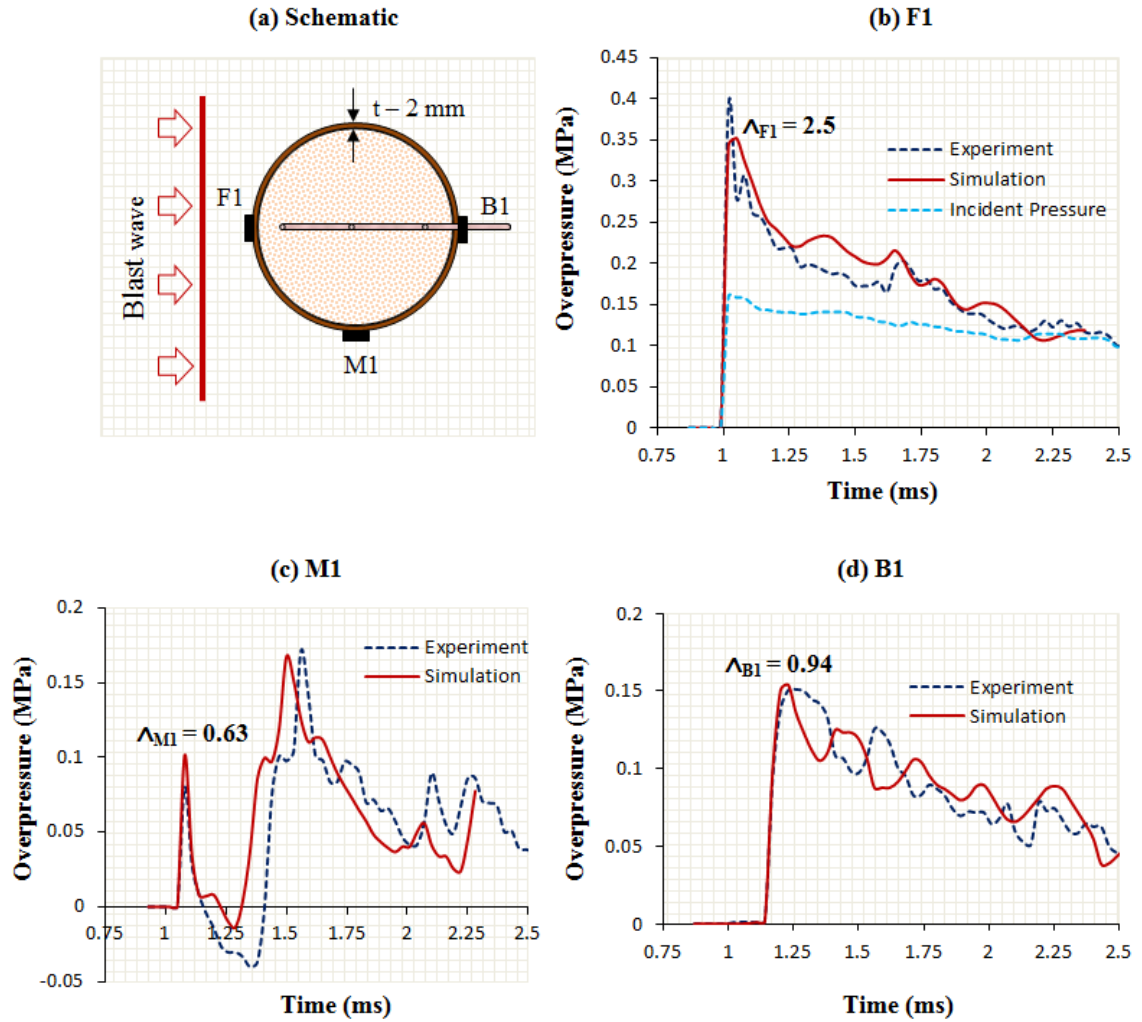


Figure 4.4 Comparison of experimental and numerical simulations of reflected overpressure at three locations: (a) Schematic (b) front (c) middle (d) back.

External flow dynamics influences the reflected overpressure on the cylinder surface depending upon the orientation of the surface normal with respect to the flow direction. When the normal points upstream and is parallel to the flow direction, then Δ is maximum; in the middle (M1), the normal is perpendicular to the flow direction and $\Delta_{M1} = 0.63$ (Fig 4.4(c)); in the back (B1) the normal points downstream and $\Delta_{B1} = 0.94$ (Fig 4.4 (d)). Figure 4.4 clearly shows that the maximum surface pressure is seen in the front; and

pressure fluctuations are seen in the middle and back due to fluid-structure interaction dynamics. The results of the numerical simulations agree qualitatively with the experimental results in essentially capturing the features and the general trends in the profile.

4.3.2 Intracranial Pressure (ICP)

Though the reflected blast overpressure for 2 mm and 3.5 mm cylindrical systems are identical, ICP varies significantly for 2 mm and 3.5 mm cylindrical systems. Comparisons of ICP computed at various locations for both the cylindrical systems are shown in Fig 4.5; the top and bottom row shows the ICP comparison of experiment and simulation for 2 mm and 3.5 mm respectively. Simulation results have similar patterns and oscillations as observed in experiments. For clarity, these pressure profiles are filtered at 15 kHz. At location F2, the sharp pressure rise is consistent with the shock front rise time in both 2 mm and 3.5 mm systems. While the peak reflected blast overpressure (p_R) is 0.4 MPa, the peak ICP is about 0.35 MPa and 0.25 MPa in 2 mm and 3.5 mm system respectively. This peak pressure variation between 2 mm and 3.5 mm systems is primarily due to the effect of shell thickness. In both 2 mm and 3.5 mm systems, the intensity of pressure reduces as it propagates from the front to the rear of fluid which can be noticed from the initial peak intensity of pressure at F2, M2 and B2.

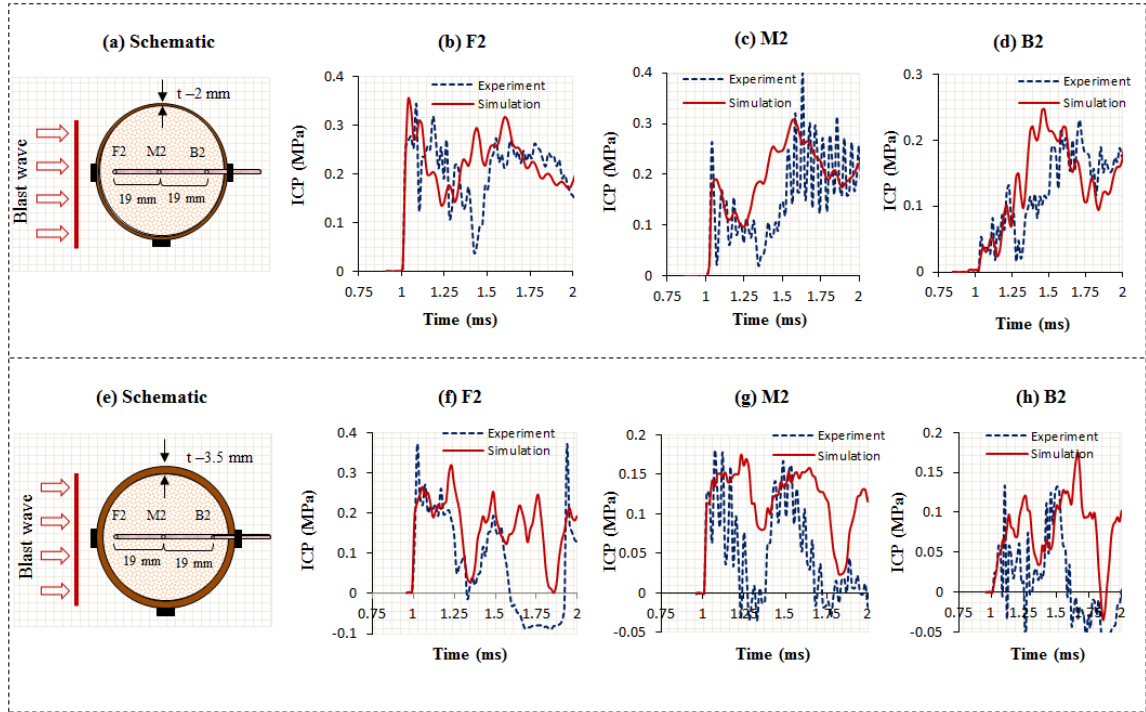


Figure 4.5 Comparison of experimental and numerical simulation of ICP: Top row-2 mm polycarbonate cylinder; Bottom row-3.5 mm polycarbonate cylinder.

Among the three locations, geometric center (M2) of both 2 mm and 3.5 mm systems show significantly higher pressure oscillations. The period of oscillation correspond to the to and fro travel time of an acoustic stress wave across the interior of the cylinder (23 mm radial distance in $16 \mu\text{s}$). Loading impulse, the area under the first positive cycle in the pressure-time diagram is an indicator of the net impulsive load acting on the body. Pressure profiles in Fig 4.5 clearly show that 2 mm system has higher impulse compared to 3.5 mm cylinder case. From Fig 4.5 it is clear that the peak ICP and its profile observed in numerical simulation agree qualitatively with the experimental results for both 2 mm and 3.5 mm cylinder cases..

The sharp rise in the fluid pressure is consistent with the shock front rise time in both 2 mm and 3.5 mm systems. Though the ROP for 2 mm and 3.5 mm cylindrical

systems are identical, the fluid pressure varies significantly for 2 mm and 3.5 mm cylindrical systems. While the peak ROP (p_R) is 0.37 MPa, the peak pressure in the fluid is about 0.36 MPa and 0.31 MPa in 2 mm and 3.5 mm system respectively. This peak pressure variation between 2 mm and 3.5 mm systems is primarily due to the effect of shell thickness. The numerical results are in good agreement with the experimental results in terms of both the peak magnitude and the general trend of the fluid pressure profile.

4.3.3 Shell strain (ϵ_s)

Figure 4.6 shows the comparison between experimental and numerical strains at locations F1, M1 and B1. Top and bottom row of Fig 4.6 shows the strain experienced by 2 mm (thinner) and 3.5 mm (thicker) cylinder respectively during blast loading. Surface mounted strain gauges at F1, M1 and B1 show negative (compressive), positive (tensile) and negative (compressive) strains, respectively. The strain measures indicate that the front section undergoes compression while the middle section is under tension, i.e., the circular cylinder become elliptical (oval) with major axis passing through M1 and perpendicular to the blast flow and minor axis passing through F1 and B1. The intensity and duration of the strain however varies between the 2 mm and 3.5 mm cylinder systems. This difference is due to the stiffness of the cylindrical system which in turn depends on the thickness of the shell. 2 mm cylinder has lesser stiffness; intensity and duration of strain are 0.6% and 1.75 ms respectively. 3.5 mm cylinder has higher stiffness; intensity and duration of strain are 0.4% and 1.35 ms respectively. The frequency of shell strain is higher in 3.5 mm cylinder (thicker) than in the 2 mm cylinder (thinner). It is clear from Fig 4.6 that the strain intensity and the pattern obtained from the

simulation matches fairly well with experimental results for both the cylinders. From the above results, it is thus clear that the developed numerical model is valid in terms of material model, boundary conditions and fluid-structure interaction and hence can be used for further analyses.

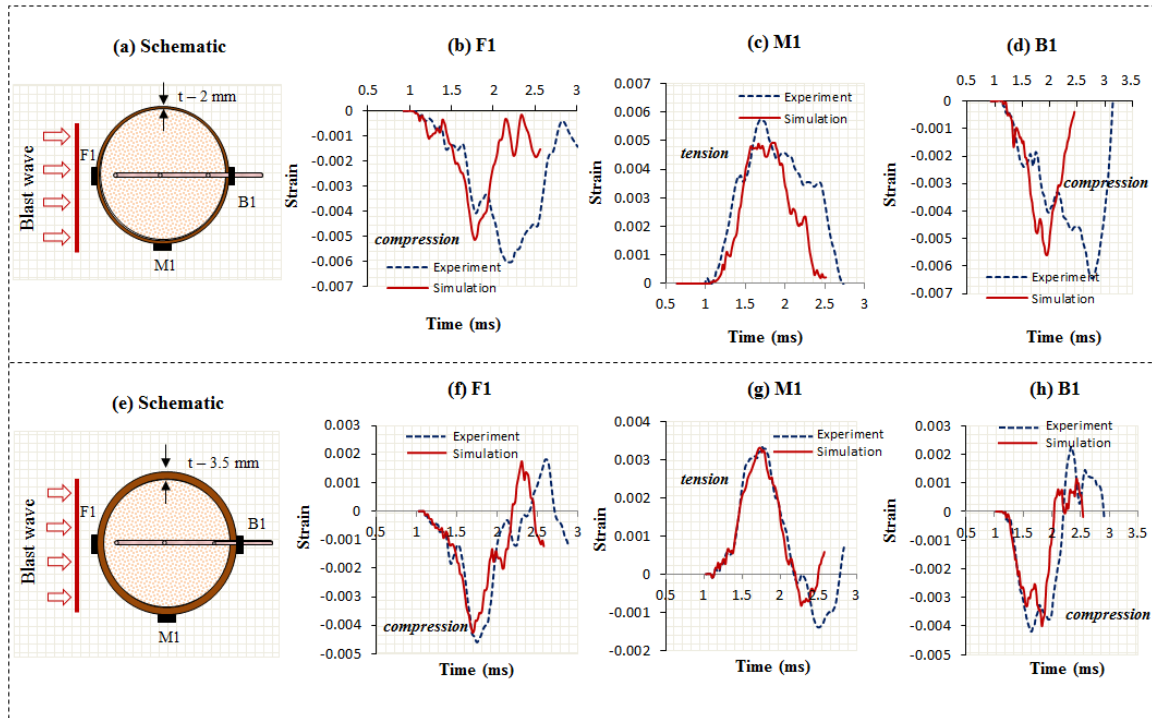


Figure 4.6 Comparison of experimental and numerical simulation of shell strain: Top row-2 mm polycarbonate cylinder; Bottom row-3.5 mm polycarbonate cylinder.

In summary, it is clear from the experimental and simulation results that the ICP drastically changes with respect to the shell thickness for an identical BOP. The intensity and shape of the ICP for the 2 mm and 3.5 mm shell thickness are distinct and the intensity of ICP reduces with increase in shell thickness. The blast loading intensity is the highest at the frontal (F1) regions of the shell, which subsequently results in the generation of higher ICP in the frontal (F2) region of the fluid. The strain experienced by the shell changes with respect to shell thickness and BOP. The 3.5 mm cylinder

experiences lesser deflection compared to 2 mm cylinder. However the frequency of strain is higher in 3.5 mm cylinder compared to 2 mm cylinder. With these analysis and results, the influences of shell thickness, BOP and shell deflection on ICP are studied and the relationships between these parameters are established and are discussed in the following sections.

4.4 RELATIONSHIP METHODOLOGY

In the numerical simulation, we used a linear elastic material model for the polycarbonate cylindrical shell. Many blast and blunt computational studies use linear elastic characteristics for the human skull. Hence the material model for the cylindrical shell is changed from polycarbonate to human skull to make the relationship more relevant for the study. To establish a relationship between skull thickness and ICP, thickness of the skull is varied in steps of 1 mm from 1 mm to 8 mm and each thickness model is subjected to the blast wave. For varying the thickness, outer radius of the skull is fixed and inner radius of the skull is altered; in such cases, the ROP (blast loading) remains the same for all thicknesses for a given incident BOP. To deduce the relation between the BOP and the ICP, the blast wave pressure is varied from 155 kPa to 625 kPa in five steps. These BOPs are the input to the numerical simulations. These input BOP are consistent with the lung injury criteria for human which makes the study relevant for bTBI [31, 32, 84].

Peak incident and ROP for each applied BOP are computed before and after the blast wave interacts with the cylindrical surface (F1). It is evident from the measurements that changes in the thickness of the skull within the range (1–8 mm) have negligible effect on ROP. Hence the blast loadings on the frontal (F1) region of the cylinder are

similar for all thickness models. Also the relation between incident and ROP is quite linear for the considered range of blast overpressures. The ICP generated for each ROP in each thickness model are computed near F2 and is given in Table 4.2. Analysis is carried out on this data set for deducing the relationship between the parameters.

Table 4.2 Pressure generated in the fluid for the given blast wave overpressure and shell thickness

Incident blast overpressure (kPa)	Reflected blast overpressure (kPa)	Shell Thickness (mm)								
		1	2	3	4	5	6	7	8	
150	326	373	326	305	259	248	230	202	171	Pressure generated near F2 (kPa)
250	629	676	571	550	480	442	385	350	335	
356	994	1072	1017	869	834	764	702	632	583	
474	1454	1562	1410	1378	1245	1072	996	963	881	
601	1989	2105	1897	1815	1751	1665	1568	1413	1306	

4.4.1 Relationship

The intensity of ICP generated directly depends on the intensity of blast load $F_{BW}(t)$. The blast load in turn depends on the ROP as given below

$$F_{BW}(t) = \int p_R(t) dA \quad (4.1)$$

where $p_R(t)$ is the ROP at time t acting on area dA of the skull. Though it is easier to measure incident BOP in the experiments, it is the ROP which actually induces the mechanical insult to head. Hence ROP is considered for the relationship. Figure 4.7 (a) shows the relation between skull thickness and ICP for each ROP. It is clear that there is a linear relationship between the skull thickness and ICP. ICP reduces linearly with

increases in skull thickness for a given ROP. Also the slope of the line (m_1 to m_5) increases with increases in the ROP. Figure 4.7 (b) shows the relation between ROP and its respective slope of the line obtained from Fig 4.7 (a). It is thus clear that there exist a linear relationship between the ROP and slope which indicates that ICP increases linearly with increase in ROP. The slope (M) of the line in Fig 4.7 (b) in turn gives the increase in the intensity of ICP generated with increase in the ROP for a given skull thicknesses.

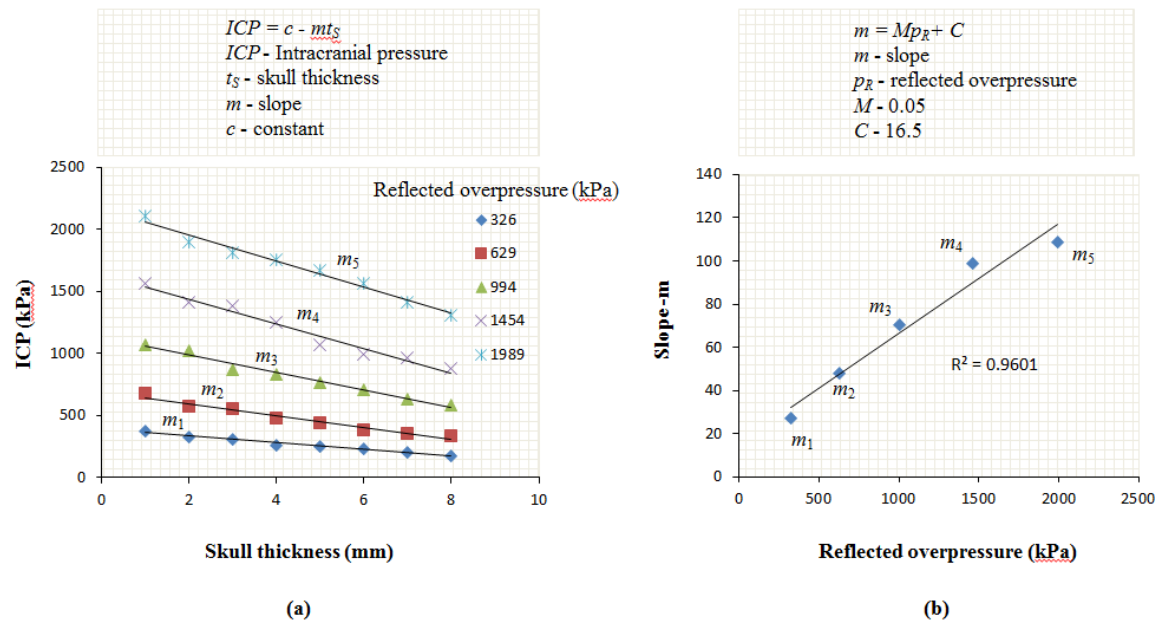


Figure 4.7 (a) Relation between skull thickness and ICP (b) Relation between reflected overpressure and its slopes

4.4.2 ICP equation

Since we established a linear relationship between ICP, skull thickness and ROP, an attempt is made to develop an equation involving these three parameters. The equation is intended to predict the ICP for a given skull thickness and ROP. The linear regression model is used to develop the equation. Since there are two independent variables in the study, multiple regression model is used. A multiple regression model deals with the variation of a dependent variable with respect to two or more independent variables. In

this case, ICP is the dependent variable that depends on the independent variables, skull thickness and ROP. Least square method is carried out for the analysis and the equation obtained from the analysis is given below,

$$p_b = c_1 p_R + c_2 t_s + c_3 \quad (4.2)$$

where p_b is the ICP in the brain, c_1 and c_2 are the coefficients of ROP (p_R) and skull thickness (t_s) respectively and c_3 is the ICP constant. The numerical values of the constants are given in the Table 4.3. Reflected overpressure in kilopascal (kPa) and skull thickness in meters (m) are the two inputs required for the equation to obtain the ICP in kilopascal (kPa). The applicability and limitation details of this developed equation are discussed below.

Table 4.3 Characteristics of the ICP equation

$p_b = c_1 p_R + c_2 t_s + c_3$		
Component	Value	Standard error
c_1	0.862	0.021
c_2	- 69940	5459
c_3	270	36
R^2	0.98	---
p_b	---	79 (kPa)

4.4.3 Valid range of ICP equation

Equation (2) clearly shows that increase in skull thickness reduces the intensity of ICP linearly; increase in ROP also increases the ICP linearly. Since the ICP induced is due to the direct transmission of blast wave (direct loading) near the interaction region, this linear relationship holds true for all test subjects. The relationship also gives a better understanding in comparing the bTBI results of different test subjects involving different

thicknesses and different ROP. Hence this equation can be used to establish a relationship between animals, humans (dead or alive) and even human surrogates.

4.4.4 Limitation of ICP equation

The intensity of pressure transmitted through heterogeneous mediums with many interfaces depends on the impedance mismatch of the participating mediums. Impedance mismatch occurs at the interface of two materials with varying acoustic impedances that are in turn determined by the elastic (or bulk) modulus and density. Hence if the impedance amongst different animal/human/dummy models are quite different then Equation (5) cannot be applied directly; however, the equation shows the general trend. Further the equation predicts the peak value in the brain just downstream of the blast interaction region. Hence the peak ICP values in this equation are strictly governed by the wave transmission near the interaction region rather than skull deformation. The size of the surrogate used in the study is comparable to a rodent head. Hence, the established relationship can be applied only to the rodent size head models. Also, since the equation has been developed by varying the skull thickness from 1 mm to 8 mm and incident blast wave from 150 kPa to 600 kPa, the equation is valid within these ranges. The equation may not provide valid ICPs when used outside these limits.

4.5 ROLE OF SKULL DEFLECTION ON ICP

It is clear from the foregoing discussions that the region just behind the first shock-skull interaction zone is affected by the shock wave transmission. For example, F2 will experience peak ICP in frontal blast interaction, and B2 in rearward blast interaction. The ICP at central region (M2) is, however found to be affected much more by skull deflection induced fluid compression. Referring back to Fig 4.6, the patterns and

numerical values of ICP at F2, M2, and B2 for both 2 mm and 3.5 mm are substantially different. It is thus of interest to study the variation of ICP as a function of a wider range of thicknesses, say 1mm to 8mm, typical of animals of interest and humans. The numerical results of the variations of ICP as a function of thicknesses are shown in Fig 4.8. Figure 4.8 (b) clearly shows that ICP at M2 is completely different for the 7 mm case compared to 2 mm case. ICP in the latter (2 mm) shows a distinctly increasing pressure trend (between 1.25 ms to 2.25 ms); no such trend is seen for the thicker cylinder (7 mm). Further, it is interesting to note that this pressure increase in the thin cylinder coincides with the surface strain. This matching of surface strain with the pressure indicates that indeed the pressure increase is due to shell deflection as measured by the strain gages.

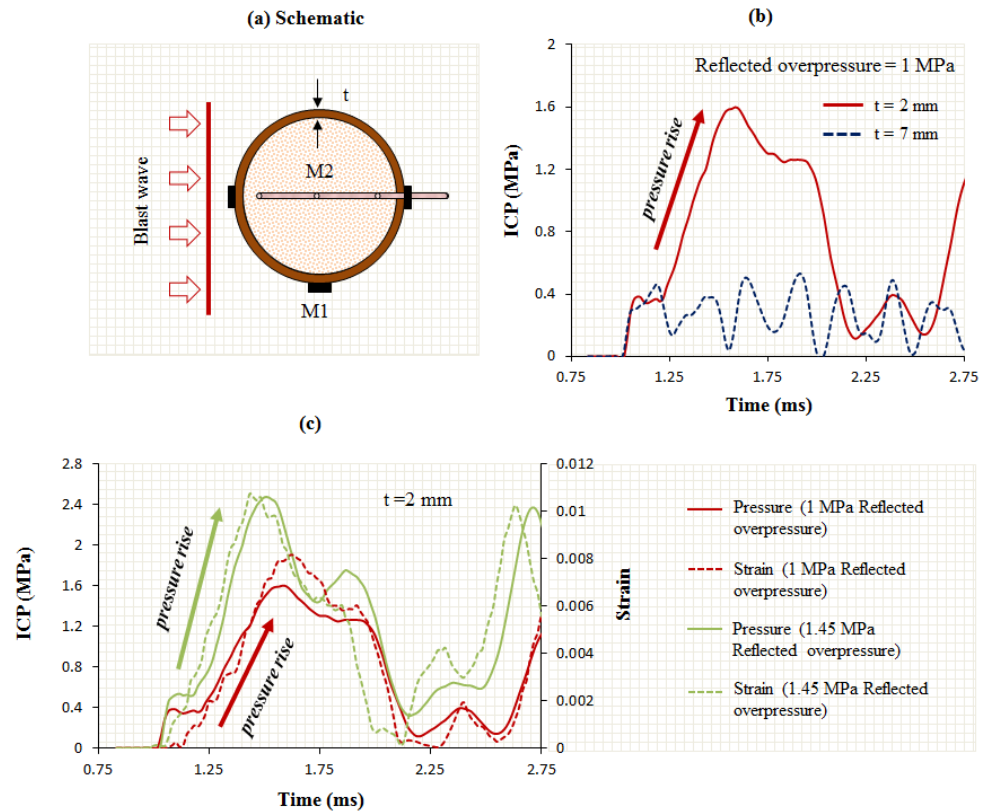


Figure 4.8 (a) Schematic (b) ICP comparison between 2mm and 7mm skull thicknesses (c) ICP correlation with skull strain for 2mm thick shell.

In order to further explore how this pressure rise (between 1.25 ms and 1.5 ms) is affected by the magnitude of ROP (or equivalently BOP), ICP at M2 (when ROP is 1000 to 1450 kPa) is plotted in Figure 4.8 (c). In both the cases, there is a strong correlation between the increase in the surface strain (at M1) and pressure rise in the fluid (at M2), once again indicating that the skull deflection is responsible for the ICP rise. The intensity of skull deflection can be given in terms of the ovality of the cylinder (deformed shape of the circular cylinder). From the analysis it is found that an ovality above 1% causes the pressure to rise (Moss et al., 2008, Bolander et al., 2011); lower values (<1%) do not result in any pressure rise in the fluid.

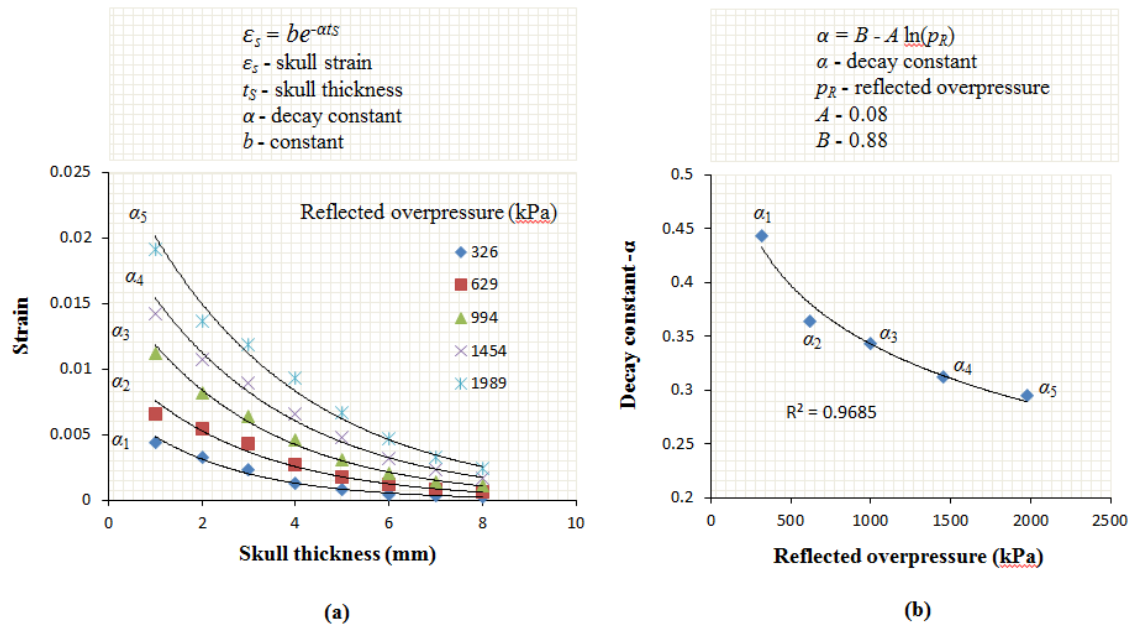


Figure 4.9 (a) Relation between skull thickness and skull strain (b) Relation between reflected overpressure and its decay constants

If the intensity of skull deflection were to affect the ICP, then the relationship between the blast load (ROP), thickness and strain level will give a better understanding on ICP. Figure 4.9 (a) shows the variation of strain levels experienced by the skull as a

function ROP. It is clear from the figure that for a given ROP, the strain decreases exponentially with increase in thickness. Thus the thinner sections deflect significantly higher enhancing the ICP (enhanced skull deflections-indirect loading). For any given thickness, the ICP increases with ROP; however, this increase is substantially higher for thinner sections due to the additive effect of skull deflection and transmission. Considering these effects, another equation can be established as given below

$$\varepsilon_s = be^{-\alpha t_s} \quad (4.3)$$

where ε_s is the skull strain; b is constant and $\alpha = B - A \ln(p_R)$ with $A=0.08$, $B=0.88$; p_R = ROP (300 to 2000 kPa).

Though we have not analyzed cylinders with non-uniform wall thicknesses, it is clear from the foregoing analysis that thinner section will deflect more for a given blast loading compared to thicker portions. For example, while frontal and occipital regions of human skull are thicker, the parietal region is thinner [85, 86], a blast facing the parietal region can induces high deflection and consequently produces higher ICP. Further, these analyses indicate that rodents may experience higher levels of deflection-induced ICP compared to humans or swine (see skull thickness details in Table 1) for a given range ROP.

Equation (3) is specifically developed for cylindrical specimens and should be used with caution. Though the exponentially increasing trend is seen for uniform thick cylinders, complex 3D geometry with varying thickness (typical of human head) may not strictly follow this relationship. Also, for a given ROP the intensity and mode of skull deflection between test subjects varies with respect to the skull geometry and stiffness.

4.6 CONCLUSIONS

In this work, we relate the ICP profile to the external blast overpressure and the thickness of a circular cylinder. The fluid-filled circular cylinders, analogous to a rodent head are used to deduce the relationship. With the help of experimental and numerical studies, it is found that

- The amplification factor Λ (ratio of reflected overpressure to incident blast overpressure) is maximal at the frontal blast interaction region and is quite insensitive to changes in thickness of the shell from 1 mm to 8 mm.
- Pressure history in the fluid varies greatly between thin and thick shell cylinder for an identical blast loading condition.
- ICP reduces linearly with increase in skull thickness and increases linearly with increase in reflected blast overpressure.
- An equation predicting the ICP for a given skull thickness and reflected overpressure has been proposed.
- The shell deflection is significant in thin cylinders compared to thick cylinders. The deflection (indirect loading) induces a rising pressure response in the fluid that is absent in thick cylinders; strong correlation is observed between ICP and shell strain profiles.
- Skull deflection increases exponentially as thickness is reduced for a given reflected overpressure; also, the skull deflection increases with increase in reflected overpressure.

- The ICP is affected by the direct transmission of shock wave as well as indirect fluid compression due to skull deflection. In thicker sections (where deflection is not significant), the ICP is influenced by the direct load at the site of initial blast interaction; in thinner sections the ICP is influenced by deflection dominated fluid compression.
- The limitations of the relationships established in the chapter are detailed in the discussions and one should be careful in applying them to generic geometric and loading conditions.

CHAPTER 5: THE BEHAVIOR OF HOMOGENEOUS VS. FLUID FILLED SOLID HEADFORMS UNDER BLUNT IMPACT LOADING CONDITIONS

5.1 INTRODUCTION

In the chapter 3 and 4, the mechanics of blast loading on the intracranial content has been studied. The findings from the studies assist in the development of bTBI mitigation techniques. In this and in the following chapter, blunt related intracranial loading mechanics are studied. The head injuries resulting from blunt impact depend on the type of loading condition and whether the head is protected or not. The commonly occurring injuries due to blunt impacts include skull fractures, contusion, sub-dural hematoma and diffusion axonal injury [87]. In non-helmeted head cases (e.g. soccer and boxing) as the head is unprotected the injuries are oftentimes lethal [88-90]. In helmeted head cases, though the loading is reduced by the helmet, the risk of injuries is still high. For instance, concussion in American football players is still high though the players wear helmet [91, 92]. The severity and the mode of head injury depend on the spatiotemporal variations of stress field (intracranial pressure, shear stress and shear strain) within the head (skull brain complex) that in turn are determined by the linear and rotational acceleration of the head. For instance, HIC predicts the probability of skull fracture based on the acceleration pulse at the C.G. of a given mass of the head (m) when the head subjected to a known impact velocity [93].

The testing methodologies of personal protective equipment (PPE) (e.g. Helmets) and assessment of the probability of injury in vehicle crashes are based on a single

measurement of linear acceleration of a specified headform. The prediction of brain injury from these measures intended to predict skull (or head) fracture is not straightforward and remains mostly heuristic in nature. The acceptable magnitude of the peak acceleration for skull fracture was simply reduced to lower limits to represent brain injury thresholds [94]. Whether this approach is scientifically valid is still an open question. Additionally, the Hybrid III and other standard headforms are rigid compared to the highly heterogeneous human head-brain system [19]. Thus, comparing a homogenous rigid headform to a heterogeneous compliant human head under identical loading conditions will help to identify the differences between the two. A study carried out by Saczalski et al with the compliant head model showed that acceleration at the center of gravity of unprotected human like compliant headform is lesser than the unprotected rigid headform. Hence, at first it appears that using a rigid headform for modeling head injury is conservative in terms of severity of head injury [95]. However, the same study showed that the structural response of compliant headform is completely different from the rigid headform; the former is more biofidelic than the latter, and should be taken into consideration in assessing brain injury.

Apart from linear acceleration, parameters like rotational acceleration, pressure and strain should be considered in the study of head/brain injuries [11-14]. For instance, concussion studies were carried in the actual football games with the head impact telemetry (HIT) system [96]. The rotational and linear accelerations measured with HIT are then related to the concussions experienced by the players [96-98]. However, the results could not find a direct correlation between the measured values and observed concussions on the field [99]. In another study, yet another criterion based on the

intracranial pressure of 35 psi for serious head injuries was established [100]. Other studies have suggested strain and strain rate measures as the criteria for the head/brain injury [12]. A head injury criterion based on rotational acceleration was also developed from the studies conducted in the football studies [98, 101, 102]. In summary, there is no consensus on which mechanical measures determine injuries, or their values. This is further exacerbated by the fact that the rigid head form is capable of producing only a single value of acceleration or strain. Hence, a study to identify the difference between rigid and compliant head forms is needed.

The primary objective of this study is to identify the critical differences between the compliant and rigid head surrogate under identical blunt loading conditions, and examine the effect of target surfaces. Carefully planned experiments and computational modeling of the experiments are carried out in this work.

5.2 METHODS

5.2.1 Experiment

Two different drop towers are used in the experiments involving compliant acrylic-gel and rigid head form as shown in Figure 5.1. Figure 5.1 (a) shows the details of the home-made precision-machined drop tower and the compliant headform. Some practical reasons of how the headforms have to be held and dropped necessitated the use of two towers, though the mechanics of the blunt impact is identical. The home-made tower is operated manually and the drop height is measured using a measuring tape rigidly attached to the wall. The drop velocity is computed from the drop height, travel time and equation of motion.

The compliant head surrogate is made of acrylic spherical shell filled with the ballistic gel as shown in Fig 5.1(c). The acrylic sphere is 150 mm in diameter and 2 mm thick. This size is comparable to the head size of 2 year old toddler with a skull thickness of 2 mm [103, 104]. Ballistic gel prepared by mixing 10% of gelatin powder by weight to 90% of water represents the brain tissue [105, 106]. The mass of the entire assembled unit of the acrylic gel complex is 1.96 kg;

The drop tower used for the rigid surrogate is shown in Fig 5.1 (e) to 5.1 (g). This drop tower is a monorail uniaxial tower manufactured by Cadex.Inc and is currently being used for the testing of army helmets. Since the details of the monorail tower are available in reference [107], only the working principles are presented here. The drop carriage in the monorail tower is connected to the surrogate through a hook as shown in Fig 5.1 (f). The drop carriage is raised automatically to a specific height and a switch for dropping the surrogate releases the hook. On releasing the hook, the surrogate drops on the anvil under the action of gravity.

The rigid head surrogate used in the study is made of aluminum. The rigid surrogate comprises of an impactor, ball arm, connector rings and the holder. The connector rings connect the impactor and ball arm as shown in Fig 5.1 (f). The ball arm in turn is connected to a holder that is hooked to the drop carriage. The total weight of the drop assembly of rigid surrogate is 1.96 kg which is equivalent to the drop mass of the compliant head surrogate. The radius of the compliant acrylic shell and the rigid impactor is same as shown in schematic Fig 5.1(d) and (h) respectively. It is thus ensured that the masses of both the compliant and rigid headforms are same as also the shape of the impacting surfaces.

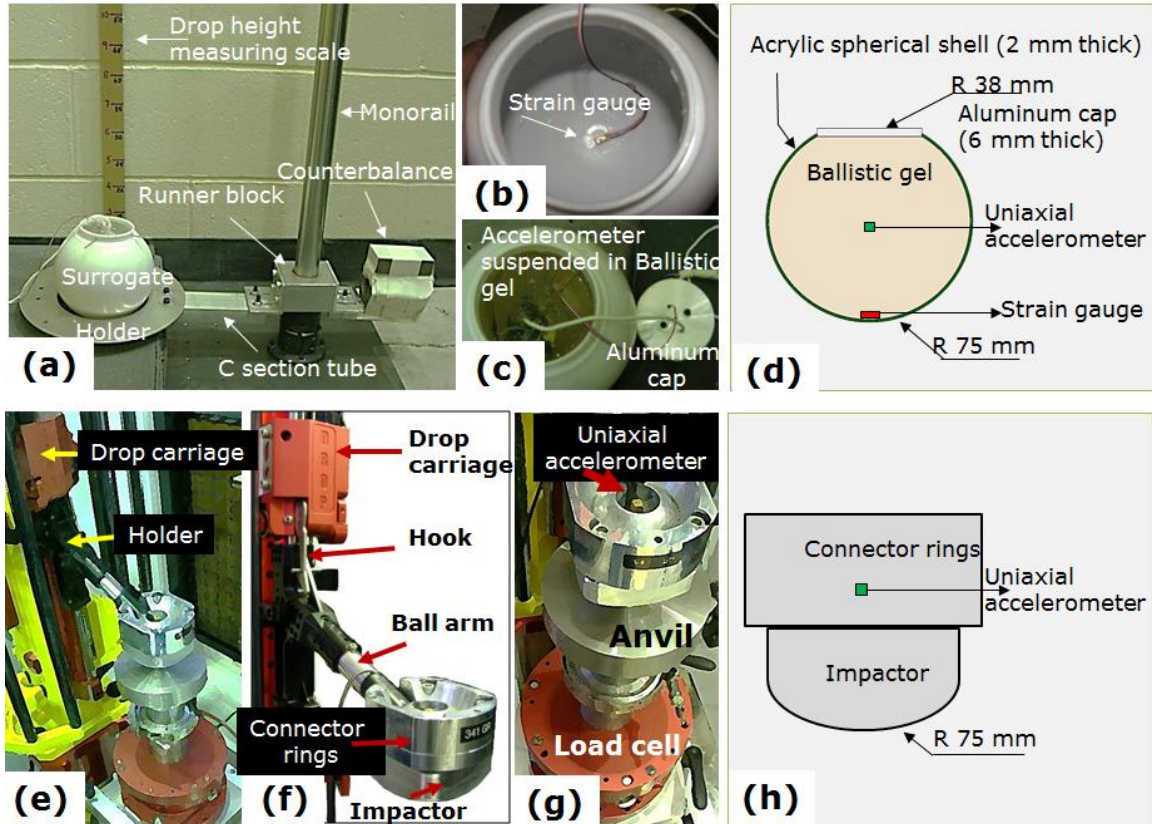


Figure 5.1 Top row – compliant surrogate experimental set up; Bottom row – rigid surrogate experimental setup: (a) In built drop tower setup ; (b) Strain gauge on inner bottom surface of the acrylic sphere; (c) Acrylic gel complex rigged with sensors; (d) Schematic of acrylic gel model; (e) Cadex monorail drop tower setup; (f) rigid aluminum surrogate setup; (g) Mounting of accelerometer and load cell; (h) schematic of rigid surrogate.

The compliant surrogate is instrumented with a linear accelerometer and a strain gauge. The linear accelerometer (piezoresistive) is suspended at the center of gravity of the gel, while the strain gauge is glued on the inside bottom surface of the sphere as shown in Fig 5.1 (b). The rigid surrogate is fitted with a linear accelerometer at the C.G. Further, a load cell is mounted at the bottom of the target as shown in Fig 5.1 (g). The linear accelerometer (piezoresistive) mounted at the center of ball arm and the load cell assembled to the anvil measure the temporal variation of the acceleration and impact force of the rigid surrogate.

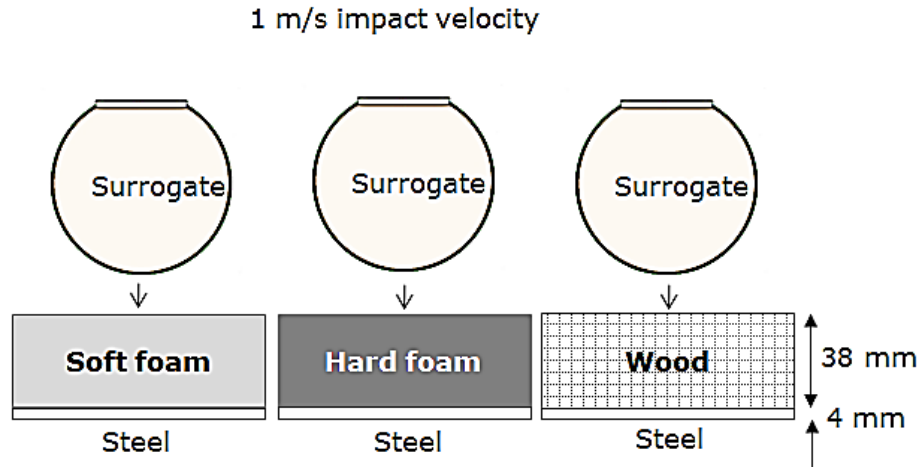


Figure 5.2 Target surface model.

Soft foam pads, hard foam pads and a wooden board (Fig 5.2) act as the target surfaces; the stiffness of these target surfaces increases from soft foam to hard foam to that of the wood. Foam pads used in the study are provided by the Team Wendy, a supplier of such pads to Advanced Combat Helmets (ACH) used by the US Army. Each experiment is repeated three times ($N=3$) for each surrogate, with a total of 36 experiments for the two headforms on the three different targets. The acceleration, strain and load cell data are recorded every 30 μs . The standard deviation of the peak values of acceleration, strain and load cell data between the experiments are within $\pm 5\%$.

5.2.2 Numerical model

The surrogates and its interaction with the different target surfaces are modeled using the commercial FEA software, Abaqus. The acrylic spherical shell in the compliant surrogate is modeled as a linear isotropic elastic solid with the material properties of acrylic (PMMA). The gel contained in the sphere is modeled with Mie-Gruneisen

equation of state, which is often employed in shock compressive materials. Material properties of acrylic sphere and gel are close to the material properties of the skull and brain respectively. In the rigid surrogate module, a solid spherical aluminum body that represents the assembled unit in the experiment is modeled as a linear isotropic elastic solid. The radius of the solid is same as the radius of the rigid impactor. The foam pads provided by the Team Wendy are made of polyurethane [108]. The low density foam material model is employed for the polyurethane foam pads. This material model uses a viscous-hyperelastic formulation. The model assumes the Poisson's ratio of the material to be zero. The Team Wendy provides the uniaxial compression test data required for this material model.

The components in both the surrogate model are discretized with Lagrangian 8-node linear brick, reduced integration, hourglass control element (C3D8R). Uniform mesh is employed in all components. Total number of elements and nodes in the entire compliant surrogate model are 169,918 and 226,396 respectively; the total number of elements and nodes in the rigid surrogate model are 98192 and 102649 respectively. Mesh convergence studies are performed for all FE models. The mesh convergence criterion of 0.4% change in the peak value of a given field variable (i.e. acceleration and strain) is employed in the simulations. The mesh convergence is achieved at the element size of 3mm for the gel, aluminum sphere and foam pads and 1mm for acrylic shell

The impact velocities employed in the experiment are applied to the numerical model of compliant and rigid surrogates. The surrogates impact the surface with a specified velocity. The penalty method with frictionless contact condition is used in the simulation to enforce the interaction between the different components of the finite

element model. The finite element interaction model is solved using nonlinear transient dynamic analysis where the governing partial differential equations of the conservation of momentum, mass and energy along with the material constitutive equations and the equations defining the initial and the boundary conditions are solved simultaneously. A typical simulation requires about 8 hours of CPU time on 8 dedicated Opteron parallel processors (processor speed 2.2 GHz, 2 GB memory per processor), for an integration time of 20 ms.

5.3 RESULTS AND DISCUSSION

5.3.1 Target surface

Stiffness of the target surface determine the intensity and duration of loading on the impacting body. For a stiffer target surface, the duration of contact is less but leads to higher forces on the impacting body compared to the softer target surface [109]. Hence, the wooden impact surface offers higher load on the gel and soft foam pad offers the least load on the gel as shown in Fig 5.3. Upon impact, the soft foam deforms with increased the contact time and decreased gel acceleration and shell strain. In both the compliant and rigid surrogates, 1) the magnitude of acceleration increases with an increase in the stiffness of the target surface 2) the duration and rise time of acceleration reduces with the increase in the stiffness of the target surface. The duration and rise time of acceleration is lesser for rigid surrogate compared to compliant surrogate.

The shell strain of the acrylic sphere is plotted along with the gel acceleration as shown in Fig 5.3 (a). The shell strain depends on the impact force that in turn depends on the stiffness of the target surface. Hence, the maximum shell strain is observed for wood, followed by hard foam and then the soft foam. In the case of wood, a short dimple is

observed in the shell strain profile. This represents the local shell bending, where the strain changes from compression to tension and tension to compression. When the tensile strain exceeds an ultimate strength, the material fails. This is one of the key mechanisms of skull fracture, where the skull bends inward at the impact location resulting in fractures on the inner surface [110]. For hard and soft foam, the intensity of shell deformation over the time is less. Hence, there is no change in the strain from compression to tension.

Table 5.1 Target surface model at 1 m/s impact velocity

Impact surface	Acceleration (G)		HIC	
	Compliant	Rigid	Compliant	Rigid
Soft foam	22	16	15	6
Hard foam	28	27	25	15
Wood	52	163	57	241

Table 5.2 Load cell measurements in target surface model

Impact surface	Impact force (N)
Soft foam	193
Hard foam	416
Wood	3321

In case of rigid surrogate, there is no shell deformation. Hence, the target surface deforms upon impact. For the hard and soft foam, the peak acceleration of the rigid surrogate is less than the compliant surrogate as given in Table 5.1; this increase in acceleration in the compliant surrogate is due to the acrylic shell. In compliant surrogate, the gel actually impacts the acrylic shell which has a higher stiffness compared to foam pads. Hence, the gel acceleration is higher than the rigid surrogate as given in Table 5.1.

The same reason is applicable for the variations in HIC. The similar kind of variation in acceleration and HIC between compliant and rigid head surrogate is given in the Saczalski et al study. Thus for the compliant surrogate, the acceleration of gel is based on the stiffness of both the target surface and acrylic shell. For rigid surrogate, the acceleration is entirely determined by the stiffness of the target surface.

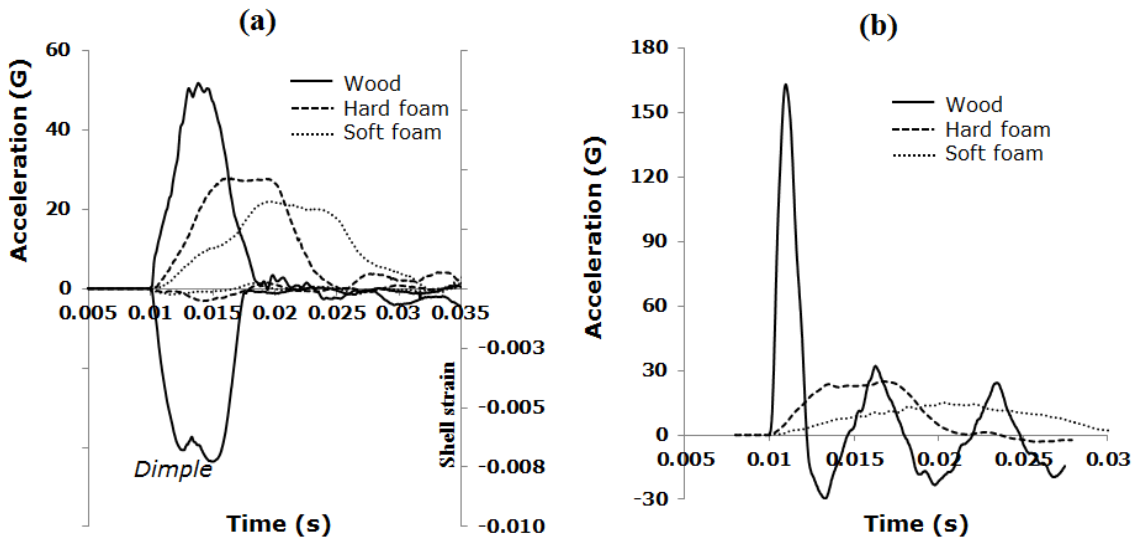


Figure 5.3 Target surface model – 1 m/s impact velocity (a) Compliant surrogate (b) Rigid surrogate

In case of wooden target surface, the difference in the acceleration between the compliant and rigid surrogate is significant. This could be understood from the work energy principle. When the body contacts the target surface, the kinetic energy of the body is transformed into internal energy of deformation due to the impact force. Thus, upon impact the acrylic gel complex deforms (higher shell strain) leading to less force and thus less acceleration. Since the wooden surface is fairly rigid, the mass (1.96 kg) times the acceleration (1630 m/s^2) of the rigid surrogate is quite equivalent to the impact force (3321 N) measured as given in Table 5.2. With this understanding, it is evident that in the perspective of acceleration injury criterion, a rigid surrogate incurs a severe level

of injury than the compliant surrogate. Nevertheless, in the perspective of stain injury criterion, a compliant surrogate incurs a severe level of injury than the rigid surrogate. Thus, a single parameter like acceleration or strain alone will not provide adequate details for understanding the head injury. Hence, a single injury criterion alone will not state the severity of the head injury. Only a combination of injury parameters (acceleration, strain and intracranial pressure) can give actual details on the severity of the head injury, which could be possible only with an actual head or with a compliant head surrogate.

5.3.2 Numerical model validation

The developed numerical models are validated against all the experimental blunt impact loading conditions. Only the results concerning the compliant surrogate impacting the wooden target surface are presented for brevity. The peak, decay pattern and duration of the acceleration in the numerical simulation are quite similar to that of the experiment for the compliant surrogate as shown in Fig 5.4. The shell strain in the simulation follows the same pattern as that of the experiment. Key features like a short dimple in the shell strain (Fig 5.4) in the experiment are captured in the simulation. Hence, it can be concluded that the numerical model of the complaint surrogate behaves in a similar way to that of the ones used in the experiments. With this validated model the variation of the acceleration across the surrogate for different target surfaces are studied.

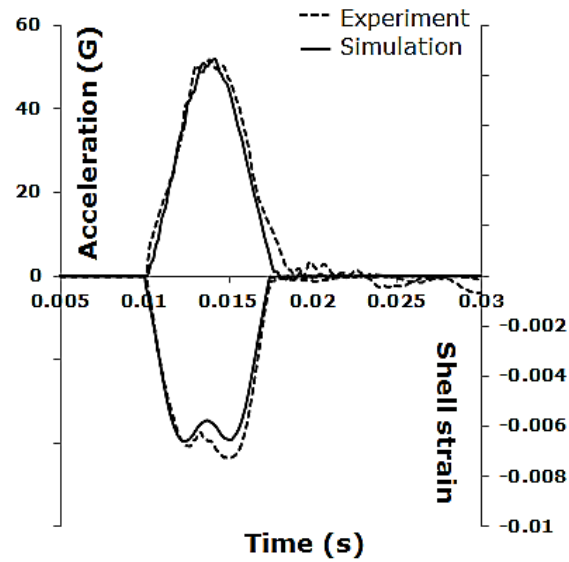


Figure 5.4 Comparison of experimental and numerical results of compliant surrogate impacting the wooden target surface

5.3.3 Gel acceleration

When a compliant body impacts a rigid surface, it undergoes deformation that leads to different acceleration at each point in the surrogate; whereas the acceleration at each point in the rigid surrogate is same. The schematic of the points of interest in the surrogate considered in the study of acceleration is shown in Fig 5.5 (a). The validated numerical model of complaint surrogate impacting the wooden surface at 1 m/s is considered in the analysis. At the beginning of compression phase, i.e, when the acrylic gel complex impacts the surface, the shell and gel near the impact location (B) begins to deform instantaneously. This results in the sharp rise in acceleration as shown in Fig 5.5 (b). The remaining part of the surrogate continues to move slowly towards the surface. Hence, the acceleration is quite smooth and uniform at other locations of the surrogate. It should be noted that the peak acceleration at the impact location exceeds the acceleration

at C.G of the gel. At the end of restitution phase, when the surrogate separates from the target surface, the gel impacts the shell due to the differences in the rate of restitution. This accounts for the sharp peak at the end of restitution phase. Hence, it is evident that the acceleration at the coup end is more critical than at the center of the compliant surrogate. In rigid surrogate there is no deformation and hence there is no relative motion between different points in the body. Thus, the acceleration is similar at all points in the body as shown in Fig 5.5 (c). Thus, the rigid and complaint surrogate behaves entirely different under similar loading conditions.

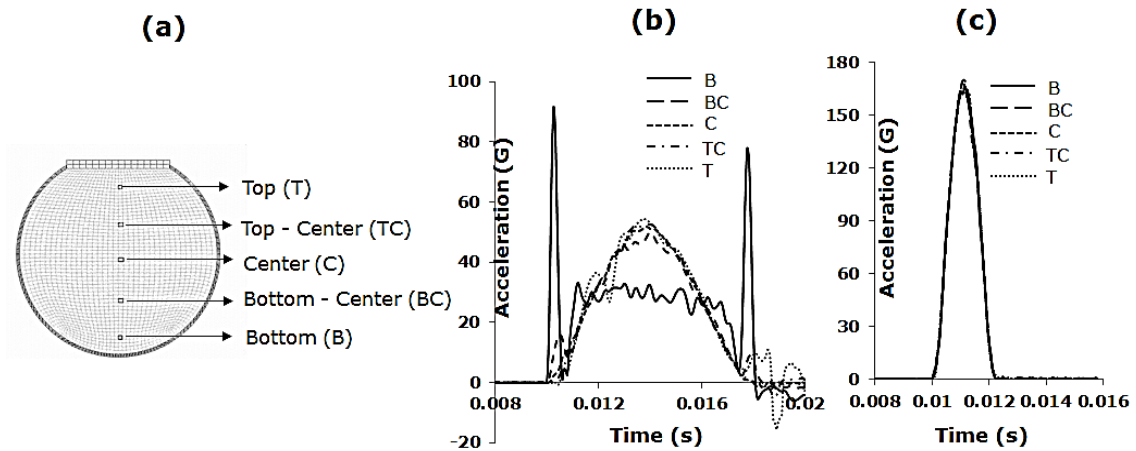


Figure 5.5 Target surface model – 1 m/s impact velocity (a) Measurement locations (b) Compliant surrogate (c) Rigid surrogate

To study the details of the sharp acceleration at the beginning of the compression phase, three cases are considered; wood, hard foam and soft foam target surface at 1 m/s impact velocity. The acceleration measured at bottom (B) of the gel for the wood, hard and soft foam case is shown in Fig 5.6. The intensity of sharp rise in acceleration reduces with a decrease in the stiffness of the target surface. The relative motion between the gel and shell increases with increase in stiffness of target surface which leads to the sharp

increase in the acceleration of the gel. In addition, the acceleration begins to plateau with an increase in the stiffness of the target surface. This is due to the deformation pattern of the shell gel complex. The deformed shape of the surrogate is shown in Fig 5.6 for all the three cases. For wood, the bottom part of the surrogate flattens that subsequently resulted in the plateaued acceleration. This plateaued deformation reduces with hard foam and it further reduces with soft foam. Thus, the plateau in the acceleration reduces with a decrease in the stiffness of the target surface.

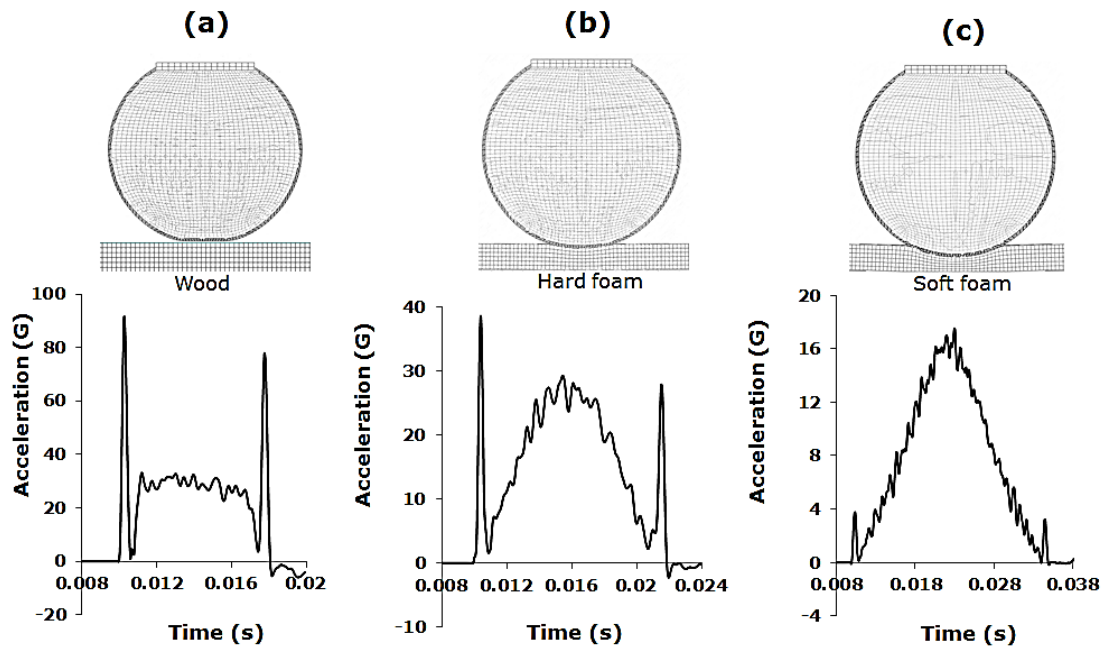


Figure 5.6 Gel acceleration near the impact location (B) at 1 m/s impact velocity (a) Wooden surface (b) Hard foam surface (c) Soft foam surface

The HIC of complaint surrogate is higher than the rigid surrogate in hard and soft foam cases (see Table 5.1). For wooden case, the rigid surrogate has higher HIC. Saczalski et al. observed similar kind of variation in HIC and acceleration between compliant and rigid head surrogate with respect to the target surface. Hence, for high stiff

target surface material, rigid surrogate incurs higher HIC and for soft target surface material compliant surrogate incurs higher HIC.

Hence, using a compliant surrogate for soft target surface cases is worse than using rigid surrogate and will incur more severe level of head injuries. Moreover, in compliant surrogate, key features in the acceleration like sharp initial rise and plateaus are captured that depicts the typical loading mechanics. Though it is not certain that the variations in acceleration profile (oscillations, the shape of the pulse, rate of loading and duration) are related to pathological changes in the brain, it is essential to duplicate the actual response characteristics of the human head to understand the injury and arriving at the injury threshold. Rigid head surrogate did not provide enough details on the mechanics of blunt loading. Thus to understand the actual mechanics of loading on the human head under different blunt impact conditions, a compliant head surrogate is needed. In addition, acceleration at the coup end is more critical than at the center of the compliant surrogate. The current testing methodology of PPE and the injury criteria like HIC, severity index and linear acceleration need to be reviewed in the perspective of actual loading mechanics rather than the single point acceleration from the rigid headform.

5.3.4 Limitations of the current study

The experiments and simulations used an impact velocity of 1 m/s; however, the mechanics may be different at higher velocities and should be studied. The compliant surrogate used in the study is comparable to toddler head; the effect of size, shape and shell thickness may alter the results and should be analyzed. Apart from accelerations,

intracranial pressure is an important variable and should be studied to prelude the impact to both head and brain injuries.

5.4 CONCLUSIONS

In this chapter, we have compared the behavior of rigid and compliant head forms when they impact wood, soft and hard foams at a velocity of 1 m/s. The followings are our observations.

- The magnitude of the acceleration of the surrogate increases with increase in the stiffness of the target surface; rise time and duration of the acceleration reduces with increase in stiffness of the target surface;
- Upon impacting a rigid target surface, the acrylic shell bends inward resulting in tensile fractures;
- While the acceleration field in the rigid head form is uniform, the field varies from coup to counter-coup region in the gel-filled case;
- The variation in the acceleration field (coup to counter coup end) in compliant surrogate is influenced by the shell deformation that in turn depends on the stiffness of the target surface; coup acceleration exceeds the acceleration at the center of gravity of gel for stiffer target surface models.
- Acceleration and HIC in compliant surrogate is higher than the rigid surrogate in cases of less stiff target surfaces.

Based on these observations, it can be concluded that compliant headform captures the mechanics of head-brain impact better. However, in certain cases the rigid head form provides a conservative upper bound when acceleration is used as the criterion.

When strain is the injury criterion, then the rigid head form may under predict the probability of injury.

CHAPTER 6: DESIGN OF FOAM PADS FOR MITIGATING THE IMPACT INDUCED HEAD INJURY

6.1 INTRODUCTION

In the previous chapter, we studied the effect of target surfaces on the behavior of the surrogate. Since target surfaces alters the mechanics of loading, these need to be studied. The motivation behind this study is that in the Operation Enduring Freedom in Afghanistan (OEF) and in the Operation Iraqi Freedom (OIF), about two thirds of the soldiers encountered with traumatic brain injury (TBI) were wearing helmets during the time of injury [111]. The role of foam pads in mitigating injury for a given load needs to be studied. There is a need for better energy absorbing pads to mitigate the head injuries. Existing foam pads inside the helmet is 0.75” thick bilayer foam pad (50% soft and 50% hard foam pad connected in series). Moss et al. employed the football helmet pads in the army head helmet subspace and compared their energy absorption characteristics with bilayer pads; none of the football helmet pads performed better than the bilayer pads [112]. Thus, presently the bilayer foam pads suits better for the current army head helmet subspace.

The army advanced combat helmet (ACH) with the bilayer foam pads meets the standard helmet testing criteria at 10.1 fps impact velocity. However due to the demands of the current battle scenario, the Army raised the impact velocity to 14.14 fps and 17.3 fps [20, 21]. Moss et al. studied the energy absorbing characteristics of the bilayer foam pad (0.75” thick) at various impact velocities. It is evident from the findings that due to limited head helmet subspace, the foam pad bottoms out at high impact velocities, for

instance higher than 14 fps. Hence, increasing the thickness of the pad which is nothing but increasing the head helmet subspace will result in the absorption of more energy [112]. However increasing the head helmet subspace will increase the weight of the helmet which causes awkward and detrimental effects to the wearer [113]. A large helmet decreases the ballistic performance and hence not recommended. Thus, selecting the right energy absorbing characteristic of foam pad for a given head helmet space for different blunt loading conditions is essential to mitigate head injury.

The primary objective of this study is to understand the energy absorbing characteristics of the foam pads for the given head helmet subspace at different impact loading conditions. Six different configurations of the foam pad are made with the hard and soft foams. These configurations are designed based on the linear springs connected in parallel and series, which are discussed in section 6.2.1. The pads are then experimentally subjected to an impact load of 4.9 kg at low (1 m/s), medium (3 m/s) and high (5 m/s) impact velocities. A uniaxial drop tower is used for performing the impact experiments. The details of the experimental setup are discussed in section 6.2.2. The experimental results are discussed in the section 6.3 followed by the corresponding discussion in section 6.4. Finally, conclusions (section 6.5) are made on the energy absorbing characteristics of the designed foam pads.

6.2 METHODS

6.2.1 Theoretical model

Consider a typical force deflection curve of a foam material as shown in Fig 6.1 (a). The foam pad deflects linearly with the applied force till it reaches the end point of elasticity. Then the deflection plateaus with the constant force. After the point of

bottoming out, the force rises instantaneously. In other words, once the foam bottoms out, it can no longer bear the load; instead it transfers the force. Hence, the absorption of energy occurs till the foam reaches the point of bottoming out; the amount of energy absorbed is given by the area under the curve as shown in Fig 6.1 (a). The maximum deflection of the foam corresponding to the point of bottoming out is x_m . It should be noted that the force at the point of bottoming out will be quite equivalent to the force at the end point of elasticity; end point of elasticity is where the linear force deflection relationship ceases.

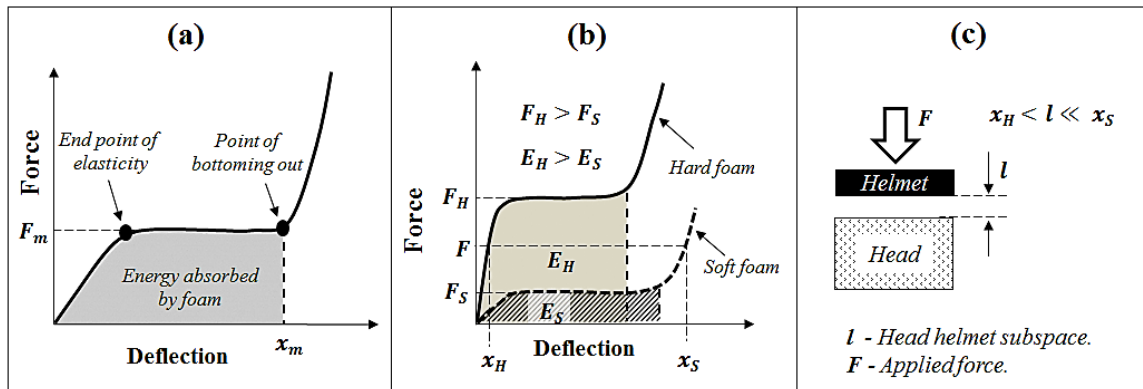


Figure 6.1 (a) Force deflection curve of a typical foam pad; (b) force deflection curve of hard and soft foam; (c) schematic of the head helmet model for foam selection

The schematic of the force deflection characteristics of hard and soft foam is shown in Fig 6.1 (b). Hard foam absorbs more energy compared to soft foam. Similarly, the bearable force of the hard foam is higher than the soft foam. With these considerations, for a given space between the head and helmet and for the given loading conditions, a soft or hard foam pad needs to be selected for the helmet padding. For instance, for the head helmet subspace of l ($x_H < l \ll x_S$) and for the applied force of F

as shown in Fig 6.1 (c), hard foam is the right selection of padding compared to the soft foam as shown in Fig 6.1 (b).

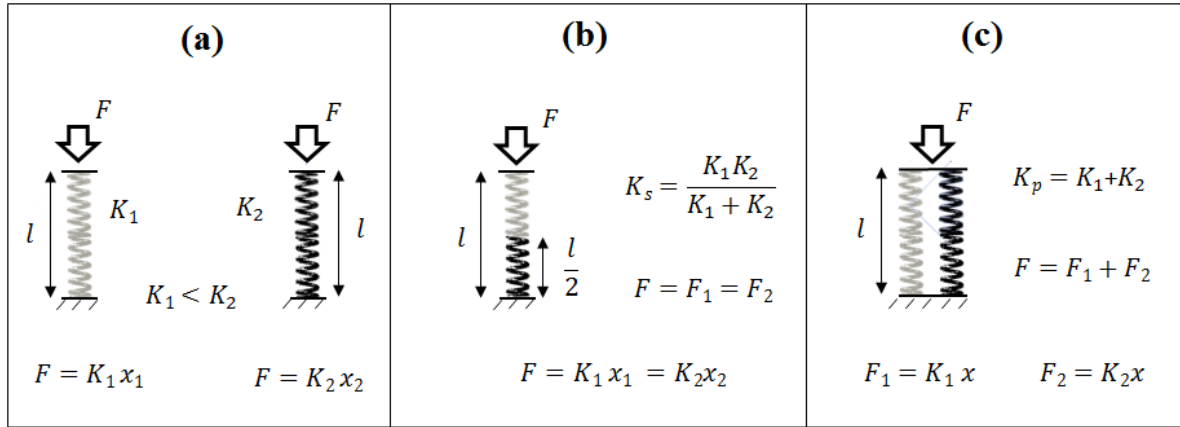


Figure 6.2 Schematic of the spring model (a) Individual; (b) Series; (c) Parallel

The energy absorbing characteristics of the foam pad depends on the stiffness (force deflection curve) and the collapse pattern [114, 115]. The stiffness of the foam pad in turn depend on the elastic modulus and contact area. It should be noted that the elastic modulus of the hard foam is approximately ten times higher than the elastic modulus of soft foam [108]. If this hard and soft foam is combined in series or parallel, the stiffness of the system will change. For instance, if the hard and soft foam are considered as spring of high (K_1) and low (K_2) stiffness respectively, then the when they are connected in series and parallel, the stiffness of the system will entirely change as shown in Fig 6.2. When either the individual, series or parallel system of springs of the same length are subjected to same force, then the deflection experienced by the spring will be different. Moreover, the intensity of energy absorbed by each spring will be different. Hence, it is evident that when two individual foam pads are used individually or in other combined (series or parallel) forms, the stiffness and the intensity of energy absorbed by the foam

pad will vary. It should be noted that the bilayer foam pad employed in the current army helmet is a series form of the hard and soft foam. Thus, it has different stiffness compared to individual and parallel form and thus for the given force it deflects differently compared to individual and parallel foam. Hence, for the given head helmet subspace and for a given loading condition, selection of the right form of the foam pad is essential.

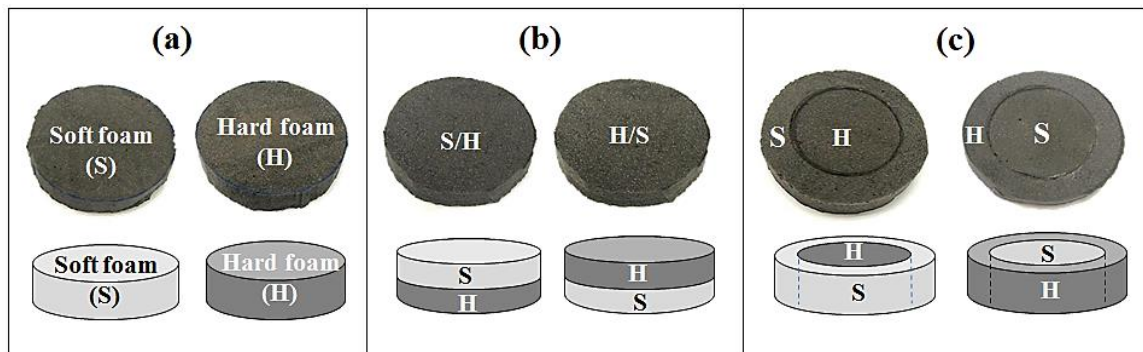


Figure 6.3 Foam pad configurations; top row – actual foam used in experiment: bottom row – schematic model of foam (a) Individual model (b) Series model (b) parallel model

With these considerations, six configurations of foam pad are designed as shown in Fig 6.3 for the analyzing the energy absorption characteristics. The configurations include two individual, two series and two parallel. The series and parallel configurations comprise about 50% hard and 50% soft foam. The total thickness (0.75”) and surface area (12.96”) of the foam pad system is same in all the configurations. When these foam pads are loaded as shown in Fig 6.4, each configuration will collapse differently. Hence, though the two series or parallel foam design have same stiffness, they are expected to collapse differently. Thus, each foam design will absorb different energy and the question is which foam design serves better at what conditions. This in turn is studied with the impact experiments. Each foam design is experimentally subjected to similar loading condition as shown in Fig 6.4. The loading setup and conditions are discussed in

the experimental section. The experimental results are then analyzed in terms of load experienced by the anvil (load transferred by the foam pads) and the acceleration of the impactor. The pad design that offers lesser force to anvil and less acceleration to the impactor absorbs the maximum energy for any given conditions. It should be noted that the acceleration of the impactor and the force experienced by the anvil are related by the Newton's second law of motion $F = ma$, where F is the force experienced by the anvil, a is the acceleration of the impactor and m is the mass of the impactor.

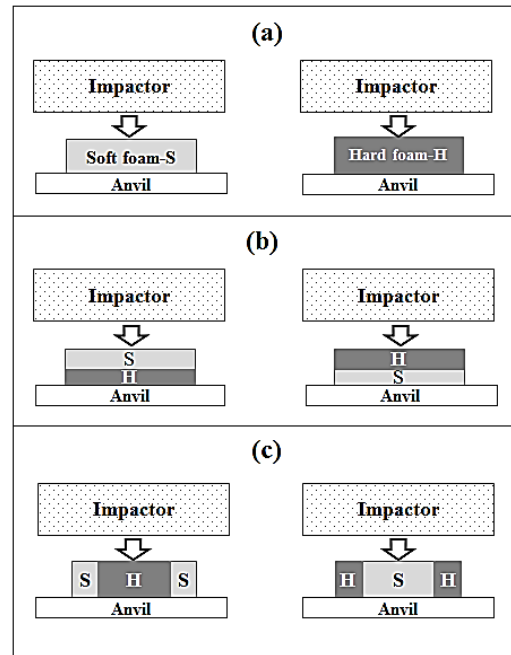


Figure 6.4 Schematic of the experimental loading setup; a) Individual foam model; b) Series foam model; c) Parallel foam model

6.2.2 Experimental model

The experimental model comprises of foam pads, impactor and steel anvil. Based on the initial analysis discussed in the theoretical model, six foam pad configurations are made as shown in Fig 6.3. The size of the foam pad is comparable to the crown pad of the

ACH; the diameter and thickness of the crown pad is 5" and 0.75", whereas the diameter and thickness of the foam pad considered for the study is 4" and 0.75". The series and parallel configurations are made of 50% soft and 50% hard foam. The soft and hard foam pads are glued together with a thin layer of rubber cement. The foam pads are supplied by the Team Wendy Inc., which supplies foam pad for the army ACH.

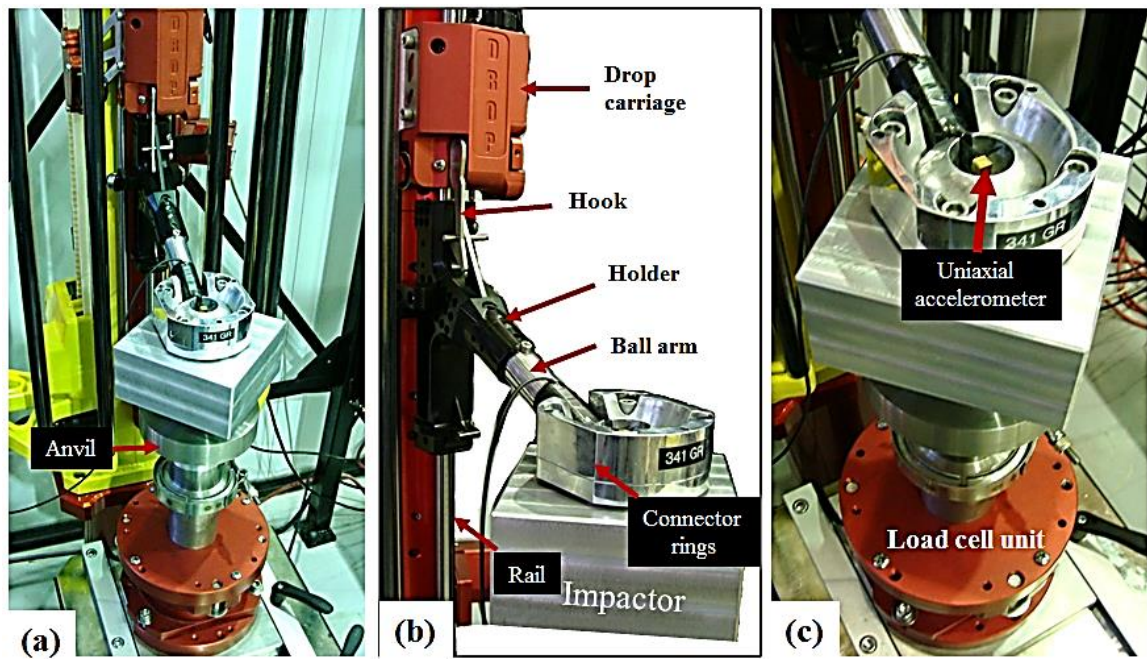


Figure 6.5 (a) Cadex monorail drop tower setup; (b) rigid aluminum surrogate setup; (c) Accelerometer mounted at the center of ball arm and load cell unit assembled to the bottom of anvil

The impactor setup and the anvil employed in this study are integrated in the uniaxial monorail drop tower as shown in fig 6.5 (a). Cadex Inc. manufactures the drop tower. The impactor setup consists of the holder, ball arm and connector rings as shown in Fig 6.5(b). The impactor used in the study is an aluminum block which is assembled to the ball arm using the connector rings. The ball arm in turn is connected to the holder which runs over the rail provided in the drop tower. The ball arm, connector rings and holder are made of aluminum material. The combined mass of the impactor setup and the

impactor is around 4.9 kg, which is approximately the weight of a human head. Since the details of the monorail tower are available in the [107] just basic working principles are discussed here. An electric operated drop carriage is hooked to the impactor setup as shown in Fig 6.5 (b). The drop carriage is raised automatically to a specific height and a switch for dropping the impactor setup releases the hook. On releasing the hook, the impactor drops on the anvil under the action of gravity. A 5” diameter steel anvil is assembled to the load cell unit as shown in Fig 6.5 (a). The impact area of the aluminum impactor is a square section of the length close to 6”. Hence, there is excess room to accommodate the deformation of the 4” diameter foam pads. The foam pads are placed at the center of the anvil.

The measurement system includes a linear acceleration of the impactor and the impact force transmitted by the foam pads. The linear acceleration of the impactor is measured by a piezoresistive accelerometer mounted at the center of the ball arm as shown in Fig 6.5 (c). The load cell unit assembled at the bottom of the anvil measures the impact force. Three impact velocities of low (1 m/s), medium (3 m/s) and high (5 m/s) are used as the impact loading conditions. Each experiment is repeated three times leading to 54 experiments in total. Due to hysteresis, each foam pad is loaded only once. Hence, a total of 54 foam samples is prepared for the assessment. The acceleration and load cell data are recorded every 30 μ s.

6.3 RESULTS

6.3.1 Low impact velocity

Acceleration and impact force data for the impact velocity of 1 m/s is shown in Fig 6.6. Each foam pad exhibits unique pattern. Among the foam pads, shortest duration

with the highest peak magnitude of acceleration is observed for hard foam; whereas longest duration with the lowest peak magnitude of acceleration is observed for soft foam. The parallel and series pads stand in between the hard and soft foam. The peak magnitude of acceleration for the parallel foam is lesser than hard foam and greater than the series foam. The duration in turn is higher than the hard foam and lesser than the series foam. There are slight differences in the magnitude of acceleration between the two designs of the parallel configuration. However, the pattern remains similar. The two designs for series configuration exhibit similar magnitude and pattern of the acceleration. The number of oscillations in the acceleration profile increase in the following order; hard, parallel, series and soft.

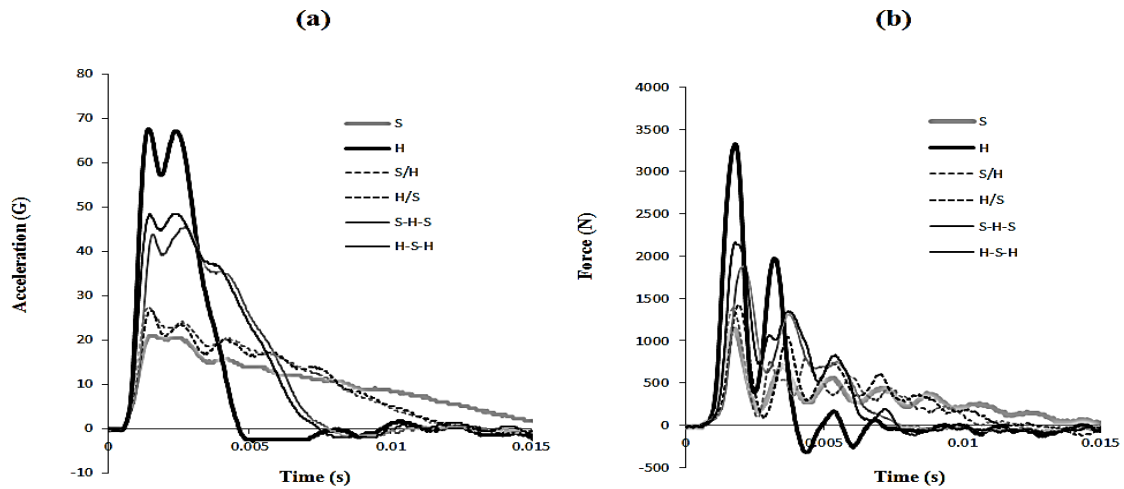


Figure 6.6 Experimental measurements at an impact velocity of 1 m/s for all the foam configurations; a) acceleration; (b) impact force

Between the foam pads, the variations in the peak magnitude and duration of impact force and the oscillations observed are similar to the variations observed for acceleration profiles. The frequency of oscillations is quite similar in all foam pad cases.

The peak values of the impact force and acceleration listed in Table 6.1 gives an overview of the variations between each foam configurations. HIC calculated from the acceleration profiles is also listed in the same table. Soft foam produces the least HIC and hard foam produces the highest HIC; the HIC for parallel is higher than the series.

Table 6.1 Peak values of the study parameters

Parameter	Impact velocity (m/s)	Individual		Series		Parallel	
		S	H	S/H	H/S	S-H-S	H-S-H
Acceleration	1	21 ± 0	68 ± 1	28 ± 0	27 ± 2	46 ± 2	48 ± 2
	3	79 ± 2	75 ± 3	73 ± 1	70 ± 3	56 ± 1	68 ± 1
	5	446 ± 6	157 ± 1	215 ± 3	218 ± 2	248 ± 9	224 ± 5
HIC	1	7 ± 1	59 ± 1	11 ± 1	10 ± 1	33 ± 5	39 ± 2
	3	124 ± 2	140 ± 4	152 ± 4	143 ± 6	108 ± 2	140 ± 2
	5	2425 ± 2	667 ± 2	878 ± 12	899 ± 12	1030 ± 20	907 ± 15
Impact force	1	1143 ± 40	3324 ± 500	1390 ± 30	1429 ± 200	1884 ± 90	2167 ± 200
	3	2422 ± 90	3615 ± 450	2877 ± 320	2705 ± 40	2310 ± 140	2374 ± 50
	5	14519 ± 150	5337 ± 160	6387 ± 40	6288 ± 10	7402 ± 500	6421 ± 175

6.3.2 Medium impact velocity

Figure 6.7 shows the acceleration and impact force for different foam configurations at the impact velocity of 3 m/s. Obviously, the magnitude of acceleration of the impactor at 3 m/s impact velocity is greater than 1 m/s impact velocity. The peak magnitude of acceleration is highest for the soft foam which is completely different compared to 1 m/s impact velocity case; the variation of the initial peak magnitude of acceleration for all the foam pad is however similar to the 1 m/s impact velocity case. For soft, series and parallel foam pads, an initial rise in acceleration followed by a drop then a secondary rise is observed. For hard foam, the secondary is absent in the

acceleration profile. The duration of acceleration increases in the following order; hard, series, parallel and soft.

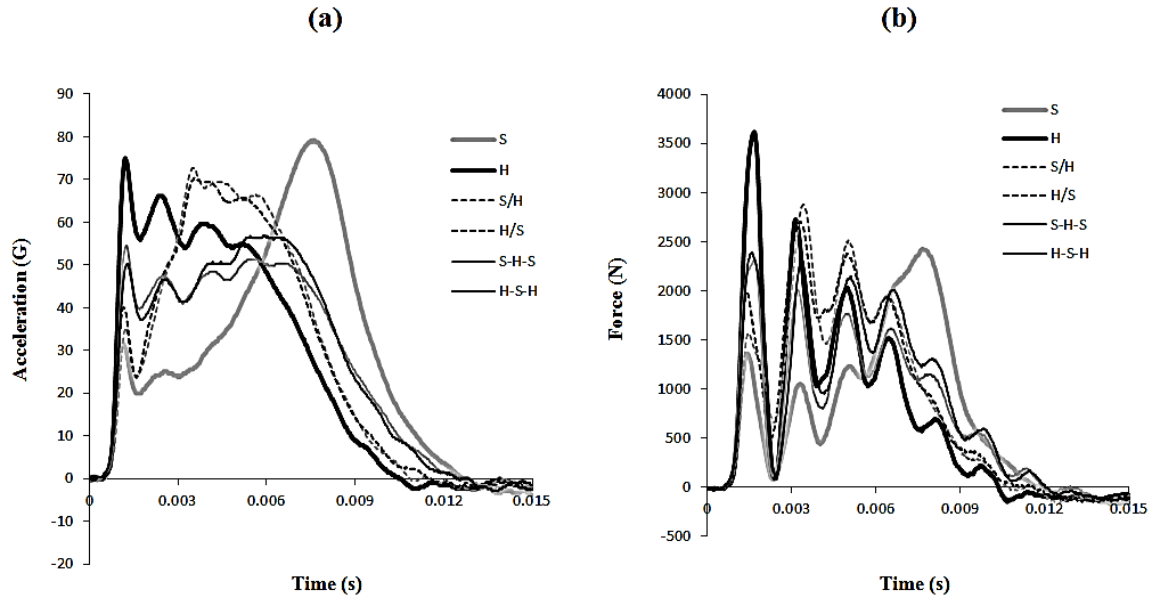


Figure 6.7 Experimental measurements at an impact velocity of 3 m/s for all the foam configurations; a) acceleration; (b) impact force

The variations of magnitude of initial rise followed by a secondary rise in the impact force are similar to the acceleration profiles for the foam pads. Similarly the variation in the duration of impact force of the foam pads is similar to its acceleration profiles. The parallel foam produces the least HIC, impact force and acceleration which are listed in Table 6.1. Series foam produces the highest HIC and acceleration; impact force is highest for hard foam

6.3.3 High impact velocity

Acceleration and impact force data for the impact velocity of 5 m/s is shown in Fig 6.8. At this velocity all the foam pads exhibits a similar pattern of the acceleration; initial rise followed by a drop then secondary rise. The magnitude of secondary rise is

higher than the initial rise in all the cases. The duration of acceleration is quite similar in all cases except the soft foam where least duration is observed. The peak magnitude of acceleration is observed for soft foam while least is observed for hard foam.

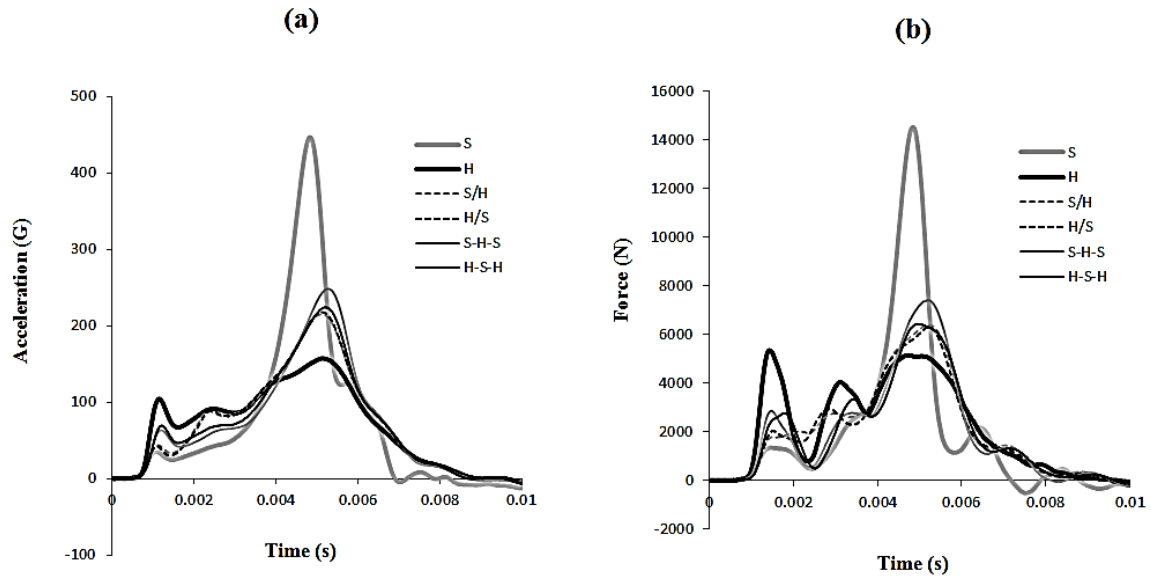


Figure 6.8 Experimental measurements at an impact velocity of 5 m/s for all the foam configurations; a) acceleration; (b) impact force

The magnitude and duration of impact force of the foam pads vary similar to the acceleration profile. HIC, impact force and acceleration is least for the hard foam and it is the most for soft foam. There is a significant difference between the two designs of the parallel foam configurations. The HIC, impact force and acceleration of H-S-H is less than the S-H-S design. However there is no much difference for two designs in the series foam configurations.

6.4 DISCUSSION

Before discussing the results, the characteristics of the each foam pad mentioned in the theoretical model are reviewed. The two key parameters that determine the energy

absorbing characteristics of the foam pad are the stiffness and the collapse pattern. The stiffness of the foam pad depend on the elastic modulus, contact area of the foam and the type of design (parallel or series). The elastic modulus of the hard foam is approximately ten times higher than the soft foam. The contact area of the foam pad is same in all the configurations. These considerations lead to following conclusions. Among the six configurations, the individual hard and soft foam has the highest and lowest stiffness respectively. The parallel design has a higher stiffness compared to the series. The collapse pattern of the each foam pad is different. Though the pattern of collapse of the foam is not studied in the work, the results are viewed with this perspective. With these understandings the results are discussed separately for each foam pad.

6.4.1 Hard and soft foam

The soft foam having the least stiffness deforms instantaneously upon the loading. Hence at the lowest impact velocity of 1 m/s, the soft foam deforms thereby increasing the contact duration as shown in Fig 6.6 (a). As a result it absorbs more energy and transfers lesser load to the anvil as shown in Fig 6.6 (b). The hard foam in turn having the highest stiffness deforms very less resulting in less contact duration. Hence it absorbs very little force and transfers the rest to the anvil as shown in the same figures. At 3 m/s impact velocity, the load imparted to the foam increases. For this load, the soft foam attains its maximum deformation limit resulting in bottoming out. Thus, the unabsorbed energy and load are transferred to the anvil. The instantaneous rise in the acceleration of the impactor as shown in Fig 6.7 (a) and the force in Fig 6.7 (b) depicts the phenomenon of bottoming out. The hard form however is stiff for this load; the deformation of pad is less and absorbs less energy and load. The remaining load is transferred to the anvil and

thus to the impactor. Hence, it is evident that though the soft foam bottoms out at 3 m/s impact velocity, the soft foam is still better than the hard foam.

At the impact velocity of 5 m/s, the hard foam absorbs more energy. The soft foam which reaches the point of bottoming out at 3 m/s impact velocity, when used at 5 m/s impact velocity it becomes more vulnerable. It absorbs very less energy and transfers most of the load to the anvil. This is clear from the Fig 6.8. The HIC, acceleration and impact force for both the foam pads at all the three velocities are listed in Table 6.1. It is evident that at the high impact velocity of 5 m/s hard forms performance better than soft foam. It is thus understood that, for the pad thickness of 0.75" or for the head helmet subspace of 0.75" using a soft foam for the impact velocities of 1 and 3 m/s is better than using a hard foam. It should be noted that at 3 m/s the soft foam bottoms out. Hence it is not advisable to use the soft foam at 3 m/s impact velocity even if is better than hard foam. At and above 5 m/s impact velocity, hard foam serves better.

6.4.2 Series and parallel foam

In parallel foam design, both the hard and soft foam deforms equally and thus they bear different loads upon loading. Hence, the point of bottoming out of soft and hard foam depends on each other. In case of series foam design, each foam bears equal load but the extent of deformation of each foam is different. The point of bottoming out is independent of each other. The parallel foam has a higher stiffness compared to series foam. At 1 m/s impact velocity it is apparent that series foam will deform more compared to parallel because of the stiffness effect. Hence, the load transferred by the series foam is lesser than the parallel foam. There is no much variation between the two designs of the series foam since the deformation of each foam is independent of each other. However a

little difference is observed between the two designs in the parallel foam. This is due to the collapse pattern; the hard foam surrounding the soft foam (H-S-H) has a controlled deformation pattern since the stiffness of the boundary is stiffer. In case of soft foam surrounding the hard foam (S-H-S) the stiffness of the boundary is not stiff leading to uncontrolled deformation.

At 3 m/s impact velocity, the soft foam in the series design bottom outs and the hard foam doesn't. Hence the performance lies in between the individual hard and soft foam. The parallel foam, which is less stiff than individual hard foam and stiffer than individual soft, and series foam transfers the least load to the anvil and impactor. However, at the impact velocity of 5 m/s, the parallel design transfers more load compared to series foam. The contact area is the reason behind this. In the parallel design only 50% of the surface area of the hard foam are involved whereas in series 100% surface area of hard foam is involved. Increase in contact area increases the stiffness and hence the role of the contact area of hard foam dominates at 5 m/s impact velocity. Hence, at higher velocities, the series design is better than the parallel design.

Thus, the key parameters that affect the energy absorbing characteristics of foam pad are elastic modulus, contact surface area and collapse pattern. At the lower impact velocity of 1 m/s, less stiff pad like soft foam and series foam deforms more resulting in higher energy absorption of more energy; whereas high stiff pads deform a little resulting in the transfer of more loads. At the medium impact velocity of 3 m/s less stiff foam (soft and series) bottoms out and the high stiff hard form deforms less resulting in the transfer of more load to anvil and impactor; whereas the parallel pad absorbs maximum force. At the high impact velocity of 5 m/s, the hard foam absorbs maximum energy compared to

other foam. Hence, it is evident that for the efficient absorption of energy, the stiffness of the pad needs to be increased with the increase in the impact velocity.

6.5 CONCLUSIONS

Six configurations designed with hard and soft foam are subjected to similar blunt loading conditions and are analyzed for the energy absorbing characteristics. The analysis leads to the following conclusions.

- At the low impact velocity (1 m/s) soft foam performs better and at the high impact velocity (5 m/s) hard foam performs better; parallel foam pad performs better at medium velocity (3 m/s).
- For a given foam pad thickness, by increasing the stiffness of the pad with increase in the impact velocity, the energy absorption of the pad can be maximized; there is a linear relationship between the impact velocity and stiffness of the pad for the efficient absorption of energy.
- Stiffness of the pad depend on the elastic modulus and contact area. An increase in the contact area increases the stiffness of the pad and thus plays a critical role in the energy absorption.
- Point of bottoming out and the force and deflection corresponding to the point is the key to identify the limits of the use of foam pads.

CHAPTER 7: CONCLUDING REMARKS

Explosions cause blast and blunt induced traumatic brain injuries. Understanding the fundamental loading mechanics of the head during a blast is necessary to resolve TBI. With simple mechanical head surrogates, experiments are carried out to study the loading mechanics of the blast and blunt loadings. Computational modelings have been extensively used to complement the experimental findings.

7.1 SUMMARY AND CONCLUSIONS

Both experimental and computational techniques are used to understand the blast and blunt loading mechanics. For blast loading, a 9” shock tube is used for generating the blast load. A polycarbonate cylindrical shell - mineral oil complex is used as head surrogate. For numerical simulations, CEL technique is used for modeling the blast-structure interaction. The findings from the blast studies are

- The total load at a point in the fluid can be partitioned into direct and indirect loads. Direct load is the stress wave transmitted from the blast to the cylinder and then to the fluid and is governed by the acoustic impedance mismatch. Higher the mismatch, lower is the transmission. Indirect load is the loading arising from the deflection of the container that loads the fluid, and this is governed by material stiffness and thickness of the shell. Higher the stiffness or/and the thickness, lesser is the indirect load.
- In the ranges of air blast (field-relevant) load, peak pressure at any given point in the fluid is governed by direct transmissive load. Deflection-induced indirect loads govern the duration of impulsive pressure load.

- Based on the time difference in the stress wave propagation of the shell and the fluid, in some special cases, negative pressures can occur in the contrecoup region; this is indirect load and can possibly lead to cavitation in the fluid.
- ICP reduces linearly with increase in skull thickness and increases linearly with increase in reflected blast overpressure.

For understanding the blunt mechanics, acrylic sphere - ballistic gel complex for compliant surrogate and aluminum body for rigid surrogate are selected. Both experimental and numerical analysis is carried out to understand the mechanics. The findings from the blunt studies are

- Upon impacting a rigid target surface, the acrylic shell bends inward resulting in tensile loading and possibly fractures.
- While the acceleration field in the rigid head form is uniform, the field varies from coup to counter-coup region in the gel-filled compliant case.
- The variation in the acceleration field (coup to counter coup end) in compliant surrogate is influenced by the shell deformation that in turn depends on the stiffness of the target surface; coup acceleration exceeds the acceleration at the center of gravity of gel for stiffer target surface models.
- Acceleration and HIC in compliant surrogate is higher than the rigid surrogate in cases of less stiff target surfaces.
- Based on the observations, it can be concluded that compliant headform captures the mechanics of head-brain impact better than the rigid headform.

- Energy absorption in foam pads is governed by the shape and magnitude of force deflection curve (e.g stiffness, bottoming out thickness, energy).
- Different types of foams are required for a given thickness and drop height. A single pad system is not optimal at different drop heights.

7.2 RECOMMENDED FUTURE STUDIES

The studies conducted were formulated for understanding the fundamental mechanics of blast and blunt loading. The basic blast and blunt loading pathways established from these simple surrogates have to be extended to animal and cadaver models. Some of the future studies needed are

- In these studies, the thickness of the skull was assumed uniform. Nevertheless, in reality the thickness of the human skull varies throughout the head. Hence, the variation of the loading pathway and significance of each parameter in the mechanics has to be studied with the appropriate skull thickness model.
- Since the brain simulant is the key for establishing the correct loading mechanics, a range of the widely used brain simulant has to be employed to check for the differences in the findings.
- Effect of spherical and pointed target surface on the acceleration of the surrogate has to be studied for a better understanding of the blunt impact mechanics.
- Both blast and blunt studies should be extended to animal and cadaver models to deduce the actual neurodegenerative effects for the particular mechanics of loading.

- Effects of variation of thickness, shape and cross sectional area of the helmet padding have to be studied to establish the comprehensive conclusions on the energy absorption of the helmet pads.
- The results obtained from the foam pads have to be employed in actual helmets to optimize the net energy absorbing characteristics of the helmet.

REFERENCES

- [1] Ralph G. Depalma, M. D., David G. Burris, M. D., Howard R. Champion, F. R. C. S., and And Michael J. Hodgson, M. D., M.P.H., 2005, "Blast Injuries," *N Engl J Med*, 352(pp. 1335-1342.
- [2] Candole, C. a. D., 1967, "Blast Injury," *Can Med Assoc J*, 96(4), pp. 207–214.
- [3] Long, J. B., Bentley, T. L., Wessner, K. A., Cerone, C., Sweeney, S., and Bauman, R. A., 2009, "Blast Overpressure in Rats: Recreating a Battlefield Injury in the Laboratory," *J Neurotrauma*, 26(6), pp. 827-40.
- [4] Tanielian, T., and Jaycox, 2008, "Invisible Wounds of War," Technical Report.
- [5] Nampiaparampil, D. E., 2008, "Prevalence of Chronic Pain after Traumatic Brain Injury: A Systematic Review," *JAMA*, 300(6), pp. 711-9.
- [6] Gregory A. Elder, M. a. a. C., Md, 2009, "Blast-Related Mild Traumatic Brain Injury: Mechanisms of Injury and Impact on Clinical Care," *Mount Sinai Journal Of Medicine*, 76(pp. 111-118.
- [7] Courtney, A. C., and Courtney, M. W., 2009, "A Thoracic Mechanism of Mild Traumatic Brain Injury Due to Blast Pressure Waves," *Medical Hypotheses*, 72(1), pp. 76-83.
- [8] Moss, W., King, M., and Blackman, E., 2008, "Skull Flexure from Blast Waves: Mechanism for Brain Injury with Implications for Helmet Design," 103(108702).
- [9] Chavko, M., Koller, W. A., Prusaczyk, W. K., and Mccarron, R. M., 2007, "Measurement of Blast Wave by a Miniature Fiber Optic Pressure Transducer in the Rat Brain," *J Neurosci Methods*, 159(2), pp. 277-81.
- [10] Cernak, I., Wang, Z., Jiang, J., Bian, X., and Savic, J., 2001, "Ultrastructural and Functional Characteristics of Blast Injury-Induced Neurotrauma," *J Trauma*, 50(4), pp. 695-706.
- [11] Byard, R. W., Gabrielian, L., Helps, S. C., Thornton, E., and Vink, R., 2012, "Further Investigations into the Speed of Cerebral Swelling Following Blunt Cranial Trauma," *J Forensic Sci*, 57(4), pp. 973-5.
- [12] Zhang, L., Yang, K. H., King, A. I., and Viano, D., 2003, "A New Biomechanical Predictor for Mild Traumatic Brain Injury—a Preliminary Finding," eds.

- [13] Nishimoto, T., and Murakami, S., 1998, "Relation between Diffuse Axonal Injury and Internal Head Structures on Blunt Impact," *J Biomech Eng*, 120(1), pp. 140-7.
- [14] Mclean, A., and Anderson, R. W. G., 1997, "2 Biomechanics of Closed Head Injury,".
- [15] Skotak, M., Wang, F., Alai, A., Holmberg, A., Harris, S., Switzer Iii, R. C., and Chandra, N., 2013, "Rat Injury Model under Controlled Field-Relevant Primary Blast Conditions: Acute Response to a Wide Range of Peak Overpressures," *J Neurotrauma*.
- [16] Sundaramurthy, A., Alai, A., Ganpule, S., Holmberg, A., Plougonven, E., and Chandra, N., 2012, "Blast-Induced Biomechanical Loading of the Rat: An Experimental and Anatomically Accurate Computational Blast Injury Model," *J Neurotrauma*, 29(13), pp. 2352-64.
- [17] Chavko, M., Watanabe, T., Adeeb, S., Lankasky, J., Ahlers, S. T., and Mccarron, R. M., 2011, "Relationship between Orientation to a Blast and Pressure Wave Propagation inside the Rat Brain," *J Neurosci Methods*, 195(1), pp. 61-6.
- [18] Bass, C. R., Rafaels, K. A., and Salzar, R. S., 2008, "Pulmonary Injury Risk Assessment for Short-Duration Blasts," *J Trauma*, 65(3), pp. 604-15.
- [19] Thorn, D. R., Hurt Jr, H. H., and Smith, T. A., 1998, "Motorcycle Helmet Test Headform and Test Apparatus Comparison," eds.
- [20] Siniora, J., Taylor, R., and Suey, D., 2012, "Blunt Impact Performance Evaluation of Helmet Lining Systems for Military and Recreational Use,".
- [21] B. Joseph Mcentire, and Whitley, P., 2005, "Blunt Impact Performance Characteristics of the Advance Combat Helmet and the Paratrooper and Infantry Personnel Armor System for Ground Troops Helmet," Technical Report No. USAARL,
- [22] Cullen, D. K., Browne, K. D., Xu, Y., Adeeb, S., Wolf, J. A., Mccarron, R. M., Yang, S., Chavko, M., and Smith, D. H., 2011, "Blast-Induced Color Change in Photonic Crystals Corresponds with Brain Pathology," *J Neurotrauma*, 28(11), pp. 2307-18.
- [23] Bolander, R., Mathie, B., Bir, C., Ritzel, D., and Vandevord, P., 2011, "Skull Flexure as a Contributing Factor in the Mechanism of Injury in the Rat When Exposed to a Shock Wave," *Ann Biomed Eng*, 39(10), pp. 2550-9.
- [24] Skotak, M., Wang, F., and Chandra, N., 2012, "An in Vitro Injury Model for Sh-Sy5y Neuroblastoma Cells: Effect of Strain and Strain Rate," *Journal of Neuroscience Methods*, 205(1), pp. 159-168.

- [25] Arun, P., Spadaro, J., John, J., Gharavi, R. B., Bentley, T. B., and Nambiar, M. P., 2011, "Studies on Blast Traumatic Brain Injury Using in-Vitro Model with Shock Tube," *Neuroreport*, 22(8), pp. 379-84.
- [26] Ellis, E. F., Mckinney, J. S., Willoughby, K. A., Liang, S., and Povlishock, J. T., 1995, "A New Model for Rapid Stretch-Induced Injury of Cells in Culture: Characterization of the Model Using Astrocytes," *J Neurotrauma*, 12(3), pp. 325-39.
- [27] Slemmer, J. E., Zhu, C., Landshamer, S., Trabold, R., Grohm, J., Ardeshiri, A., Wagner, E., Sweeney, M. I., Blomgren, K., Culmsee, C., Weber, J. T., and Plesnila, N., 2008, "Causal Role of Apoptosis-Inducing Factor for Neuronal Cell Death Following Traumatic Brain Injury," *Am J Pathol*, 173(6), pp. 1795-805.
- [28] Engel, D. C., Slemmer, J. E., Vlug, A. S., Maas, A. I., and Weber, J. T., 2005, "Combined Effects of Mechanical and Ischemic Injury to Cortical Cells: Secondary Ischemia Increases Damage and Decreases Effects of Neuroprotective Agents," *Neuropharmacology*, 49(7), pp. 985-95.
- [29] Bain, A. C., and Meaney, D. F., 2000, "Tissue-Level Thresholds for Axonal Damage in an Experimental Model of Central Nervous System White Matter Injury," *J Biomech Eng*, 122(6), pp. 615-22.
- [30] Kodama, T., Hamblin, M. R., and Doukas, A. G., 2000, "Cytoplasmic Molecular Delivery with Shock Waves: Importance of Impulse," *Biophys J*, 79(4), pp. 1821-32.
- [31] Richmond Dr, Damon Eg, Fletcher Er, Bowen Ig, and Cs., W., 1968, "The Relationship between Selected Blast-Wave Parameters and the Response of Mammals Exposed to Air Blast.," *Ann N Y Acad Sci.*, 152(1), pp. 103-121.
- [32] Richmond, D. R., and White, C. S., 1962, "A Tentative Estimation of Man's Tolerance to Overpressures from Air Blast. Technical Progress Report," Technical Report No. DASA-1335.
- [33] Kamnaksh, A., Kovesdi, E., Kwon, S. K., Wingo, D., Ahmed, F., Grunberg, N. E., Long, J., and Agoston, D. V., 2011, "Factors Affecting Blast Traumatic Brain Injury," *J Neurotrauma*, 28(10), pp. 2145-53.
- [34] Elsayed, N. M., and Gorbunov, N. V., 2007, "Pulmonary Biochemical and Histological Alterations after Repeated Low-Level Blast Overpressure Exposures," *Toxicol Sci*, 95(1), pp. 289-96.
- [35] Golovkin, V. I., and Glaznikov, L. A., 1991, "[the Neurological Manifestations of Blast Trauma to the Brain]," *Voen Med Zh*, 8), pp. 37-8.

- [36] Ono, K., Kikuchi, A., Nakamura, M., Kobayashi, H., and Nakamura, N., 1980, "Human Head Tolerance to Sagittal Impact. Reliable Estimation Deduced from Experimental Head Injury Using Subhuman Primates and Human Cadaver Skulls," Technical Report No.
- [37] Anderson, R. W., Brown, C. J., Blumbergs, P. C., Mclean, A. J., and Jones, N. R., 2003, "Impact Mechanics and Axonal Injury in a Sheep Model," *J Neurotrauma*, 20(10), pp. 961-74.
- [38] Li, K., Cao, Y. X., Yang, Y. Q., Yin, Z. Y., Zhao, H., and Wang, L. J., 2012, "Establishment of a Blunt Impact-Induced Brain Injury Model in Rabbits," *Chin J Traumatol*, 15(2), pp. 100-4.
- [39] Shridharani, J. K., Wood, G. W., Panzer, M. B., Capehart, B. P., Nyein, M. K., Radovitzky, R. A., and Bass, C. R., 2012, "Porcine Head Response to Blast," *Front Neurol*, 3(pp. 70.
- [40] Bir, C., 2011, "Measuring Blast-Related Intracranial Pressure within the Human Head," W81XWH-09-1-0498.
- [41] Gurdjian, E., Lissner, H., and Patrick, L., 1963, "Concussion: Mechanism and Pathology," eds., 7, pp. 470-482.
- [42] Lissner, H., Lebow, M., and Evans, F., 1960, "Experimental Studies on the Relation between Acceleration and Intracranial Pressure Changes in Man," *Surgery, gynecology & obstetrics*, 111(pp. 329.
- [43] Hardy, W. N., Mason, M. J., Foster, C. D., Shah, C. S., Kopacz, J. M., Yang, K. H., King, A. I., Bishop, J., Bey, M., Anderst, W., and Tashman, S., 2007, "A Study of the Response of the Human Cadaver Head to Impact," *Stapp Car Crash J*, 51(pp. 17-80.
- [44] Ganpule, S., Gu, L., Alai, A., and Chandra, N., 2011, "Role of Helmet in the Mechanics of Shock Wave Propagation under Blast Loading Conditions," *Comput Methods Biomech Biomed Engin*, pp. 1-12.
- [45] Ganpule, S., Alai, A., Plougouven, E., and Chandra, N., 2012, "Mechanics of Blast Loading on the Head Models in the Study of Traumatic Brain Injury Using Experimental and Computational Approaches," *Biomech Model Mechanobiol*.
- [46] Zhu, F., Wagner, C., Dal Cengio Leonardi, A., Jin, X., Vandevord, P., Chou, C., Yang, K. H., and King, A. I., 2012, "Using a Gel/Plastic Surrogate to Study the Biomechanical Response of the Head under Air Shock Loading: A Combined

Experimental and Numerical Investigation," *Biomech Model Mechanobiol*, 11(3-4), pp. 341-53.

[47] Mediavilla Varas, J., Philippens, M., Meijer, S. R., Van Den Berg, A. C., Sibma, P. C., Van Bree, J. L. M. J., and De Vries, D. V. W. M., 2011, "Physics of Ied Blast Shocktube Simulations for Mtb Research," *Frontiers in Neurology*, 2.

[48] Alley, M. D., Schimizz, B. R., and Son, S. F., 2011, "Experimental Modeling of Explosive Blast-Related Traumatic Brain Injuries," *NeuroImage*, 54 Suppl 1(pp. S45-54.

[49] Cernak, I., Savic, J., and Lazarov, A., 1997, "Relations among Plasma Prolactin, Testosterone, and Injury Severity in War Casualties," *World J Surg*, 21(3), pp. 240-5; discussion 246.

[50] Cramer, F., Paster, S., and Stephenson, C., 1949, "Cerebral Injuries Due to Explosion Waves-- 'Cerebral Blast Concussion' a Pathologic, Clinical and Electroencephalographic Study," *Arch Neurol Psychiatry*, 61(1), pp. 1-20.

[51] Cheng, J., Gu, J., Ma, Y., Yang, T., Kuang, Y., Li, B., and Kang, J., 2010, "Development of a Rat Model for Studying Blast-Induced Traumatic Brain Injury," *J Neurol Sci*, 294(1-2), pp. 23-8.

[52] Clemedson, C. J., and Pettersson, H., 1953, "Genesis of Respiratory and Circulatory Changes in Blast Injury," *Am J Physiol*, 174(2), pp. 316-20.

[53] Dal Cengio Leonardi, A., Bir, C. A., Ritzel, D. V., and Vandevord, P. J., 2011, "Intracranial Pressure Increases During Exposure to a Shock Wave," *Journal of Neurotrauma*, 28(1), pp. 85-94.

[54] Teasdale, G., and Jennett, B., 1974, "Assessment of Coma and Impaired Consciousness : A Practical Scale," *The Lancet*, 304(7872), pp. 81-84.

[55] Suneson, A., Hansson, H. A., and Seeman, T., 1990, "Pressure Wave Injuries to the Nervous System Caused by High-Energy Missile Extremity Impact: Part II. Distant Effects on the Central Nervous System--a Light and Electron Microscopic Study on Pigs," *J Trauma*, 30(3), pp. 295-306.

[56] Cullis, I. G., 2001, "Blast Waves and How They Interact with Structures," *J R Army Med Corps*, 147(1), pp. 16-26.

[57] Zhang, L., Yang, K. H., and King, A. I., 2004, "A Proposed Injury Threshold for Mild Traumatic Brain Injury," *J Biomech Eng*, 126(2), pp. 226-36.

- [58] Chen, X., and Chandra, N., 2004, "The Effect of Heterogeneity on Plane Wave Propagation through Layered Composites," *Composites Science and Technology*, 64(10–11), pp. 1477-1493.
- [59] Chen, X., Chandra, N., and Rajendran, A. M., 2004, "Analytical Solution to the Plate Impact Problem of Layered Heterogeneous Material Systems," *International Journal of Solids and Structures*, 41(16–17), pp. 4635-4659.
- [60] Rahman, M. A., and Rahman, A. S., 2005, "Design Parameters of a Circular Proving Ring of Uniform Strength," eds., Dhaka, pp. 1-5.
- [61] Kleinschmit, N. N., 2011, "A Shock Tube Technique for Blast Wave Simulation and Studies of Flow Structure Interactions in Shock Tube Blast Experiments,".
- [62] Chandra, N., Ganpule, S., Kleinschmit, N., Feng, R., Holmberg, A., Sundaramurthy, A., Selvan, V., and Alai, A., 2012, "Evolution of Blast Wave Profiles in Simulated Air Blasts: Experiment and Computational Modeling," *Shock Waves*, 22(5), pp. 403-415.
- [63] Chandra, N., Holmberg, A., and Feng, R., 2011, "Controlling the Shape of the Shock Wave Profile in a Blast Facility," US Provisional patent application, 61542354.
- [64] Mowatt, S., and Skews, B., 2011, "Three Dimensional Shock Wave/Boundary Layer Interactions," *Shock Waves*, 21(5), pp. 467-482.
- [65] Chafi, M. S., Karami, G., and Ziejewski, M., 2009, "Numerical Analysis of Blast-Induced Wave Propagation Using Fsi and Alemulti-Material Formulations," *International Journal of Impact Engineering*, 36(10–11), pp. 1269-1275.
- [66] Honma, H., Ishihara, M., Yoshimura, T., Maeno, K., and Morioka, T., 2003, "Interferometric Ct Measurement of Three-Dimensional Flow Phenomena on Shock Waves and Vortices Discharged from Open Ends," *Shock Waves*, 13(3), pp. 179-190.
- [67] Fry, F. J., and Barger, J. E., 1978, "Acoustical Properties of the Human Skull," *J Acoust Soc Am*, 63(5), pp. 1576-90.
- [68] Ludwig, G. D., 1950, "The Velocity of Sound through Tissues and the Acoustic Impedance of Tissues," *The Journal of the Acoustical Society of America*, 22(6), pp. 862-866.
- [69] Chris Mougeotte, Pasquale Carlucci, Stephen Recchia, A., and Ji, H., 2010, Novel Approach to Conducting Blast Load Analyses Using Abaqus/Explicit-CEL.

- [70] Ofengeim, D. K., and Drikakis, D., 1997, "Simulation of Blast Wave Propagation over a Cylinder," *Shock Waves*.
- [71] Anderson, J. D., 2001, *Fundamentals of Aerodynamics*, McGraw-Hill,
- [72] Goggio, A. F., 1941, "The Mechanism of Contre-Coup Injury," *J Neurol Psychiatry*, 4(1), pp. 11-22.
- [73] King, A. I., 2001, "Fundamentals of Impact Biomechanics: Part 2--Biomechanics of the Abdomen, Pelvis, and Lower Extremities," *Annu Rev Biomed Eng*, 3(pp. 27-55.
- [74] Narayan Yoganandan, P. D., Frank A. Pintar, P. D., and Sanford J. Larson, M. D., Ph.D., 1998, *Frontiers in Head and Neck Trauma: Clinical and Biomechanical*, Medical College of Wisconsin, Milwaukee.
- [75] Goeller, J., Wardlaw, A., Treichler, D., O'bruba, J., and Weiss, G., 2012, "Investigation of Cavitation as a Possible Traumatic Brain Injury (Tbi) Damage Mechanism from Blast," *J Neurotrauma*.
- [76] Tamer El Sayed , A. M., Fernando Fraternali , Michael Ortiz, 2008, "Biomechanics of Traumatic Brain Injury," *Comput. Methods Appl. Mech. Engrg*, 197(pp. 4692-4701.
- [77] Taylor, P. A., and Ford, C. C., 2009, "Simulation of Blast-Induced Early-Time Intracranial Wave Physics Leading to Traumatic Brain Injury," *J Biomech Eng*, 131(6), pp. 061007.
- [78] Bir, C., 2011, "Measuring Blast-Related Intracranial Pressure within the Human Head," Technical Report No. DTIC Document,
- [79] Zhang, L. P. D., 2009, *Computational Modeling of Causal Mechanisms of Blast Wave Induced Traumatic Brain Injury – A Potential Tool for Injury Prevention*. Detroit.
- [80] Cernak, I., Merkle, A. C., Koliatsos, V. E., Bilik, J. M., Luong, Q. T., Mahota, T. M., Xu, L., Slack, N., Windle, D., and Ahmed, F. A., 2011, "The Pathobiology of Blast Injuries and Blast-Induced Neurotrauma as Identified Using a New Experimental Model of Injury in Mice," *Neurobiol Dis*, 41(2), pp. 538-51.
- [81] Rafaels, K. A., Bass, C. R., Panzer, M. B., and Salzar, R. S., 2010, "Pulmonary Injury Risk Assessment for Long-Duration Blasts: A Meta-Analysis," *J Trauma*, 69(2), pp. 368-74.

- [82] Varas, J. M., Philippens, M., Meijer, S., Van Den Berg, A., Sibma, P., Van Bree, J., and De Vries, D., 2011, "Physics of Ied Blast Shock Tube Simulations for Mtbi Research," *Frontiers in Neurology*, 2.
- [83] Bauman, R. A., Ling, G., Tong, L., Januszkiewicz, A., Agoston, D., Delanerolle, N., Kim, Y., Ritzel, D., Bell, R., Ecklund, J., Armonda, R., Bandak, F., and Parks, S., 2009, "An Introductory Characterization of a Combat-Casualty-Care Relevant Swine Model of Closed Head Injury Resulting from Exposure to Explosive Blast," *J Neurotrauma*, 26(6), pp. 841-60.
- [84] Richmond, D. R., Yelverton, J. T., and Fletcher, E. R., 1986, *New Airblast criteria for man*. Anaheim, CA.
- [85] Lynnerup, N., Astrup, J. G., and Sejrsen, B., 2005, "Thickness of the Human Cranial Diploe in Relation to Age, Sex and General Body Build," *Head & Face Medicine*.
- [86] Mahinda, H. a. M., and Murty, O. P., 2009, "Variability in Thickness of Human Skull Bones & Sternum – an Autopsy Experience," *Journal of Forensic Medicine and Toxicology*, 26(2), pp. 26-31.
- [87] Ropper, A. H., 2005, "Concussion and Other Head Injuries," *Harrison Principles of Internal Medicine*, 16(2), pp. 2447.
- [88] Jayarao, M., Chin, L. S., and Cantu, R. C., 2010, "Boxing-Related Head Injuries," *Phys Sportsmed*, 38(3), pp. 18-26.
- [89] Kirkendall, D. T., Jordan, S. E., and Garrett, W. E., 2001, "Heading and Head Injuries in Soccer," *Sports Med*, 31(5), pp. 369-86.
- [90] Tysvaer, A. T., 1992, "Head and Neck Injuries in Soccer. Impact of Minor Trauma," *Sports Med*, 14(3), pp. 200-13.
- [91] Wilberger, J. E., 1993, "Minor Head Injuries in American Football. Prevention of Long Term Sequelae," *Sports Med*, 15(5), pp. 338-43.
- [92] Schneider Rc, R. E. C. H. O. O. B. G., 1961, "Serious and Fatal Football Injuries Involving the Head and Spinal Cord," *JAMA*, 177(6), pp. 362-367.
- [93] King, A. I., 2000, "Fundamentals of Impact Biomechanics: Part I--Biomechanics of the Head, Neck, and Thorax," *Annu Rev Biomed Eng*, 2(pp. 55-81.
- [94] Becker, E. B., 1998, "Helmet Development and Standards," *Frontiers in Head and Neck Trauma Clinical and Biomedical*, N. Yoganandan et al. Eds., IOS Press.

- [95] Saczalski, K. J., Wagar, I. J., and Richardson, E. Q., 1976, "A Critical Assessment of the Use of Non-Human Responding Surrogates for Safety System Evaluation," eds.
- [96] Funk, J. R., Rowson, S., Daniel, R. W., and Duma, S. M., 2012, "Validation of Concussion Risk Curves for Collegiate Football Players Derived from Hits Data," *Ann Biomed Eng*, 40(1), pp. 79-89.
- [97] Viano, D. C., Casson, I. R., and Pellman, E. J., 2007, "Concussion in Professional Football: Biomechanics of the Struck Player--Part 14," *Neurosurgery*, 61(2), pp. 313-27; discussion 327-8.
- [98] Guskiewicz, K. M., Mihalik, J. P., Shankar, V., Marshall, S. W., Crowell, D. H., Oliaro, S. M., Ciocca, M. F., and Hooker, D. N., 2007, "Measurement of Head Impacts in Collegiate Football Players: Relationship between Head Impact Biomechanics and Acute Clinical Outcome after Concussion," *Neurosurgery*, 61(6), pp. 1244-52;
- [99] Forbes, J. A., Awad, A. J., Zuckerman, S., Carr, K., and Cheng, J. S., 2012, "Association between Biomechanical Parameters and Concussion in Helmeted Collisions in American Football: A Review of the Literature," *Neurosurg Focus*, 33(6), pp. E10: 1-6.
- [100] Ward, C., Chan, M., and Nahum, A., 1980, "Intracranial Pressure—a Brain Injury Criterion," *SAE Technical Paper*, 801304.
- [101] Rowson, S., Brolinson, G., Goforth, M., Dietter, D., and Duma, S., 2009, "Linear and Angular Head Acceleration Measurements in Collegiate Football," *Journal of Biomechanical Engineering*, 131(pp. 061016.
- [102] Pellman, E. J., Viano, D. C., Tucker, A. M., Casson, I. R., and Waeckerle, J. F., 2003, "Concussion in Professional Football: Reconstruction of Game Impacts and Injuries," *Neurosurgery*, 53(4), pp. 799-812; discussion 812-4.
- [103] Ibrahim, N. G., and Margulies, S. S., 2010, "Biomechanics of the Toddler Head During Low-Height Falls: An Anthropomorphic Dummy Analysis," *J Neurosurg Pediatr*, 6(1), pp. 57-68.
- [104] Ounsted, M., Moar, V. A., and Scott, A., 1985, "Head Circumference Charts Updated," *Arch Dis Child*, 60(10), pp. 936-9.
- [105] Cronin, D. S., 2011, *Dynamic Behavior of Materials, Volume 1*, Springer New York, Ballistic Gelatin Characterization and Constitutive Modeling.

- [106] Salisbury, C. P., and Cronin, D. S., 2009, "Mechanical Properties of Ballistic Gelatin at High Deformation Rates," *Experimental Mechanics*, 49(6), pp. 829-840.
- [107] Cadex, [Http://Www.Cadexinc.Com](http://www.cadexinc.com),
- [108] Zhang, L., Makwana, R., and Sharma, S., 2011, "Comparison of the Head Response in Blast Insult with and without Combat Helmet," eds.
- [109] Stronge, W. J., 2004, *Impact Mechanics*, Cambridge university press,
- [110] Gurdjian, E. S., Webster, J. E., and Lissner, H. R., 1950, "The Mechanism of Skull Fracture," *Radiology*, 54(3), pp. 313-39.
- [111] Michael R. Galarneau, M. S., Susan I. Woodruff, P. D., Judy L. Dye, M.S., R.N., A.N.P., , and Charlene R. Mohrle, M. S., R.N., and Amber L. Wade, M.P.H., 2008, "Traumatic Brain Injury During Operation Iraqi Freedom: Findings from the United States Navy–Marine Corps Combat Trauma Registry," *Journal of Neurosurgery*, 108(5), pp. 950-957.
- [112] Moss, W. C., King, M. J., and Blackman, E. G., 2012, "Towards Reducing Impact-Induced Brain Injury: Lessons from a Computational Study of Army and Football Helmet Pads," *Computer Methods in Biomechanics and Biomedical Engineering*, ahead-of-print), pp. 1-12.
- [113] Mcentire, B. J., and Shanaha, D. F., 1997, "Mass Requirements for Helicopter Aircrew Helmet," eds., 597, pp. 20.1-20.6.
- [114] Salwani M. S., A. A., Sahari B. B and Nuraini A. A., 2011, "Crash of Automotive Side Member Subjected to Oblique Loading," *International Journal of the Physical Sciences*, 6(pp. 7125-7131.
- [115] Xiong Zhanga, Gengdong Chenga, Zhong Youb, and Zhanga, H., 2007, "Energy Absorption of Axially Compressed Thin-Walled Square Tubes with Patterns," *Thin-Walled Structures*, 45(9), pp. 737-746.